NUCLEAR ENERGY INSTITUTE

Alexander Marion
SENIOR DIRECTOR, ENGINEERING
NUCLEAR GENERATION DIVISION

June 13, 2006

Document Control Desk
U.S. Nuclear Regulatory Commission
Washington, DC 20555-0001

SUBJECT: Re-submittal of Safety Evaluation by the Office of Nuclear Reactor Regulation of Electric Power Research Institute (EPRI) Topical Report TR-1002865, "Topical Report on Reactivity Initiated Accidents: Bases for RIA Fuel Rod Failures and Core Coolability Criteria"

PROJECT: 669

Dear Mr. Berkow:

The enclosed letter was originally addressed to Mr. Herbert N. Berkow without knowledge of his retirement. We are resubmitting the letter to NRC, addressed to the Document Control Desk, per the instructions of Ms. Michelle Honcharik.

If you have any questions, please feel free to contact me at 202.739.8080; am@nei.org or Gordon Clefton at 202.739.8086; gac@nei.org.

Sincerely,

Alexander Marion

Enclosure

c: Michelle C. Honcarik, NRR/DPR/PSPB, US NRC

NUCLEAR ENERGY INSTITUTE

Alexander Marion
SENIOR DIRECTOR, ENGINEERING
NUCLEAR GENERATION DIVISION

April 27, 2006

Mr. Herbert N. Berkow
Director
Project Directorate IV
Division of Licensing Project Management
Office of Nuclear Reactor Regulation
U.S. Nuclear Regulatory Commission
Washington, DC 20555-0001

SUBJECT: Safety Evaluation by the Office of Nuclear Reactor Regulation of Electric Power Research Institute (EPRI) Topical Report TR-1002865, "Topical Report on Reactivity Initiated Accidents: Bases for RIA Fuel Rod Failures and Core Coolability Criteria"

Dear Mr. Berkow:

As stated in our previous correspondence, the industry has considered the staff's concerns documented in the above referenced safety evaluation (SE) as a set of requests for additional information (RAIs) and has prepared technical responses to these RAIs. Drafts of the responses to the RAIs were provided to the NRC Staff in September 2005 and a meeting was held with the NRC Staff on November 2, 2005, to further discuss the technical issues related to the RAIs. The purpose of this letter is to formally transmit the final responses to the NRC for review and consideration.

A total of eleven RAIs have been constructed from the technical concerns raised in the above referenced SE. Separate responses have been prepared to address each RAI. The attached responses provide additional information to help clarify the technical justification for the proposed RIA acceptance criteria and to further expand the technical basis provided in the topical report. The industry believes that the proposed fuel acceptance criteria are fully supported by the combination of the information provided in the topical report and these responses to the Staff's RAIs. While we believe that the methods used to develop the proposed criteria adequately address the uncertainties in the experimental data and reactor experience, we recognize that other methods can be used to consider the impact of data uncertainties on the acceptance criteria. In this regard, we are willing to discuss with the NRC Staff alternative methods to address data uncertainties in the development of RIA fuel acceptance criteria.

1776 I STREET, NW SUITE 400 WASHINGTON, DC 20006-3708 PHONE 202.739.8080 FAX 202.533.0164 am@nei.org

We will follow-up with the NRC Staff in a few weeks to schedule a meeting to discuss any questions or comments your Staff may have on these responses. We look forward to working with the Staff to ensure realistic conservatisms for our proposed criteria. If you have any questions, please feel free to contact me at 202.739.8080; am@nei.org or Gordon Clefton at 202.739.8086; gac@nei.org.

Sincerely,

Alexander Marion

Attachments

c: Odelli Ozer, EPRI

Response to Requests for Additional Information (RAI's)
NRR Safety Evaluation Report – Project No. 689

C-1. In addition, the FALCON code version used in the development of the coolability limit underestimates fuel temperatures at high burnups resulting in an overprediction of the energy needed to cause fuel melting when the fuel burnup is above 40 gigawatt days per metric ton uranium (GWD/MTU). This effect leads to a non-conservative melt enthalpy limit.

Response to RAI C-1

The basis for the statement on the underestimation of the fuel temperature at high burnup in FALCON was not provided; so several aspects and considerations for the coolability calculation are described below. The response comprises two parts: 1) validation of the best-estimate fuel temperature calculation in FALCON under RIA conditions against applicable data and 2) sensitivity of the fuel temperature calculation to the UO_2 thermal conductivity model.

The validation of fuel rod temperature calculations for rapid energy deposition events is difficult because no measured fuel temperature data are available for code comparison purposes. Indirect data (e.g. ceramography, metallography, and dimensional measurements) from inpile and post-test examinations have been used to validate FALCON BETA-RIA [C-1.1] for the analysis of RIA events. Based on the validation of FALCON BETA RIA with results from RIA-simulation experiments in CABRI and NSRR, it is our opinion that the code provides a best estimate of the fuel temperatures during rapid energy deposition transients such as RIA events.

One area of potential criticism of FALCON BETA-RIA is the UO_2 thermal conductivity model used in the program, specifically, the treatment of burnup degradation. The effect of UO_2 thermal conductivity on the fuel temperature calculation in FALCON BETA-RIA was evaluated using three different UO_2 thermal conductivity correlations. The results from the baseline model (MATPRO-11 [C-1.2] with the ESCORE Burnup Correction [C-1.3]) in FALCON BETA-RIA were compared to the results for two newer UO_2 thermal conductivity models: 1) the current FRAPTRAN thermal conductivity model [C-1.4], and 2) the NFIR model [C-1.5] developed using thermal diffusivity data from highly irradiated fuel pellets. The NFIR model has recently been incorporated into the latest version of FALCON [C-1.6]. A description of each of these UO_2 thermal conductivity correlations is contained in Appendix C-1.A.

Validation of FALCON BETA-RIA Fuel Temperature Calculations Using RIA Tests

It must be acknowledged from the onset that the baseline UO_2 thermal conductivity correlation used in FALCON BETA-RIA [C-1.1] is the MATPRO-11 [C-1.2] temperature and porosity dependent model, which is based entirely on unirradiated material. For use in FALCON BETA-RIA, the MATPRO-11 model was modified to include a burnup dependency throughout the entire temperature range of applicability (300 K to 3100 K) based on an correction factor developed in the mid-1980's for the ESCORE fuel performance code [C-1.3]. This correction factor saturates at a maximum reduction in the thermal conductivity of 14% at a pellet average burnup of 30 GWd/MTU. Since the time that this correction factor was developed, a large amount of thermocouple measurements and thermal diffusivity data from highly irradiated fuel has been made available that indicate a stronger effect of burnup on the thermal conductivity of UO_2 below temperatures of 1600°C where phonon transport is the primary mechanism for heat transfer processes. Newer UO_2 thermal conductivity correlations use burnup reduction factors of 30% to 40% at a pellet average burnup of 65 GWd/tU and for a temperature of ~1000°C. As discussed in Appendix C-1.A, the burnup reduction factor in the newer UO_2 thermal conductivity correlations is dependent on temperature, with the reduction factor decreasing at higher temperatures.

Comparison of the FALCON BETA-RIA steady state temperature calculations with thermocouple measurements shows that the baseline UO_2 thermal conductivity correlation results in a underestimation of the fuel centerline temperatures by ~200°C at pellet average burnup levels exceeding 30 GWd/MTU. A comparison to thermocouple measurements for the Halden irradiation test IFA-515.10 Rod A1 is shown in Figure C-1.1. Also shown for comparison is the FALCON calculated fuel temperatures using the FRAPTRAN [C-1.4] and NFIR [C-1.5, 6] UO_2 thermal conductivity correlations. The results for these two correlations agree well with the thermocouple data and are almost indistinguishable from each other.

For steady state conditions, heat transfer across the pellet is primarily a function of the pellet thermal conductivity. However, this is not the case for RIA conditions. The rapid nature of the energy deposition results in an almost adiabatic condition where the maximum fuel temperature depends mostly on the UO_2 specific heat capacity, the radial power distribution, and the deposited energy. Therefore, it is not possible to evaluate the capability of a code to calculate fuel temperatures during rapid RIA conditions using steady state thermocouple measurements.

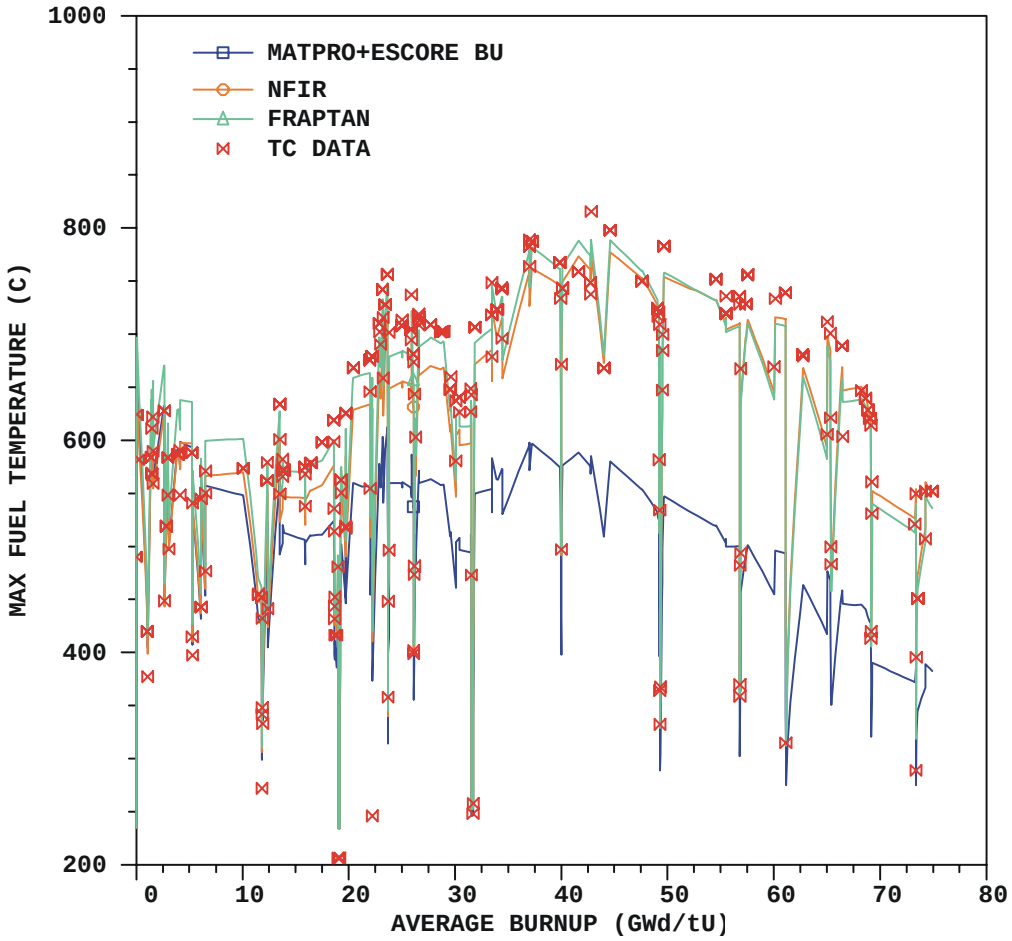

Figure C-1.1 Comparison of fuel centerline temperature predictions by FALCON BETA RIA, using MATPRO-11/ESCORE, FRAPTRAN and NFIR thermal conductivity models with thermocouple measurements for the Halden irradiation test IFA-515.10 Rod A1.

Unlike steady state irradiation of fuel rods, no thermocouple measurement data for fuel pellet temperatures are available from the RIA-simulation experiments. Basically, there are two indirect methods availabe to validate the calculation of fuel temperature for RIA conditions. The first method is to compare the in-pile measurements for cladding and fuel column elongation from high burnup fuel with the calculated results from the fuel behavior code. These parameters reflect the thermal expansion of the fuel column, which is directly related to fuel temperatures. The second method is to use ceramography results to visually identify the presence of pellet melting for high fuel enthalpy tests (H_{max} ~ 200 cal/gm). The ceramography results are obtained through destructive examinations following the experiments. Both methods were used to validate the fuel temperature calculation in FALCON.

Figure C-1.2 shows a comparison of the calculated and measured cladding elongation during RIA-simulation tests on high burnup fuel rods in CABRI and NSRR. Good agreement is found between predicted and measured results for a variety of fuel rod designs and burnup levels. Because of the small residual pellet-cladding gap, these results reflect the expansion of the fuel column during the energy deposition. Since this expansion is proportional to the pellet

temperature, the results shown in Figure C-1.2 reflect the close agreement between the calculated and actual fuel pellet temperatures.

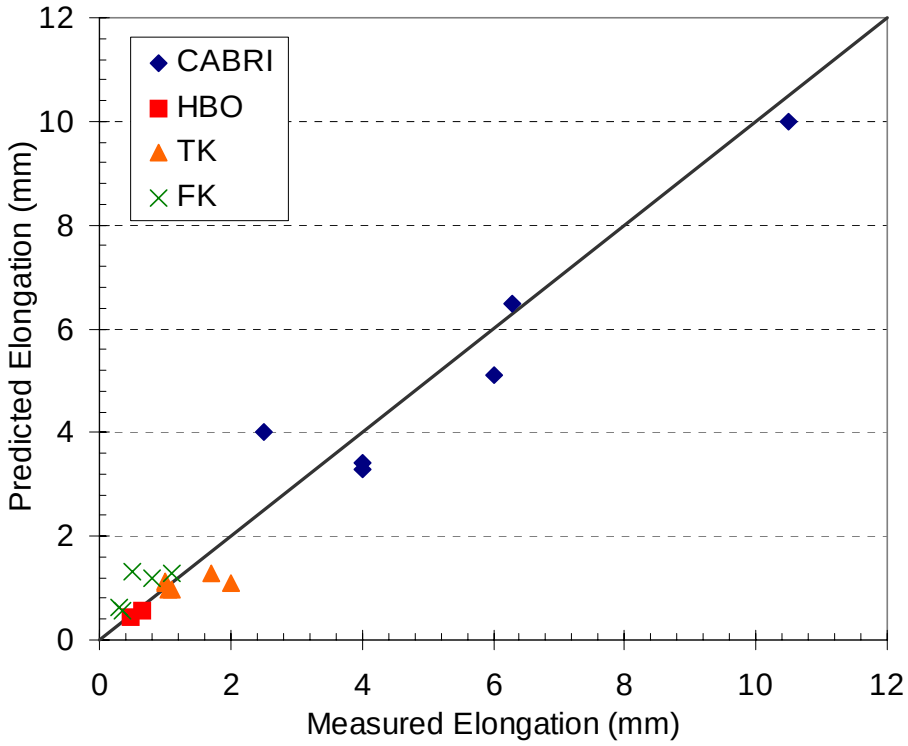

Figure C-1.2 Comparison of FALCON calculated peak cladding elongation with the measured values for the CABRI and NSRR experiments

A second confirmation of the accuracy of the FALCON fuel temperature calculations is the ceramography data from the CABRI REP Na-2 experiment. The rod average burnup for REP Na-2 is 33 GWd/tU and the peak pellet burnup is 42.5 GWd/tU. The FALCON calculated peak pellet temperature for REP Na-2 is 2796°C at a radial position of 3.895 mm or ~130 microns from the pellet periphery. This is within 15°C of the local melting temperature. Figure C-1.3 contains a photomicrograph of the pellet in the peak power region after the experiment [C-1.7]. No evidence of pellet melting was observed in any of the photomicrographs taken for REP Na-2. These results further validate the pellet temperatures calculated by FALCON.

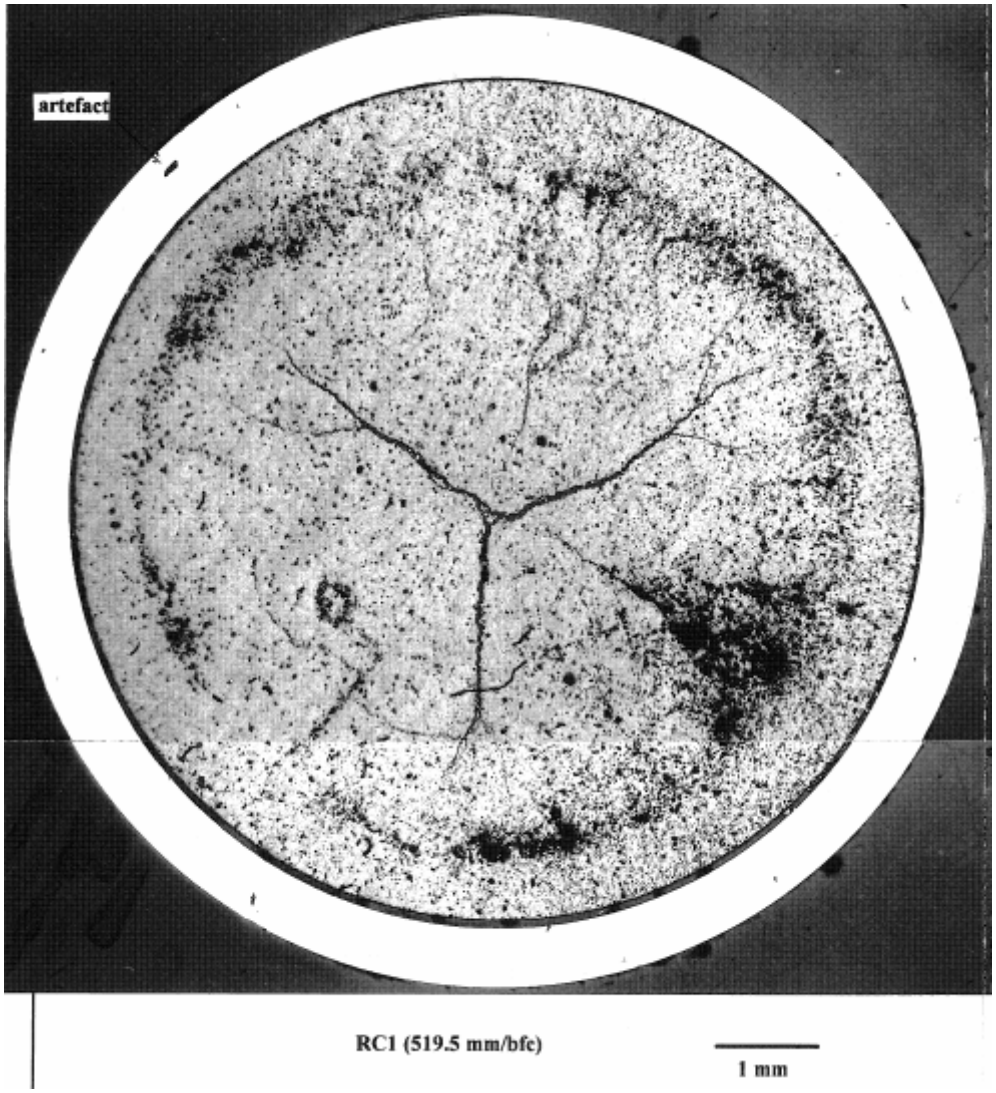

Figure C-1.3: Ceramograph of the UO_2 Fuel Pellet from the Peak Power Location of REP Na-2 [C-1.7]

Sensitivity of the Calculated Fuel Temperature to the UO_2 Thermal Conductivity Correlation for RIA Conditions

The effect of the UO_2 thermal conductivity correlation on the calculation of the fuel temperature in high burnup fuel under RIA conditions has been performed using three different correlations available in the literature. The evaluation used the FALCON BETA-RIA default UO_2 thermal conductivity correlation (MATPRO-11 [C-1.3] with the ESCORE burnup correction [C-1.4]) the latest thermal conductivity correlation in FRAPTRAN [C-1.5] and the recent thermal conductivity correlation developed for the latest version of FALCON from the NFIR [C-1.6,7] thermal diffusivity data obtained from high burnup fuel. The details of the three UO_2 thermal conductivity correlations are given in Appendix C-1.A. Two sets of FALCON analyses were conducted to evaluate the effect of the UO_2 thermal conductivity correlation on the peak fuel temperature and the radial average fuel enthalpy, both at a rod average burnup of 60 GWd/tU (66 GWd/tU pellet average). In the first set, the same injected energy (195 cal/g at PPN) was used, while the second set involved varying the injected energy to achieve approximately the same maximum fuel temperature.

The first analysis set is one of the cases used in the definition of the coolability limit proposed in the RIA Topical Report. The injected energy at the end of the power pulse is 195 cal/g, with a pulse width of 20 ms (FWHM). Table C-1.1 compares the FALCON results for the different UO_2 thermal conductivity correlations. For the MATPRO-11/ESCORE correlation, FALCON calculates a stored energy of 199.84 cal/g and a peak temperature of 2775°C in the pellet periphery region, which is approximately 15°C below the melting temperature of 2790°C. Using the FRAPTRAN and NFIR models, the calculated peak fuel temperature just reaches the melting temperature locally in the pellet periphery region. The radial average peak fuel enthalpy is also slightly higher (~0.5 cal/gm) because of the higher pellet temperatures. For the FRAPTRAN and NFIR correlations, FALCON BETA-RIA calculates that the peak pellet temperature is at the melting temperature for about 5 milliseconds before heat conduction decreases the temperature.

Table C-1.1: Comparison of FALCON results for peak temperature and radially averaged peak stored energy for different fuel thermal conductivity models: MATPRO, FRAPTRAN and NFIR

UO_2 Thermal conductivity correlation	Max. Radial Average Fuel Enthalpy (cal/g) at 0.091 s	Max Temp (°C) at 0.085 s	Temperature Difference from MATPRO (°C)
MATPRO-11/ESCORE	199.84	2774.7	-
FRAPTRAN	200.39	2790 (melt)	15.3
NFIR	200.45	2790 (melt)	15.3

In the second analysis set, the cases using the FRAPTRAN and NFIR correlations were reanalyzed using a power pulse with an injected energy of 192 cal/g and a 20 millisecond pulse width. The peak pellet temperature and the maximum radial average fuel enthalpy are given in Table C-1.2. Note the results for the baseline FALCON BETA-RIA correlation are shown for comparison. The peak pellet temperatures calculated using FRAPTRAN and NFIR correlations are within 4°C of the temperature calculated by FALCON BETA-RIA using the MATPRO-

11/ESCORE correlation. The calculated maximum radial average fuel enthalpy for the FRAPTRAN and NFIR correlations is 2.26 cal/g less than the MATPRO-11/ESCORE correlation.

Table C-1.2: Comparison of FALCON results for peak temperature and radially averaged peak stored energy for different fuel thermal conductivity models: MATPRO, FRAPTRAN and NFIR.

UO_2 Thermal conductivity correlation	Max. Radial Average Fuel Enthalpy (cal/g) at 0.091 s	Max Temp (°C) at 0.085 s	Temperature Difference from MATPRO (°C)
MATPRO-11/ESCORE	199.84	2774.7	-
FRAPTRAN	197.58	2778.3	3.6
NFIR	197.58	2772.2	-2.5

This evaluation shows that using the most recent FRAPTRAN or NFIR UO_2 thermal conductivity correlations would reduce the coolability limit by less than 3 cal/g in order to achieve the same 15°C margin to the melting temperature that was obtained in the original effort to develop the coolability limit. The variation of ~3 cal/gm caused by the uncertainty in the UO_2 thermal conductivity is the same magnitude of uncertainty identified for the gap conductance and pulse width parameters as described in Section 4 of the Topical Report.

Based on the correlations given in Appendix C-1.A, the MATPRO-11/ESCORE UO_2 thermal conductivity correlation results in a higher thermal conductivity than the FRAPTRAN and NFIR correlations, particularly for temperatures above 2500°C. Figure C-1.3 shows the calculated UO_2 thermal conductivity values as a function of position across a 17x17 pellet model at the time of the peak temperature. The UO_2 thermal conductivity profile is based on the local fuel temperatures shown in Figure C-1.5. The MATPRO-11/ESCORE thermal conductivity correlation is higher than that of the FRAPTRAN correlation across the entire pellet with the largest variation occurring at the highest temperature location, which is in the pellet periphery. The NFIR correlation thermal conductivity values are lower than the MATPRO/ESCORE correlation in the inner portion of the pellet, which corresponds to temperatures below 2400°C. Above this temperature, the NFIR thermal conductivity increases to a value slightly above that of the MATPRO-11/ESCORE model as the temperature approaches 2800°C. As shown in Appendix C-1.A, the FRAPTRAN correlation has a reduced electronic conduction term at higher temperatures (>2400°C) as compared to either the older MATPRO-11/ESCORE correlation or the newer NFIR correlation. This results in the 20% lower thermal conductivity in the pellet periphery. The lower electronic conduction term used in FRAPTRAN is not a result of burnup, but is based on an interpretation of high temperature thermal conductivity data.

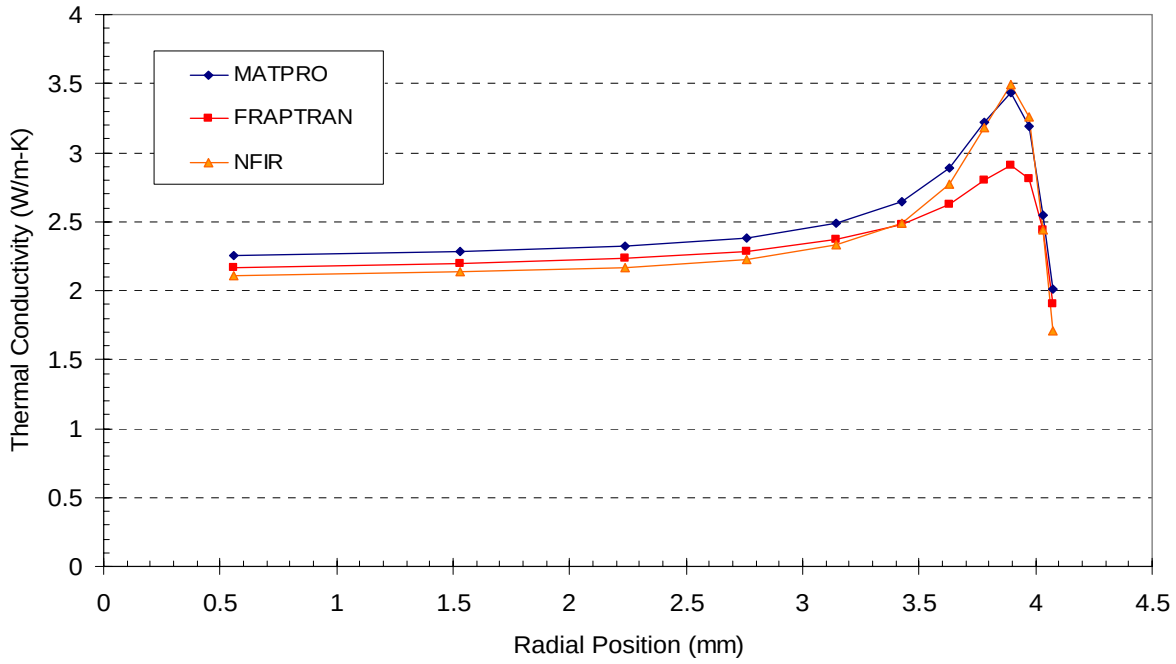

Figure C-1.4. Comparison of fuel thermal conductivities calculated by FALCON using the modified MATPRO-11, FRAPTRAN, and NFIR models with peak temperature near T_{melt}.

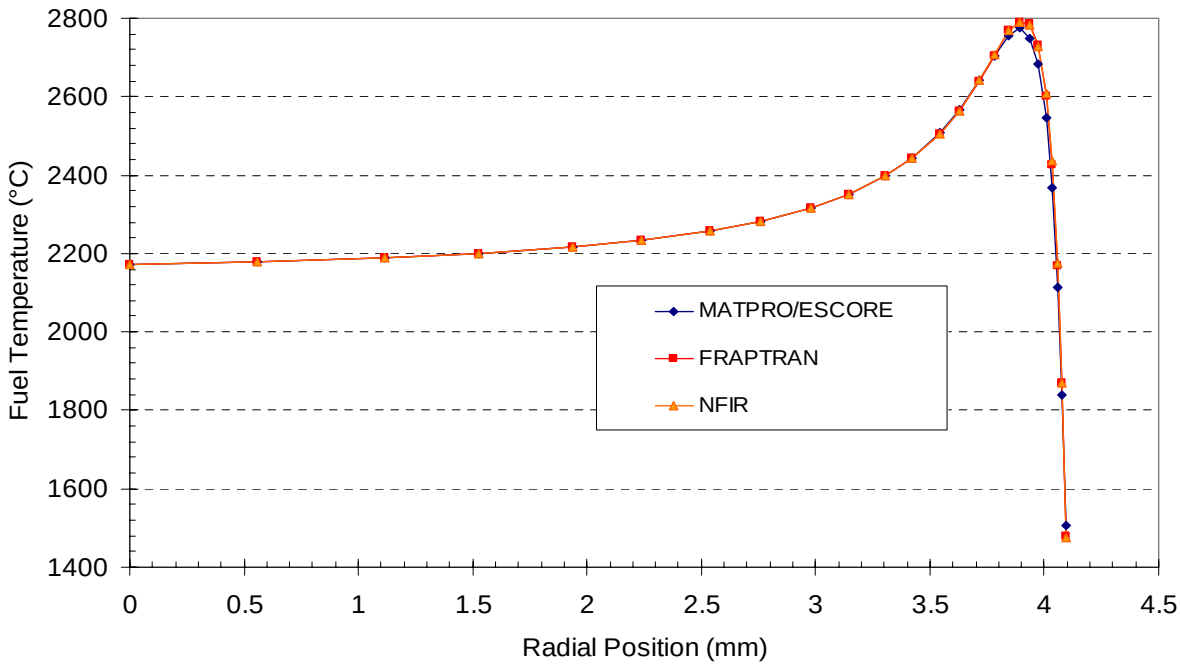

Figure C-1.5. Pellet radial temperature distributions calculated by FALCON using the MATPRO-11/ESCORE, FRAPTRAN (PNL) and NFIR models as peak temperature approaches T_{melt} with an injected fuel enthalpy of 195 cal/g.

Despite the differences in the calculated thermal conductivity across the pellet, the calculated fuel temperatures are very close, as shown in Figure C-1.5. At the peak temperature location, the difference in peak temperature is only 15°C. These results highlight the insensitivity of the fuel temperatures to large variations in UO_2 thermal conductivity, particularly for burnups greater than 40 GWd/tU. This insensitivity is a result of the adiabatic conditions experienced during the energy deposition, when the peak temperatures are reached in the pellet periphery.

Discussion

The fuel temperature during an RIA event depends mostly on the energy deposition rate, the radial power distribution, and the fuel heat capacity. Because of the almost adiabatic energy deposition, the maximum fuel temperature during an RIA event has only a weak dependency on the low temperature and high temperature fuel thermal conductivity, the pellet-cladding gap conductance, and the heat transfer across the cladding/outer surface. Sensitivity calculations contained in Section 4 of the Topical Report and summarized in this response show that the variations in the coolability limit are less than 5 cal/gm due to uncertainties in the UO_2 thermal conductivity, the pellet-cladding gap conductance, and the clad to coolant heat transfer. These results demonstrate the adiabatic nature of a rapid RIA event with a pulse width of 20 milliseconds.

References:

[C-1.1] R. O. Montgomery and Y. R. Rashid, FALCON BETA-RIA -- Fuel Analysis for Reactivity Initiated Accident, Volume 1: Theoretical and Numerical Bases, October 2002.

[C-1.2] Hagrman, D.L., "MATPRO - Version 11: A Handbook of Materials Properties for Use in the Analysis of Light Water Reactor Fuel Rod Behavior," NUREG/CR-0497 TREE-1280, February 1979

[C-1.3] Krammen, M.A., Freeburn, H. R., Eds., *ESCORE--the EPRI Steady-State Core Reload Evaluator Code: General Description*, EPRI NP-5100, Electric Power Research Institute, Palo Alto, California, February 1987.

[C-1.4] DD Lanning, CE Beyer, and KJ Geelhood, and N Gerceker, "FRAPCON-3 Code Updated With MOX Fuel Properties," ANS 2004

[C-1.5] Turnbull, J. A., "An Empirical Model of UO_2 Thermal conductivity Based on Laser Flash Measurements of Thermal Diffusivity," EPRI, Palo Alto, CA, 1998, TR-111347.

[C-1.6] *Fuel Analysis and Licensing Code: Falcon MOD01: Volume 1: Theoretical and Numerical Bases*, EPRI, Palo Alto, CA: 2004. 1011307.

[C-1.7] D. Lespieux, "Examinations Performed at the LECA on the REP Na2 Rod, Note Technique No. 95/2016, Dec. 22, 1995.

[C-1.8] J. H. Harding and D. G. Martin, "A Recommendation for the Thermal Conductivity of UO_2," Journal of Nuclear Materials, **166** (1989), 223-226.

[C-1.9] Ronchi, C., Sheindlin, M., Musella, M., and Hyland, G. J., "Thermal conductivity of uranium dioxide up to 2900 K from simultaneous measurement of the heat capacity and thermal diffusivity," Journal of Applied Physics, 85, No. 2, 15 Jan., 1999, pp.776-789.

[C-1.10] Baron, D. "Fuel Thermal Conductivity: A Review of the Modeling Available for UO_2, $(U\text{-}Gd)O_2$, and MOX Fuel," *Proceedings of OECD/NEA Seminar on the Thermal Performance of High Burnup LWR Fuel*, Cadarache, France, March 1998, p. 99.

[C-1.11] Wiesenack, W., "Assessment of UO_2 Conductivity Degradation Based on In-Pile Temperature Data," *Proceedings of the ANS International Topical Meeting on LWR Fuel Performance*, Portland, Oregon, March 2-6, 1997, p.507.

[C-1.12] Koichi Ohira and Noboru Itagaki, "Thermal Conductivity Measurements of High Burnup UO_2 Pellet and a Benchmark Calculation of Fuel Center Temperature, "*Proceedings of the ANS International Topical Meeting on LWR Fuel Performance*, Portland, Oregon, March 2-6, 1997, p.541.

[C-1.13] C. DURIEZ, J.-P. Allesandri, T. Gervais, and Y. Philipponneau, "*Thermal Conductivity of Hypostoichiometric Low Pu Content (U,Pu)O_{2-x} Mixed Oxide.*" *Journal of Nuclear Materials* **277**:143 (2000).

[C-1.14] J. Carbajo, G.Yoder, S. Popov, and V. Ivanov, "A Review of Thermophysical Properties of MOX and UO_2 Fuels", *Journal of Nuclear Materials* **299:**181 (2001).

[C-1.15] Lassman, K., Schubert, A., van de Laar, J., Vennix, C.W.H.M., "Recent Developments of the TRANSURANUS code with emphasis on high burnup phenomena," Nuclear Fuel behavior modeling at high burnup and its experimental support, Proceedings of a Technical Committee meeting in Windermere, United Kingdom, 19-23 June 2000.

[C-1.16] Lucuta, P. G., Matzke, H., Hastings, I.J., “A pragmatic approach to modeling thermal conductivity of irradiated UO_2 fuel review and recommendations,” Journal of Nuclear Materials, 232, 1996, pg. 166-180.

Appendix C-1.A
Description of UO_2 thermal conductivity models used with FALCON

MATPRO, Version 11 with ESCORE Burnup Correction Model (FALCON Default Model)

The MATPRO-11 expression consists of a low temperature term representing phonon-phonon and phonon-defect scattering and a high temperature term representing electronic conduction. The equations from MATPRO-11 [C-1.2] for UO_2 thermal conductivity are:

$$k_{mat} = P\left[\frac{K_1}{K_2+T} + K_3 e^{K_4 T}\right] \qquad \text{for } T < 1650 \text{ K} \qquad \text{(C-1.A.1)}$$

$$k_{mat} = P\left[K_5 + K_3 e^{K_4 T}\right] \qquad \text{for } 1650 \text{ K} \le T < T_{melt} \qquad \text{(C-1.A.2)}$$

where

k_{mat}: Unirradiated thermal conductivity (W/m-K)

P: Porosity correction factor (unitless)

T: Temperature (°C)

K_1: 4040.0

K_2: 464

K_3: 0.01216

K_4: 1.867×10^{-3}

K_5: 1.91

The porosity correction factor, P, is given by

$$P = \frac{1-\beta(1-D)}{1-\beta(1-0.95)} \qquad \text{(C-1.A.3)}$$

where

β: Porosity coefficient ($2.58 - 0.58 \times 10^{-3}$ T)

D: Fraction of theoretical density (unitless)

T: Temperature (°C)

The thermal conductivity model from MATPRO-11 was developed from a large database of thermal conductivity measurements on unirradiated UO_2 material [C-1.2]. Although most of the data used to develop the MATPRO-11 expressions were obtained in the 1960's and 1970's, a recent review by Baron demonstrates that the model continues to agree well with recent thermal diffusivity measurements up to 2200 K on unirradiated UO_2 material [C-1.10].

FALCON uses the expressions given in equations C-1.A.1 through C-1.A.3 to calculate the UO_2 thermal conductivity as a function of the local temperature and porosity at each integration point within the fuel element grid. However, the expression from MATPRO-11 does not consider the effect of burnup on the thermal conductivity of irradiated material. Observations from in-pile pellet centerline temperatures measurements and post-irradiation thermal diffusivity measurements have shown that the thermal conductivity of irradiated UO_2 decreases compared to unirradiated material [C-1.11, 12]. The decrease in thermal conductivity is a result of the accumulation of fission products and lattice point defects, which increase the phonon-defect scattering sites. A number of methods have been developed to account for the effect of burnup on the thermal conductivity. Most of the recent UO_2 thermal conductivity correlations include a modification to the low-temperature phonon-defect scattering term to address burnup effects [C-1.9, 13, 14, 15, 16].

FALCON includes a burnup reduction factor on the UO_2 thermal conductivity as given in equation C-1.A.4. To be consistent with the EPRI steady state fuel performance code ESCORE, the burnup reduction factor from ESCORE has been incorporated into FALCON [C-1.1, 3]. The burnup reduction factor from ESCORE was derived from fuel centerline thermocouple measurements in Halden as a multiplier on the total thermal conductivity. The UO_2 thermal conductivity model for irradiated material in FALCON is:

$$k_{irr} = (T, P, Bu) = k_{mat}(T, P) \; f(Bu) \qquad \text{(C-1.A.4)}$$

where

$f(Bu) = 1 - 0.005\,Bu \qquad 0 \le Bu \le 20$

$f(Bu) = 0.9 - 0.004\,(Bu - 20) \qquad 20 < Bu \le 30$

$f(Bu) = 0.86 \qquad 30 < Bu$

and

Bu: Pellet average burnup (GWd/tU)

In FALCON, the MATPRO/ESCORE burnup correction for thermal conductivity applies to the entire expression, including the electron conduction term, whereas the FRAPTRAN and NFIR models apply the burnup correction term to the phonon conduction term only.

FRAPCON/FRAPTRAN Fuel Thermal Conductivity Model

Lanning et al (PNL) [C-1.4] published the latest fuel thermal conductivity model, which is based on the Duriez model [C-1.13] for the thermal conductivity, K_{95}, of unirradiated MOX fuel pellets at a nominal density of 95% theoretical density (TD), has the following form:

$$K_{95} = \frac{1}{A(x) + B(x)T} + \frac{C}{T^2}\exp(-\frac{D}{T}) \qquad \text{(C-1.A.5)}$$

where, for K_{95} in W/m-K:
x = 2.00 – O/M (oxygen-to-metal ratio)
T = temperature in K
A(x) = 2.85x + 0.035 m-K/W
B(x) = (2.86 - 7.15x)*1E-4 m/W
C = 1.689E9 W-K/m
D = 13520 K.

For unirradiated fuel pellets, this recommendation is virtually identical to that by Carbajo [C-1.14] et al. PNL's recommended burnup dependence deviates from that of Carbajo, as explained below. PNL has modified the model to include burnup dependence and a reduced high temperature term, as follows:

$$K_{95} = \frac{1}{A(x) + B(x)T + f(Bu) + G(bu,T)} + \frac{C_{\text{mod}}}{T^2}\exp(-\frac{D}{T}) \qquad \text{(C-1.A.6)}$$

where
G(Bu,T) = [1-0.9exp(-0.04Bu]g(Bu)h(T)

x, T, A(x), B(x), and D are as defined above for equation (C-1.A.5),
Bu = local (radially as well as axially) burnup in GWd/tHM
f(Bu) = effect of fission products in crystal matrix (solution) = 0.00187•Bu
g(Bu) = effect of irradiation defects = $0.038 \cdot Bu^{0.28}$
h(T) = temperature dependence of annealing on irradiation defects = $\frac{1}{1 + 396e^{-Q/T}}$
Q = 6380 K
C_{mod} = 1.5E9 W-K/m.

The PNL correlation was multiplied by 1.0789 to obtain the appropriate conductivity for 100% TD, and then the appropriate porosity correction was applied within the FALCON code.

NFIR UO_2 Thermal Conductivity Model

The NFIR thermal conductivity model provides a more accurate treatment of the burnup on fuel thermal conductivity than the MATPRO-11 model discussed above. The NFIR thermal conductivity model in FALCON is a modified version of an empirical expression developed by Turnbull [C-1.6] from thermal diffusivity measurements performed using miniature UO_2 specimens irradiated to burnup levels between 28 and 80 GWd/tU. Details of the original thermal conductivity expression are contained in Reference C-1.5.

As with the MATPRO and PNL models, the heat conduction through the fuel is modeled as a combination of lattice conduction by phonons and electron conduction, both of which are temperature dependent. Based on this, the general formula for thermal conductivity is given by:

$$K = K_{ph} + K_{el} \tag{C-1.A.7}$$

The lattice conduction by phonons (K_{ph}) is represented empirically by:

$$K_{ph} = \frac{1}{A + BT} \tag{C-1.A.8}$$

where the model coefficient A describes the effect of phonon scattering by lattice impurities or discontinuities and the model coefficient B describes the effects of phonon-phonon collisions.

The electron conduction (K_{el}) is given by:

$$K_{el} = Ce^{DT} \tag{C-1.A.9}$$

where the model coefficients C and D have been determined empirically by Christensen.

Thermal diffusivity experiments on both irradiated UO_2 and unirradiated UO_2 material containing simulated fission products indicate that both the coefficients A and B in eq. C-1.A.8 are a function of burnup [14,15]. Turnbull used experimental results obtained from thermal diffusivity measurements on UO_2 samples irradiated at temperatures below 800ºC and burnups between 28 and 67 GWd/tU to determine the coefficients A and B as a function of burnup. The thermal diffusivity experiments used by Turnbull to develop the burnup dependency of the A and B coefficients displayed a measurable recovery of the thermal conductivity upon heating to temperatures above 800ºC due to annealing of fission products and point defects [C-1.5]. As a result, the coefficients A and B have a complex burnup dependency that includes an empirical function representing the thermal recovery process. The resulting thermal conductivity as a function of burnup is given by;

$$K(Bu) = (1 - F) \cdot K_{start} + F \cdot K_{end} + K_{el} \tag{C-1.A.10}$$

where K_{start} is the lattice conductivity before thermal recovery, K_{end} is the lattice conductivity after recovery, F is the empirically-derived thermal recovery function, and K_{el} is given by eq. C-1.A.9. The lattice conductivity before thermal recovery is given by;

$$K_{start} = \frac{1}{A_1 + A_2 \cdot Bu + A_3 \cdot Bu^2 + \left[B_1 + B_2 \cdot Bu\right] \cdot T} \tag{C-1.A.11}$$

where the model coefficients A_1, A_2, A_3, B_1, and B_2 are shown in Table C-1.A.1, Bu is the local (radially across the pellet) burnup in GWd/tU, and T is temperature in ºC. Similarly, the lattice conductivity after thermal recovery is given by;

$$K_{end} = \frac{1}{A_1 + A_4 \cdot Bu + \left[B_1 + B_3 \cdot Bu\right] \cdot T} \qquad \text{(C-1.A.12)}$$

where the model coefficients A_4 and B_3 are shown in Table C-1.A.1.

The thermal recovery function, F, was developed to represent the transition between no recovery of irradiation damage and full recovery of irradiation damage. The function is given by;

$$F = 0.5\left(1 + \tanh\left(\frac{T - 900}{150}\right)\right) \qquad \text{(C-1.A.13)}$$

As can be seen by eq. C-1.A.13, the thermal recovery process is completed by ~1200ºC.

Table C-1.A.1

Model Coefficients for the Modified NFIR UO_2 Thermal Conductivity Model

Model Constant	Value
A1	9.592E-2
A2	6.14E-3
A3	-1.4E-5
A4	2.6E-3
B1	2.5E-4
B2	-1.81E-6
B3	-2.7E-7
B4	-1.268763E-2
C	1.32E-2
D	1.88E-3

Comparison of UO_2 Thermal Conductivity Models

In addition to the fuel temperature sensitivity evaluation, a comparison of the default FALCON (MATPRO-11/ESCORE) thermal conductivity model to other UO_2 thermal conductivity models available in the literature has been performed in order to see what differences exist. A review of the literature finds numerous approaches or mathematical expressions for calculating fuel thermal conductivity. Furthermore, there is considerable scatter in the data, and a lack of experimental measurements at temperature > 2500°C.

The uranium dioxide thermal conductivity is required to calculate the temperature distribution across the fuel pellet. The thermal conductivity of unirradiated uranium dioxide is primarily a function of temperature and porosity. Irradiation further reduces thermal conductivity for temperatures below approximately 1800°C.

The thermal conductivity of UO_2 is a function of two phenomena: 1) phonon-phonon conduction and 2) electron (small polaron) conduction. The former involves heat transport by virtue of atomic vibration and dominates the conductivity for temperatures less than 1377°C (1650 K); the latter involves conduction by electrons surrounding the atoms and dominates heat conduction for temperatures above 1377°C (1650 K). As the temperature of the UO_2 ceramic increases, the phonon conduction is less effective, whereas the electron conduction becomes more effective. Furthermore, the phonon conduction is affected by the accumulation of burnup, whereas the electron conduction is not.

Various correlations have been devised over the years [C-1. 8 through C-1.16]. Some have used polynomial fits to data taken from thermal diffusivity measurements over the full range of temperature, while other correlations use separate terms for the phonon-phonon and electron conduction processes. The phonon conduction term usually takes the form of an inverse linear function, e.g. 1/(A + B*T); the electron conduction term has a variety of exponential or polynomial expressions. The different correlations do not necessarily coincide over the full range of temperature (200 – 2840°C (melting temperature)).

The different models yield slight differences in local temperature as a function of temperature and burnup. The thermal conductivities of the three models used in the maximum temperature sensitivity study are compared along with the Ronchi model in Figures C-1.5 and C-1.6 for burnups of 40 and 65 GWd/tU, respectively. The models show very good agreement for a burnup of 40 GWd/tU and reasonably good agreement at 65 GWd/tU. The MATPRO-11 correlation shows a slightly greater conductivity than the PNL (FRAPCON/FRAPTRAN) correlation, but less than the Ronchi model. Comparing these results with those of the temperature predictions in Figure C-1.4, one may conclude that the differences among the MATPRO, PNL and NFIR models do not lead to significant differences in the prediction of maximum temperature during an RIA event.

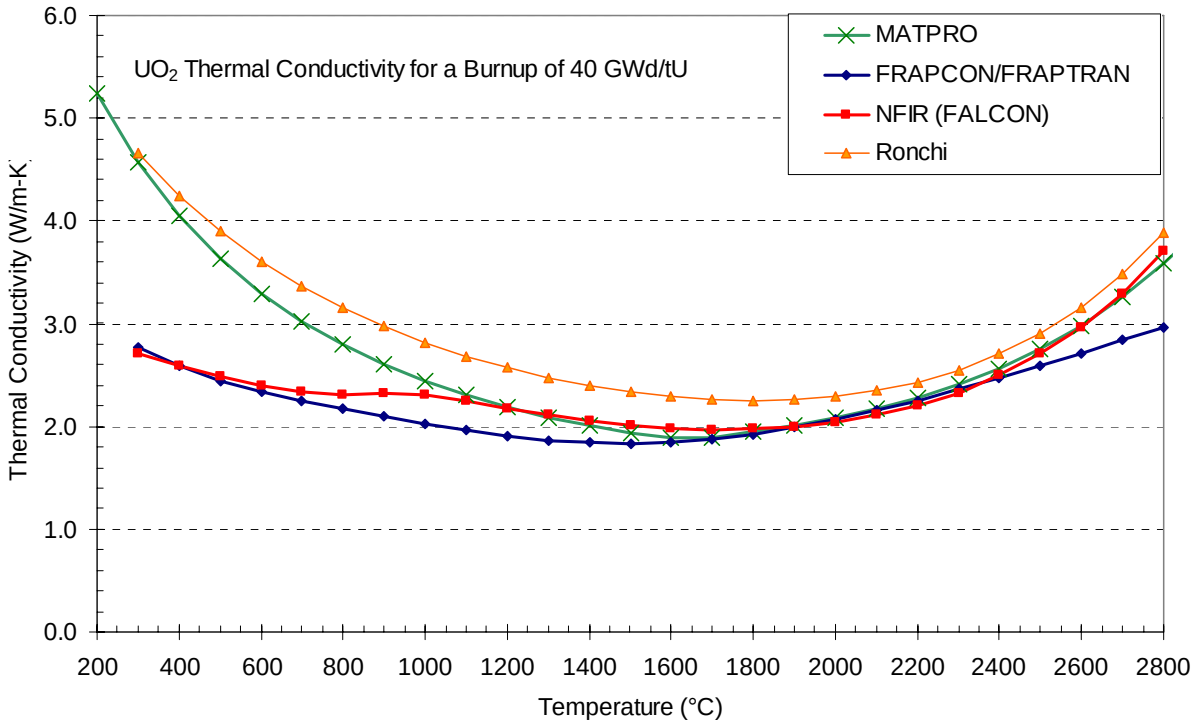

Figure C-1.A.1: Thermal Conductivity as a Function of Temperature for a Burnup of 40 GWd/tU.

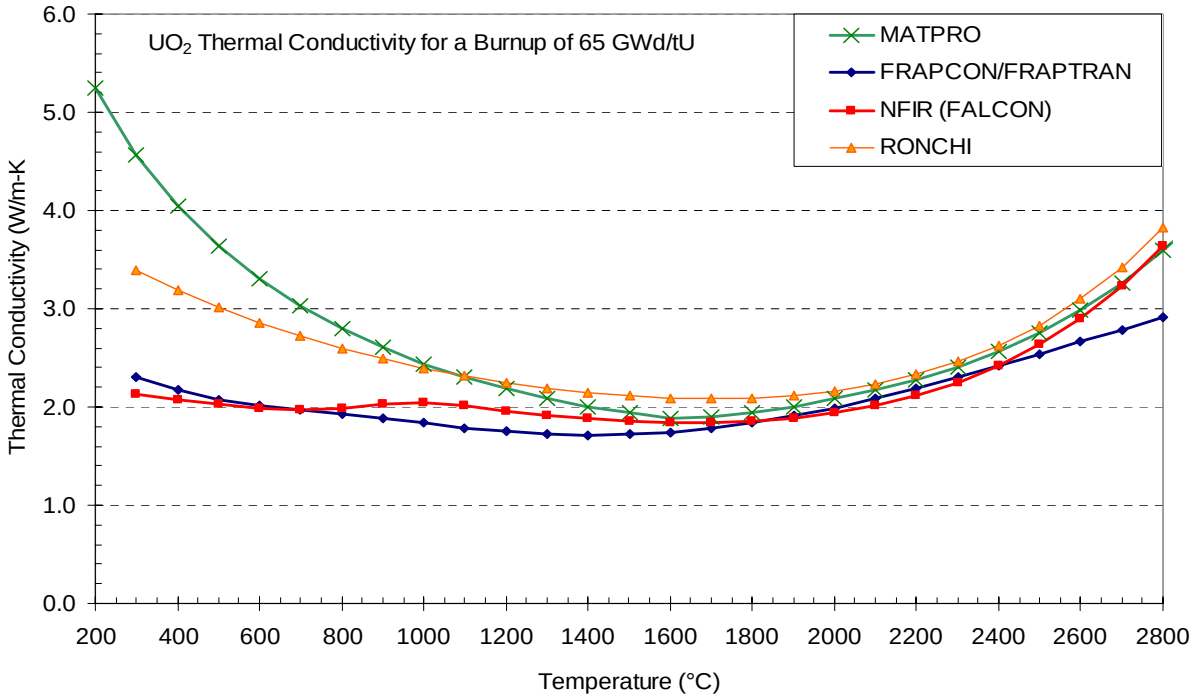

Figure C-1.A.2: Thermal Conductivity as a Function of Temperature for a Burnup of 65 GWd/tU.

In the version of FALCON used for the development of RIA acceptance criteria, the MATPRO [vers. 11] subroutine FTHCON is used in the calculation of fuel thermal conductivity. A burnup correction factor from the ESCORE model is used to account for burnup effects on conductivity. Figure C-1.A.3 shows a comparison of the electron conduction terms used in MATPRO-11, FRAPTRAN (PNL), NFIR and several other correlations. The MATPRO-11 and NFIR models use the same form proposed by Christensen,

$$K_{el} = C e^{DT},$$

but with different coefficients. The NFIR model predicts slightly higher thermal conductivity.

The FRAPTRAN (PNL) has the form, $\frac{C}{T^2} * e^{-D/T}$, and is based on a modification of the Duriez model [C-1.13], namely by a reduced pre-exponential term 'C'. The Duriez model was itself based on the form proposed by Harding and Martin[C-1.8], although the coefficients were quite different.

The Ronchi correlation [C-1.9] uses a form, $\frac{C}{T^{5/2}} * e^{-D/T}$. Interestingly, between the temperatures 1800°C and 2600°C, the MATPRO-11 electron conductivity is less than the Ronchi correlation.

One correlation developed by NFI [C-1.12], uses a quartic expression for the electron conduction term ($C T^2 + D T^4$).

The MATPRO-11 correlation provides the lowest thermal conductivity over the range of temperatures 1800 – 2600°C, which are typical for maximum fuel temperatures during an RIA event.

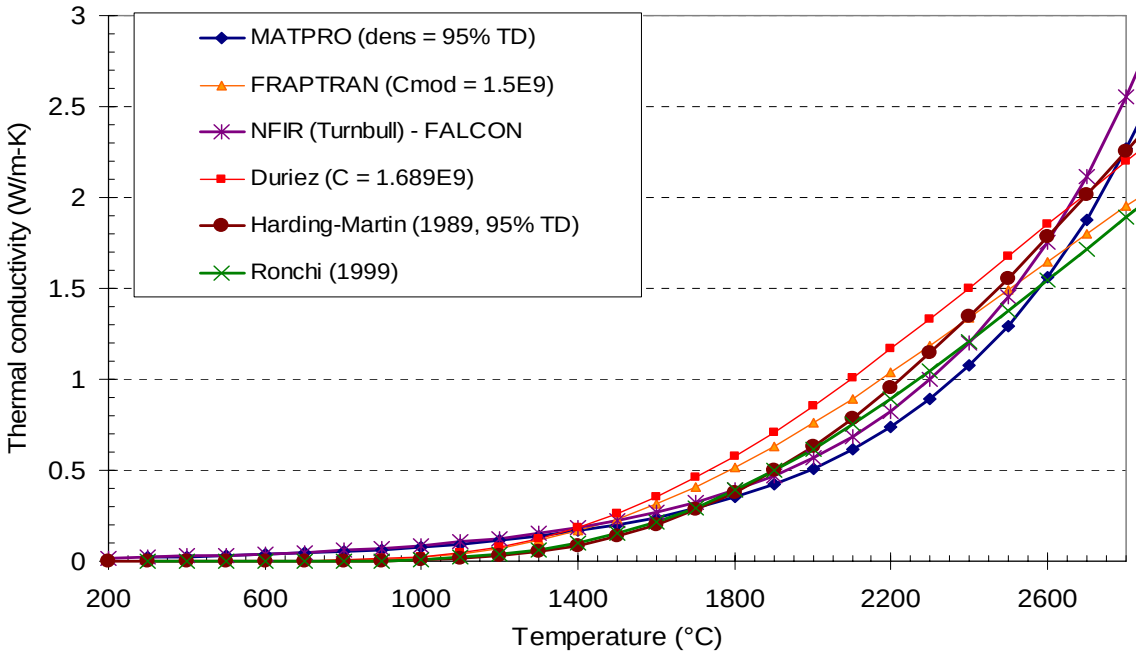

Figure C-1.A.3. Electron conduction term for various thermal conductivity models as a function of fuel temperature.

Response to Requests for Additional Information (RAI's)
NRR Safety Evaluation Report – Project No. 689

C-2. The Topical Report discusses the impact of gadolinia on the proposed fuel coolability limit but does not address the impact other poisons such as erbia.

Response to RAI C-2

The approach used in the RIA Topical Report EPRI 1002865 to evaluate the effect of gadolinia burnable poison on the fuel coolability limit was to identify the impact of gadolinia on the radial distribution of the burnup and the local melting temperature at a pellet average burnup levels of 40 GWd/tU and 75 GWd/tU. The TUBRNP model was used to calculate the radial burnup distribution for a 4.95 wt%^{235}U enriched pellet with 8 wt%Gd_2O_3 and without gadolinia. Some differences in the radial distribution of burnup were calculated with the TUBRNP model. The variation in burnup distribution between a 8 wt% gadolinia pellet and a non-gadolinia pellet resulted in a decease in the local melting temperature of less than 15°C for burnup levels evaluated in the report. This analysis was performed assuming that the unirradiated melting temperature is the same for UO_2 and UO_2-Gd_2O_3 pellet at 8 wt% gadolinia. Based on this evaluation, it was determined that the impact of gadolinia enrichment up to 8 wt% would be less than 5 cal/gm on the revised fuel coolability limit.

Erbia (Er_2O_3) is also used as a burnable poison in LWR fuel rods for reactivity control. References C-2.1 and C-2.2 provide a description of erbia use as an integral burnable absorber in UO_2 fuel pellets. Because of the magnitude and energy dependence of the neutron capture cross-sections of erbium, lower concentrations of erbium are required to obtain the appropriate reactivity worth and depletion rate for PWR applications. Erbia concentrations are typically less that 2.5 wt% for pellet enrichments of 4.0 to 4.5 wt%^{235}U. By using lower concentrations of erbia, the material properties and local power peaking are not significantly different than UO_2 characteristics. The impact of 2.5 wt% erbia on the radial power peaking is much less than that for 8 wt% gadolinia. Westinghouse reports that the effect of erbia on the pellet melting temperature is a decrease of 5.8°C per wt% erbia, which is less that 15°C below the unirradiated UO_2 melting temperature for 2.5wt% erbia enrichment [C-2.3].

The impact of erbia on the fuel coolability limit is bounded by the 8 wt% gadolinia assessment, which showed a decrease of less than 5 cal/gm at pellet average burnup levels of 40 and 75 GWd/tU.

References

C-2.1 Crosetti, L.V., Hatfield, S.C., and Jonsson, A., "Recent Advances in PWR Fuel Design at ABB-CE," Proceedings of the International Topical Meeting on LWR Fuel Performance, Avignon, France, April 21-24, 1991, pg 113-121.

C-2.2 Fiero, I.B. et. al., "Status of Erbium Burnable Absorber Development at ABB Combustion Engineering Nuclear Fuel," Proceedings of the International Topical

Meeting on Light Water Reactor Fuel Performance, West Palm Beach, Florida, April 17-21, 1994, pg 667-673.

C-2.3 Mitchell, D., Private Communication, 2003.

Response to Requests for Additional Information (RAI's)
NRR Safety Evaluation Report – Project No. 689

C-3. Although we believe there may be a justifiable coolability limit at an enthalpy above the Research Information Letter (RIL)-0401 cladding failure threshold, we cannot accept the proposed limit because of the lack of experimental data. Assertions are made about limited amounts of fuel dispersal, small magnitude of pressure pulses, and inefficient energy conversion of non-molten particles. However, these assertions are based mostly on tests in the Nuclear Safety Research Reactor (NSRR) with medium-to-high-burnup specimens under conditions that are far from typical for a nuclear power plant. No analysis is presented that would allow one to interpret these data or to compare predicted light-water reactor pressure pulses with vessel limits. We do not believe it is adequate to assume that molten fuel is needed to produce an energetic fuel-coolant interaction and then use a burnup-dependent melt enthalpy as the limit.

Response to RAI C-3:

Introduction
The Topical Report contains an assessment of the potential consequences of the dispersal of non-molten fuel particles into the coolant following cladding failure (Section 4.1.3 and Section 4.2.1). The discussion reviews the experimental results from tests that resulted in both molten and non-molten fuel dispersal during a RIA-simulation experiments as well as ex-reactor fuel-coolant interaction experiments performed to study mechanical energy generation during severe core accidents. The review concludes that dispersal of finely fragmented non-molten fuel particles from high burnup fuel is not a coolability issue for the following technical reasons:

- No fuel dispersal is expected after cladding failures for pulse widths above 10 milliseconds
- The amount of material that is available for dispersal is small.
- The mechanical energy conversion is less efficient for non-molten fuel particles
- Fuel-coolant interaction is less efficient in reactor coolant pressure and temperature conditions

Based on these technical reasons, the Topical Report further concludes that the consequence of dispersing a small amount of finely fragmented non-molten fuel material into the coolant is a radiological release issue, not a coolability issue.

The following discussion addresses the two key observations/questions contained in the RAI:

(1) The lack of data to support the proposed coolability limit
(2) The lack of analytical evaluations of the NSRR mechanical energy generation data to allow for the interpretation of the experimental results and the application of the NSRR observations to LWR conditions.

The sections below describe the experimental data that supports the proposed coolability limit and the analytical evaluations performed to assess the consequences of fuel-coolant interaction following dispersal of non-molten fuel material.

Industry Evaluation

The industry believes that both the experimental database and analytical evaluations available support the technical basis for the proposed coolability limit described in the Topical Report. More than 75 RIA-simulation experiments in the burnup range between zero and 78 GWd/tU have been performed up to radial average peak fuel enthalpy levels that are well above the RIL-0401 cladding failure threshold. Of these tests, approximately a third (24 test rods) failed by PCMI related mechanisms during the power deposition. Another 10 to 12 tests failed by high temperature failure mechanisms related to operation in departure from nucleate boiling (DNB) conditions following the energy deposition, i.e. ballooing/burst or oxidation-induced embrittlement. In a majority of the tests above the RIL-0401 failure threshold, the fuel rods maintained their rod geometry up to radial average peak fuel enthalpy levels approaching 220 cal/gm with little or no consequence other than the development of a through-wall crack. In a few cases from the NSRR test facility, end effects caused the fracturing of the test rod into several pieces due to separation of the lower or upper end plugs. This is not unexpected because the short test rod length (~5 inches) and uniform axial power profile used in the NSRR tests force an axial cladding crack to extend into the heat affected zones near the lower and upper end plugs.

Of the test rod failures that reside above the RIL-0401 failure threshold, approximately two-thirds (15) of the rods that failed by PCMI experienced some amount of fuel dispersal. The amount of fuel that was dispersed was less than 20% of the total UO_2 pellet loading for the tests that did not fracture the lower end plug weld. All the test rods that experienced fuel dispersal were tested at pulse widths less than 10 milliseconds, supporting the conclusions of the Topical Report. All test rods with fuel dispersal had burnup levels exceeding 30 GWd/tU. It should be noted that some PCMI failures at pulse widths less than 10 milliseconds did not disperse any fuel up to burnup levels of 38 GWd/tU. None of the test rods that failed by high cladding temperature related processes (ballooing/burst or oxidation-induced embrittlement) resulted in non-molten fuel material dispersal up to 230 cal/gm, even though several were tested at pulse widths below 10 milliseconds.

Based on the understanding that the pulse width varies inversely with the amount of reactivity insertion and deposited energy (Nordheim-Fuchs relationship), it is recognized that pulse widths less than 10 milliseconds may be required to reach fuel enthalpy levels above the proposed failure threshold in the Topical Report. As a result, fuel dispersal is likely following cladding failure for such high enthalpy levels for rods that exceed a peak burnup of 30 GWd/tU.

The technical assessment in the Topical Report also considered the consequences of fuel dispersal following cladding failure. The assessment focused on the generation of mechanical energy through coolant pressure pulses as a result of fuel-coolant interaction (FCI). By comparing the consequences between tests with dispersal of non-molten fuel particles with those from tests with dispersal of molten fuel, it was demonstrated that the mechanical energy

generation from the dispersal of molten fuel is at least an order of magnitude larger than for the dispersal of non-molten material. In most tests with dispersal of molten fuel material, partial or complete loss of rod geometry was observed in post test examinations. Based on this assessment, the coolability limit was established to preclude local pellet melting by limiting the maximum radial average peak fuel enthalpy. The assessment contained in the Topical Report is consistent with that performed by the Japanese Safety Authority, which also developed a coolability limit based on precluding fuel melting [C-3.1 and C-3.2]. A comparison of the coolability limit proposed in the Topical Report and the Japanese limit is shown in Figure C-3.1. The two limits shown in Figure C-3.1 are very similar.

Assessment of Core Coolability Consequences with Non-molten Fuel Dispersal

Although the Topical Report did not include analytical evaluations of the consequences of non-molten fuel material under light-water reactor (LWR) conditions, it has relied on several evaluations that have been performed by others. These assessments include both thermal-hydraulic and computational fluid dynamics (CFD) calculations of hypothetical events in LWR as well as, the direct use of the NSRR experimental results. One of the key objectives of these evaluations has been to translate the observations from fuel dispersal consequences in the NSRR experiments to fuel rod and coolant conditions typical of LWRs. In most cases, the results from these evaluations have been compared to pressure vessel limits, expressed either in terms of a maximum pressure at the pressure vessel boundary or as the maximum absorbable energy of the pressure vessel. Thermal-hydraulics and CFD calculations have been performed by EPRI [C-3.3], University of California, Santa Barbara [C-3.4], and Tokyo Electric Power Company [C-3.5]. In all of these analyses, the calculated pressure pulse generation is within the limits for the pressure vessel in the case of dispersal of non-molten material from high burnup fuel assemblies. The Japanese Safety Authority (NSCJ) has also performed an assessment of fuel rod failure by PCMI using directly the thermal-to-mechanical energy conversion ratio derived from experimental data (water velocity and pressure data) from the NSRR experiments to calculate the mechanical energy generated during a LWR event. This assessment finds that the mechanical energy generation from the dispersal of non-molten fuel material following PCMI cladding failure is well within the pressure vessel limits for both BWRs and PWRs. A summary of the NSCJ assessment is contained in Appendix C-3.A.

References

C-3.1 “Evaluation Guideline for Reactivity-Initiated Events for Power Generating Light Water Reactors,” Statement by the Nuclear Safety Commission of Japan, January 19, 1984.

C-3.2 “High Burn-up Fuel In the Matter of Reactivity-Initiated Events for Power Generating Light Water Reactors,” Statement by the Nuclear Safety Commission of Japan, April 13, 1998.

C-3.3 Montgomery, R. O. and Y. R. Rashid, "Evaluation of Irradiated Fuel During RIA-Simulation Tests", EPRI TR-106387, May 1996.

C-3.4 Yuen, W.W., and Theofanous, T.G., "A Scoping CFD Evaluation of RIA Consequences," http://www.crss.ucsb.edu/imust/yuen/NRC_2000-01.html.

C-3.5 Azuma, M., et. al., "Assessment on Integrity of BWR Internals Against Impact Load by Water Hammer Under Conditions of Reactivity Initiated Accidents," Nuclear Technology, Vol. 149, March 2005.

C-3.6 Lipinski, R. L., "A Coolability Model For Postaccident Nuclear Reactor Debris," Nuclear Technology, Vol. 65, April 1984, pp. 53-66.

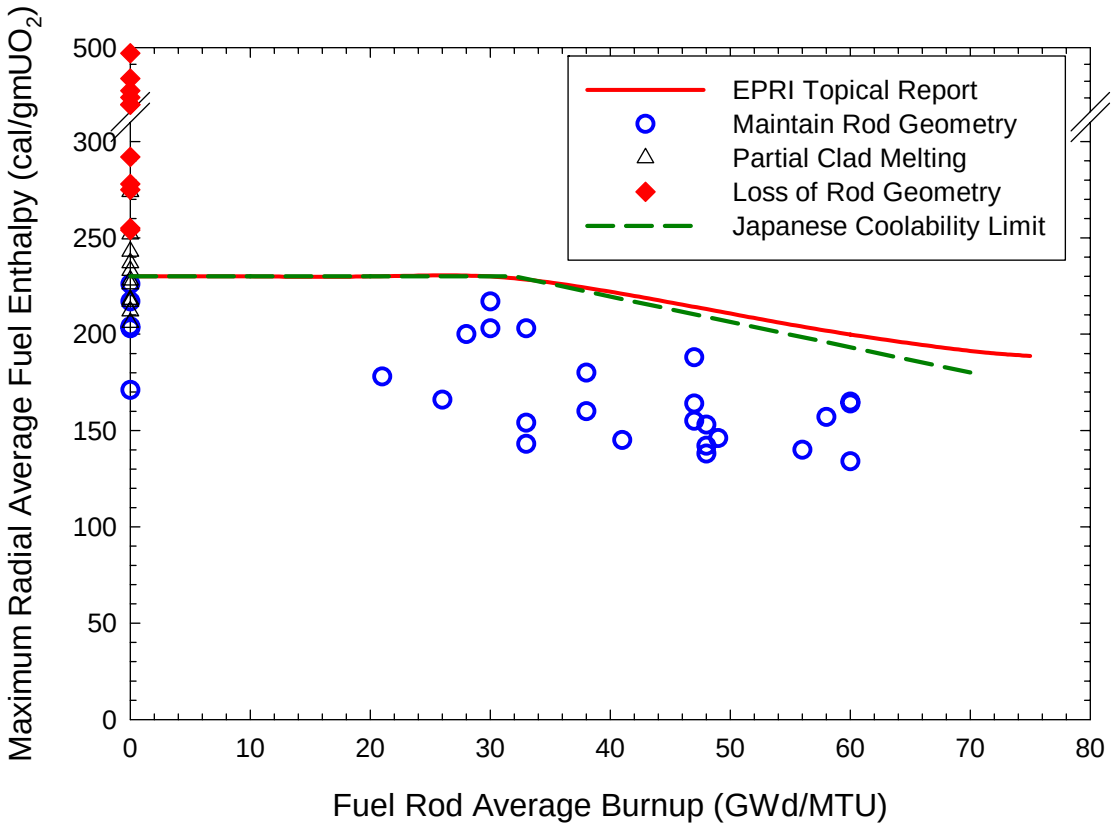

Figure C-3.1 Comparison of the Coolability Limit Proposed in the EPRI Topical Report and the Japanese Coolability Limit [C-3.2]. Selected high fuel enthalpy test rods shown for comparison.

Appendix C-3.A
Nuclear Safety Commission of Japan (NSCJ) Assessment of Failure of High Burnup Fuel During a Reactivity Initiated Accident

The Nuclear Safety Commission of Japan (NSCJ) issued an Evaluation Guideline for Reactivity Initiated Events (RIE Evaluation Guideline) in January 1984 that describes the criteria and methodology to evaluate the impact of RIA events in Light Water Reactors [C-3.1]. The RIE Evaluation Guideline contains a cladding failure threshold as a function of rod internal pressure and a limit on fuel enthalpy to prevent pressure pulse generation from the dispersal of molten/evaporated fuel material. In addition, Attachment 2 of this guideline includes an assessment of the impact of mechanical energy release from rupture of waterlogged fuel rods on the structural integrity of the reactor pressure vessel and shutdown capability of the reactor. This earlier assessment found that the mechanical energy release from rupture of waterlogged fuel rods (impulse pressure) was below 10% of the absorbable energy of the reactor vessel for both PWR and BWR reactors.

Following the conduct of additional RIA-simulation tests on high burnup fuel segments, the NSCJ performed an assessment of the RIE Evaluation Guideline in light of the additional data from high burnup fuel [C-3.2]. The assessment included the development of a burnup dependent failure threshold for PCMI cladding failure and a burnup dependent fuel enthalpy limit to prevent mechanical energy release from dispersal of molten/evaporated fuel material. Also, this new assessment included an evaluation of the consequences of cladding failure by PCMI on reactor pressure vessel integrity and reactor shutdown capability, including dispersal of non-molten fuel particles. The consequences of PCMI failure evaluated were 1) the potential for steam explosion, 2) the mechanical energy release from PCMI and waterlogged fuel failure, and 3) the coolability of fuel fragment sediment within the pressure vessel. The conclusions from the assessment of each consequence are summarized below.

Consequence #1: Potential for Steam Explosion

After reviewing temperature calculations for hypothetical RIA events in both PWR and BWRs and from RIA-simulation tests in NSRR, the NSCJ concluded that since the temperature of the fuel material dispersed from the fuel rod upon failure by PCMI is well below the melting temperature of UO_2, there is no possibility for the development of a steam explosion. This evaluation considered the burnup dependence of the UO_2 melting temperature.

Consequence #2: Mechanical Energy Release from PCMI and Waterlogged Fuel Failure

Although a steam explosion from non-molten fuel dispersal is not possible, the NSCJ recognized that the mechanical energy release following PCMI failure was not completely negligible as observed in irradiated fuel tests conducted in NSRR. Therefore, it was decided to evaluate the effects of mechanical energy release as a result of PCMI failure. The approach used for PCMI failures was the same as that developed for waterlogged rods in the original RIE Evaluation Guideline. In this approach, the mechanical energy release is separated into two components: impulse pressure resulting from release of rod pressure upon failure and water hammer (or pressure increase) caused by steam generation from fuel particle heat transfer to the coolant. Experimental data obtained from NSRR show that these two mechanical energy release mechanisms occur at different times during the event and can therefore be evaluated separately.

The thermal to mechanical energy generation ratio determined for both water hammer and impulse pressure is shown in Figure C-3.A.1 and Figure C-3.A.2, respectively for both PCMI fuel rod failures (solid symbols) and unirradiated waterlogged tests (open symbols). Also shown in Figures C-3.A.1 and C-3.A.2 is an upper bound curve derived from the unirradiated waterlogged rods (solid line) and a curve that is 50% of the upper bound curve (dashed line). The experimental data on mechanical energy release following PCMI failure show that the mechanical energy conversion ratio for both impulse pressure and water hammer is less than ~50% of the unirradiated waterlogged fuel at the same fuel enthalpy level.

To calculate the mechanical energy release from either impulse pressure or water hammer, the number of fuel rod failures by PCMI and waterlogged rods were estimated from core wide fuel enthalpy distributions for hypothetical PWR and BWR RIA events. It is conservatively assumed that 1% of the fuel rods are waterlogged at the start of the accident. The number of fuel rods exceeding the PCMI failure threshold and the waterlogged fuel rupture limit are used to estimate the amount of fuel that has failed. Using the amount of material released from the failures, the thermal energy of the dispersed material, and the mechanical energy conversion ratio, the mechanical energy release for the impulse pressure and the water hammer (or pressure increase) were calculated for different reactor designs. In this analysis, the mechanical energy conversion ratio for the PCMI failures was conservatively assumed to be the same as for the waterlogged rods. The mechanical energy release values were compared to the absorbable energy of the reactor vessel, which is the strain energy required to load the vessel material to the yield point. These comparisons find that mechanical energy release is less that 40% of the absorbable energy of the reactor vessel for BWR's and less than 3% for PWR's. Based on these results, the NSCJ concluded that the mechanical energy release following fuel rod failure by PCMI would not impact the integrity of the pressure vessel or impair the shutdown capability of BWR or PWR reactor cores.

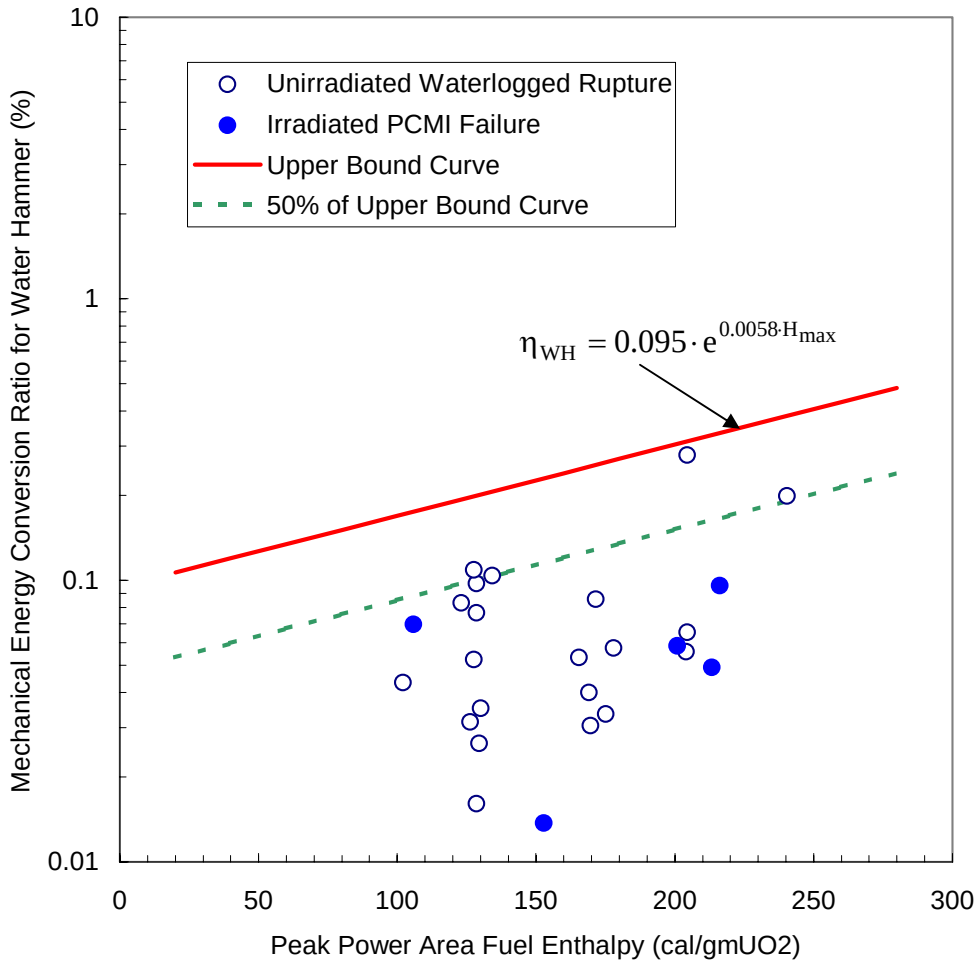

Figure C-3.A.1 Mechanical energy conversion ratio for water hammer (pressure increase) as a function of peak radial average fuel enthalpy for the NSRR tests on waterlogged fuel and irradiated fuel.

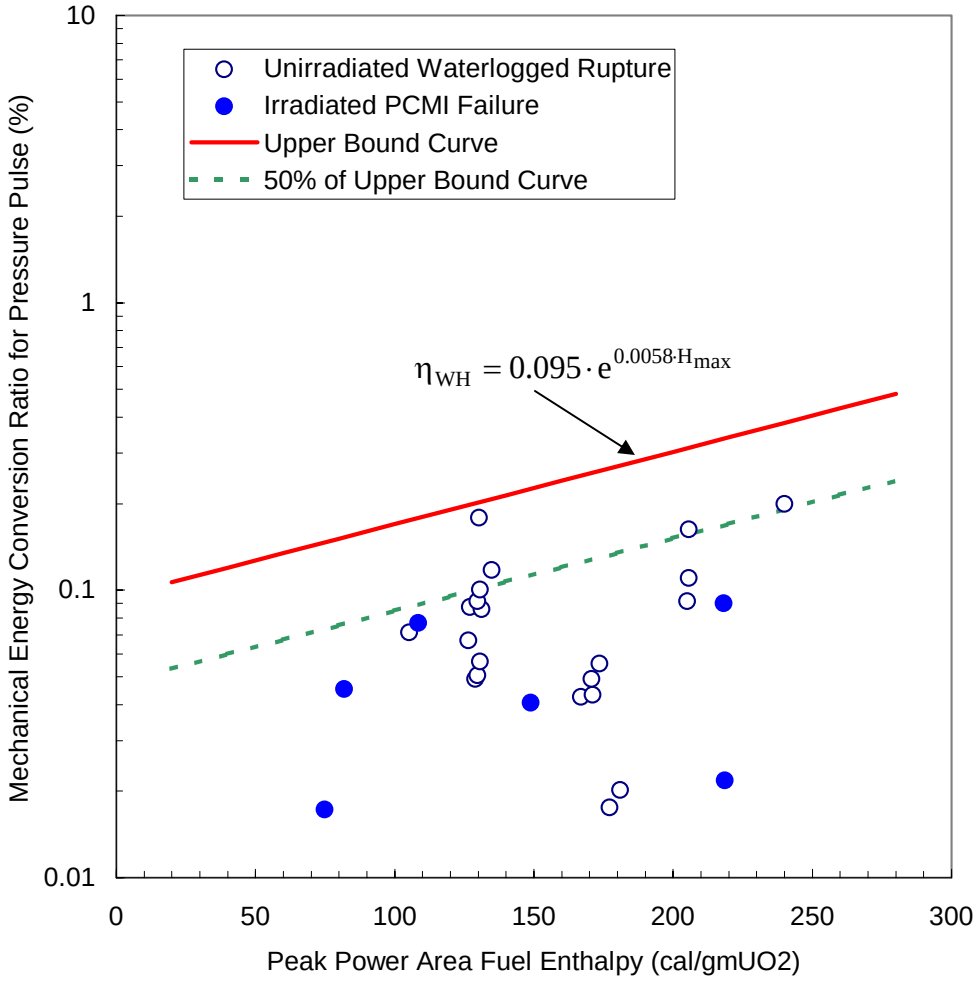

Figure C-3.A.2 Mechanical energy conversion ratio for impulse pressure as a function of peak radial average fuel enthalpy for the NSRR tests on waterlogged fuel and irradiated fuel.

Consequence #3: Coolability of Fuel Fragment Sediment

As a result of tests in NSRR and CABRI that failed by PCMI and dispersed some fuel particles through the rupture opening, the NSCJ evaluated the coolability of the fuel fragment sediment assuming all the dispersed material concentrated in the bottom of the reactor vessel. This event was considered by the NSCJ as unlikely because the particle size of the dispersed material indicates that some of the material would remain in suspension in the circulating coolant and any material that would be deposited as sediment would be located in various places within the reactor coolant system. In both of these situations, sufficient cooling would be available to remove the decay heat.

To assess the coolability of the fuel fragment sediment, the amount of fuel material dispersed from both PCMI and waterlogged fuel ruptures was estimated using the enthalpy distribution from hypothetical RIA events in PWR and BWR reactors. It is conservatively assumed that 1%

of the fuel rods are waterlogged at the start of the accident. The number of fuel rods exceeding the PCMI failure threshold and the waterlogged fuel rupture limit are used to estimate the amount of fuel material that is released. The amount of fuel dispersed was estimated to range between 70 and 210 kgUO_2, depending on the reactor design. Assuming a decay heat rate of 0.6% of rated power, a heat transfer analysis was performed using the Lipinski model for coolability of reactor debris beds [C-3.6]. In evaluating the coolability of debris beds (sediment), dryout of liquid within the bed reduces the heat removal capability and can lead to high temperatures that threaten the support structural. Ensuring that the heat flux within the debris bed remains below a critical value for dryout (critical heat flux) provides assurance that the sediment can remain coolable. Assuming the most conservative conditions to produce a minimum critical heat flux, it was demonstrated that the heat flux within the fragmented fuel sediment is well below the critical heat flux for the worst case configuration. The NSCJ concluded that this demonstrates that the fuel fragment sediment is sufficiently cooled by the reactor coolant and that there is not impact of the dispersed fuel on the integrity of the reactor pressure vessel.

Response to Requests for Additional Information (RAI's)
NRR Safety Evaluation Report – Project No. 689

F-1. A best estimate fit to the mechanical failure data is used to determine the critical strain energy density (CSED). This fit means that slightly less than 50 percent of the rods will fail just below the failure threshold when failure is not predicted. This is not consistent with NRC criteria that dose consequences for accidents not be underestimated. A lower bound fit of the failure data would be more appropriate to determine the RIA failure and subsequent radionuclide release and dose estimates.

Response to RAI F-1

The response to RAI F-1 is divided into three parts. First, the reasons for using a best-fit curve to the CSED database to develop the cladding integrity model are described. Second, the use of the cladding integrity model combined with conservatisms in developing the fuel rod failure threshold described in the RIA Topical Report is described. Third, the conservatisms within the radionuclide release assumptions used to calculate the dose consequences are described.

Development of Cladding Integrity Model

A best-fit rather than a lower bound curve to the critical strain energy density (CSED) data was used to develop the cladding integrity model for three principal reasons.

First, the scatter (or variation in CSED at a given oxide thickness) observed in the combined CSED database is not representative of the stochastic nature of material failure. The scatter in the mechanical property data is more related to variations in test sample geometry, loading conditions, and temperature. This is evident when each individual dataset (burst, ring, and axial tension) is evaluated separately. It can be seen that the scatter within each dataset is much less than the combined CSED database. However because of the limited amount of mechanical property tests on highly irradiated cladding material, it was not possible to eliminate selected datasets. Instead, a best-fit to the entire CSED database was used to ensure no significant upward or downward bias was introduced into the cladding integrity model.

Second, comparison of the maximum SED calculated by FALCON during the RIA simulation tests in CABRI UO_2 fuel with the best-fit CSED curve finds that all the non-failed tests reside below the best-fit CSED curve for non-spalled cladding material confirming the non-failed outcome for these tests. This result is shown in Figure F-1.1. Significantly lowering the non-spalled CSED curve to the lower bound of all the CSED data would result in prediction of failure for all the non-spalled UO_2 tests in CABRI, which would be inconsistent with the outcomes of these tests. Conversely, the failed UO_2 rods in the CABRI tests were all from test segments containing oxide spallation and the calculated SED for these tests reside above the best-fit CSED curve for spalled cladding material confirming the failed outcome for these tests.

A third consideration in developing a cladding integrity model for PCMI conditions is the fact that the loading conditions for typical mechanical property tests performed on cladding samples do not represent well the cladding failure processes arising from pellet-cladding mechanical interaction (PCMI). The differences between mechanical property tests and PCMI include the type of the applied load (pressure versus displacement), friction between the pellet and cladding,

and the active gauge length. Because of these factors, the specimen average strain to failure measured in typical cladding mechanical property tests is generally lower than for conditions of PCMI. As a result, cladding integrity models developed from mechanical property tests represent a lower bound failure boundary when applied to the PCMI loading conditions of high burnup. These differences are even more important for cladding material containing incipient defects. The differences between the loading conditions used in mechanical property tests and PCMI have been evaluated in Reference F-1.1.

Use of Cladding Integrity Model in the Development of the Fuel Rod Failure Threshold

Although as discussed above, the best-fit CSED model may in fact represent a lower bound estimate of the failure potential under PCMI conditions, in applying the CSED cladding integrity model to the development of the fuel rod failure threshold, it was recognized that some additional conservatism was required to ensure that the number of fuel rod failures would not be underestimated. Irradiation causes changes in the cladding ductility as burnup progresses. Fast neutron damage accumulation leads to an increase in material strength (irradiation hardening) and a decrease in ductility at low exposures. Material property changes caused by fast fluence saturate at low exposures and do not lead to significant decreases in cladding ductility at high burnup. A continued decrease in cladding ductility with exposure is known to occur due to outer surface corrosion and the accompanying hydrogen pickup and formation of zirconium hydrides (ZrH_2) platelets. These hydrides cause a further increase in material strength and a more significant decrease in cladding ductility, depending on the hydrogen content, distribution, and ZrH_2 platelet orientation. Because of the interrelationship between outer surface corrosion layer thickness and hydrogen content, it is convenient to use the oxide layer thickness as an indicator of hydrogen concentration.

Poolside inspections and destructive examinations find that the oxide layer thickness and hydrogen content can vary significantly as a function of fuel rod exposure. Since the cladding ductility depends on hydrogen content, the variations in oxide thickness and hydrogen content can lead to deviations in cladding ductility as well. To account for the uncertainties in the changes in cladding ductility with burnup, an upper bound cladding oxide thickness versus burnup correlation was developed from more than 4400 oxide thickness measurements on Zr-4 cladding. The data and upper bound curve are shown in Figure F-1.2. Since the cladding integrity model is a function of oxide thickness, using the upper bound oxide thickness accumulation versus burnup curve shown in Figure F-1.2 results in an upper bound estimate of the decrease in cladding ductility with burnup when combined with the cladding integrity model.

This can be seen when the upper bound oxide thickness curve is used in the CSED correlation given by Equation 2-12 in the Topical Report. This approach produces a lower bound CSED versus burnup curve for non-spalled cladding, which is shown in Figure F-1.3 along with a comparison of the FALCON calculated SED for the CABRI REP Na UO_2 tests without oxide spallation. None of these test rods failed during the experiments in CABRI. The conservative nature of the CSED versus burnup curve is evident in Figure F-1.3 where three of the experiments reside well above the curve, yet none of these rods experienced cladding failure. Three non-failed tests lie below the bounding CSED curve shown in Figure F-1.3. Since the cladding SED is a function of the fuel enthalpy, the low levels of fuel enthalpy reached in each

of these tests resulted in low mechanical duty on the cladding. As a result, a large margin to cladding failure existed in these three tests.

Calculation of Radionuclide Release Rate and Dose Consequences for a Control Rod Ejection Accident

Regulatory Guide 1.77 specifies the assumptions and the approach to be used in calculating the radionuclide release and dose consequences from the fuel rod failures during a control rod ejection accident. Several conservatisms are included in this calculation including;

- Calculate end of life core nuclide inventory assuming continuous maximum power operation throughout the lifetime (maximizes the fission product production rate)
- No allowance for radioactive decay prior to the accident initiation in calculation of the nuclide inventory (maximizes the fission product inventory)
- The activity accumulated in the fuel-cladding gap should be assumed to be 10% of the noble gases and 10% of the iodines
- 100% of the gaseous constituents in the fuel-cladding gap are released at failure

Each one of these assumptions includes a degree of conservatism in estimating the radiological source term from the fuel rod failures during a reactivity accident. Recent RIA-simulation tests on short fuel rod segments with almost uniform axial power distributions have shown transient fission gas release rates between 5% and 25%, depending on the burnup level and maximum radial average fuel enthalpy. This transient gas release is beyond that incurred during the base irradiation. Typical fission gas release inventories from the base irradiation were below 5% for the rods tested in NSRR and CABRI. In applying these transient gas release rates to LWR fuel under postulated reactivity accidents, the axial distribution of the power deposition must be considered. Neutron kinetics calculations using 3-D methods have shown that less than 30% of the fuel column is affected by the energy deposition because of the localized nature of a reactivity accident. As a result, the local power peaking limits the inventory of noble gases and iodines available for release and the assumption of 10% of the noble gases and 10% of the iodine isotopes would provide an upper bound to the fuel-cladding gap inventory for a full-length high burnup fuel rod. The assumptions above can result in about a factor 2 overestimation of the release of the noble gases and potentially much higher for the iodine release. Conservative assumptions are also used in the transport of fission products through the primary reactor coolant system to the environment. These further increase the radionuclide release rate as compared to better estimate transport models.

Summary

In summary, several conservatisms are contained within the approach used to develop the proposed fuel rod failure threshold that insures the dose consequences from this accident are not underestimated. First, the cladding integrity model developed from mechanical property test data predicts a lower mechanical energy required to fail the cladding as compared to PCMI conditions during an RIA event. Second, it is expected that fuel rods targeted for high burnup operation beyond a lead rod average burnup of 62 GWd/tU would have improved oxidation characteristics and would therefore have an oxide thickness accumulation that is bounded by the curve shown in Figure F-1.2. Third, the assumptions and analysis approach defined in the

regulations to calculate the radioactive material release rates and dose consequences for the fuel rod failures also contain significant conservatisms.

Given these factors, the failure threshold based on the best-fit CSED model combined with an upper bound oxide thickness correlation provides a bounding estimate of the fuel rod failures and thus the dose consequences expected during a hypothetical RIA event in a PWR or BWR. Undue conservatism would be introduced into the process by using a lower bound fit to the CSED data from mechanical property tests when combined with the upper bound oxide thickness correlation and the conservatisms in the release fractions and dose calculations defined in the regulations.

Finally, alternative methods to address the uncertainties in the cladding ductility data can be evaluated and then used to develop a new fuel rod failure threshold. However, construction of a new approach would also need to address the conservatisms in the bounding oxide thickness accumulation curve and in the radioactive material release rate assumptions to ensure that undue conservatisms are not introduced into the final outcome.

References:

F-1.1 Montgomery, R.O., et.al., "The Mechanical Response of Cladding with a Hydride Lens under PCMI Loading Conditions," Paper presented at the International Seminar on Pellet-Clad Interaction in Water Reactor Fuels, Aix-en-Provence, France, 9-11 March 2004

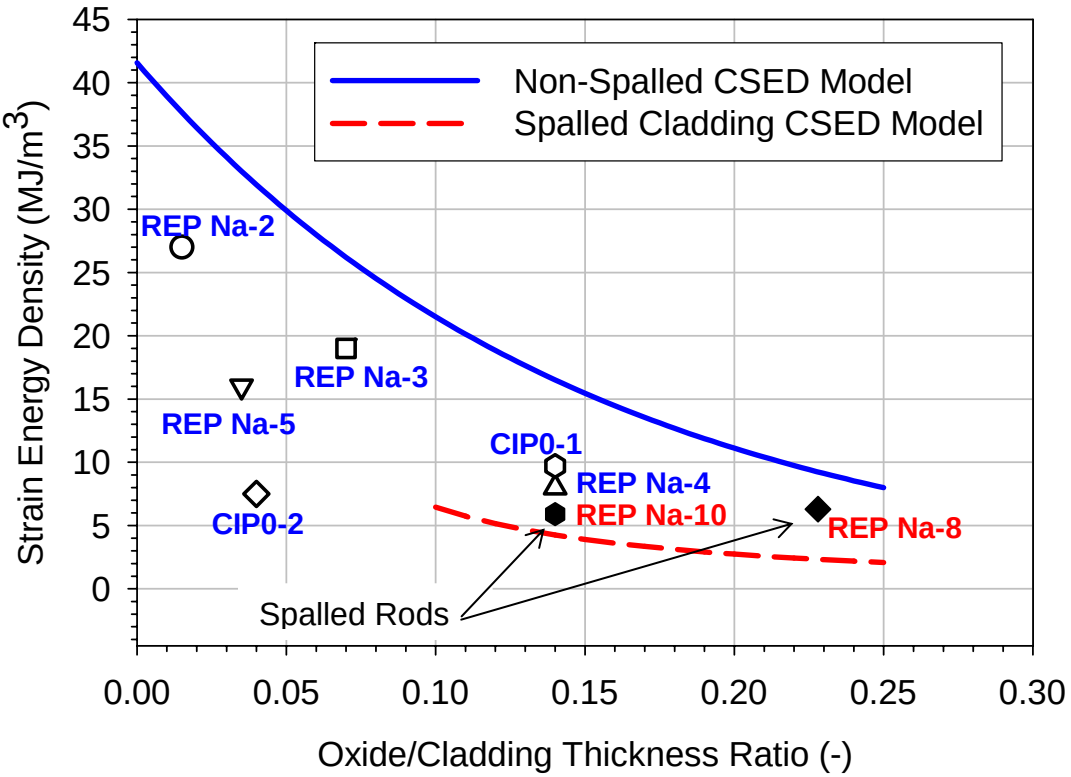

Figure F-1.1 Best-fit CSED models for non-spalled (solid) and spalled (dashed) oxide layers developed from cladding mechanical property tests. The FALCON calculated SED values for the CABRI REP Na test conducted on UO_2 fuel rods shown for comparison.

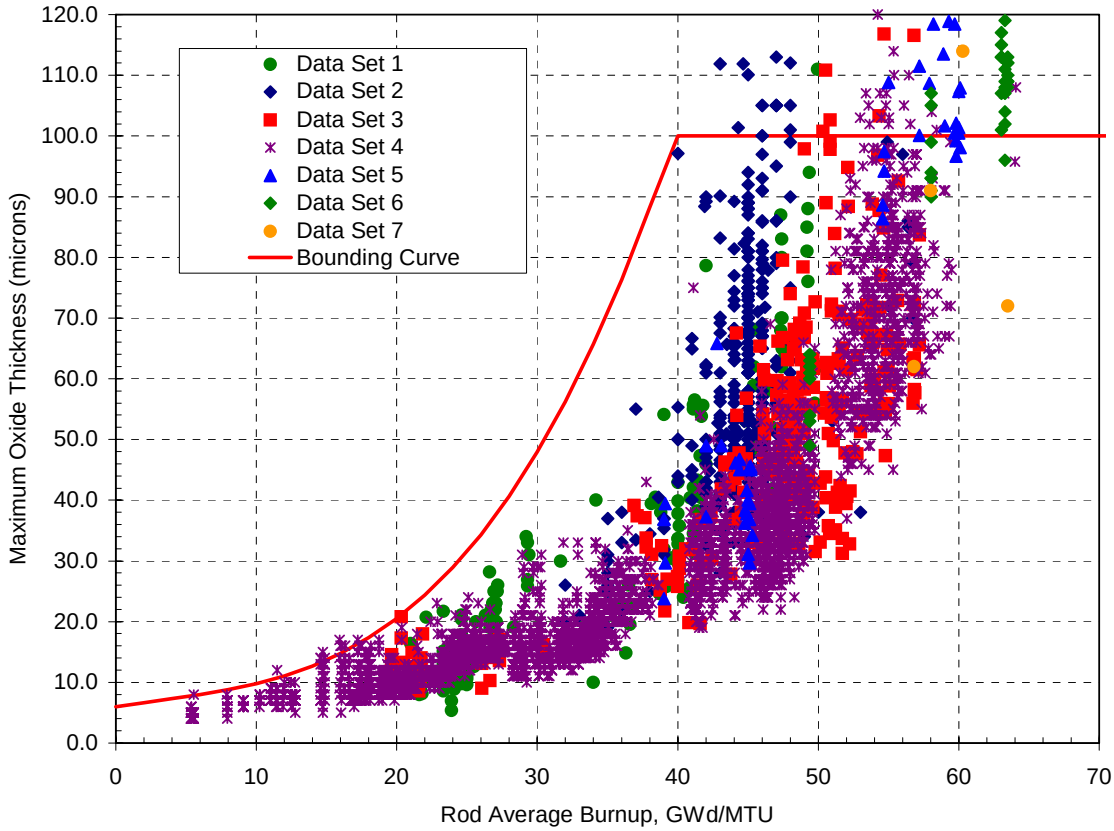

Figure F-1.2. Maximum outer surface corrosion data for Zircaloy-4 cladding as a function of rod average burnup. Upper bound curve used in the developed of the fuel rod failure threshold shown for comparison.

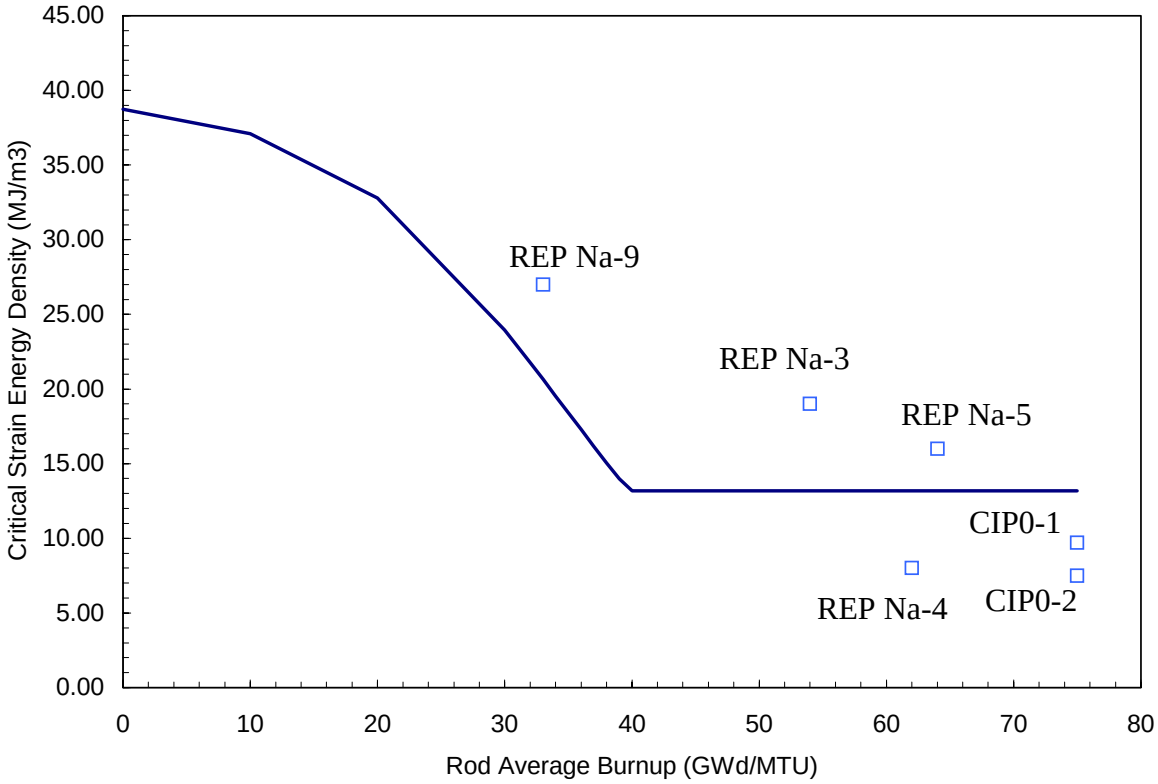

Figure F-1.3. Lower bound CSED versus rod average burnup curve used in the development of the fuel rod failure threshold. FALCON calculated SED for the non-failed UO_2 CABRI REP Na tests shown for comparison.

Response to Requests for Additional Information (RAI's)
NRR Safety Evaluation Report – Project No. 689

F-2. Clad cracking in CABRI REP Na-8 and REP Na-10 was not associated with hydride blisters or spalled locations in these tests. We believe that spalling did not cause the early failure in these tests but failure was simply a consequence of heavy oxidation that produced hydrides which degraded ductility. Eliminating these two tests results in an artificially high CSED curve.

Response to RAI F-2

Observations from both the CABRI REP Na experiments [F-2.1] and mechanical property tests on cladding material with spalled oxide layers [F-2.2, F-2.3, F-2.4, F-2.5] indicate that cladding failure in both REP Na-8 and REP Na-10 was a result of localized hydride accumulations induced by oxide spallation. Based on the pre-test neutron radiographies, post-test metallographies, and mechanical property tests performed on cladding with spalled oxide layers within the PROMETRA program [F-2.2], IRSN has concluded that the decrease in strength and ductility caused by oxide spallation and the formation of hydride lenses produced the low fuel enthalpy at failure in CABRI REP Na-8 and Na-10. In support of this position, IRSN has recently published a synopsis of the CABRI REP Na test program and issued this statement regarding cladding failure of UO_2 fuel rods [F-2.1]:

> "*On the basis of these results, the UO2 fuel rod failures* [REP Na-8 and REP Na-10] *are explained by the drastic loss of apparent ductility of the Zr4 cladding linked to the high corrosion level with hydrogen absorption into the metal and in reactor oxide spalling which lead to formation of large hydride concentrations or hydride blisters (blisters are formed by hydrogen migration towards cold points as a result of oxide removal).*"

The conclusion that the premature failure of REP Na-8 and REP Na-10 was caused by the presence of hydride lenses in the cladding is further supported by the results of tube burst tests and ring tension tests performed to measure the mechanical properties of irradiated Zr-4 cladding with outer surface oxide spallation. Tests performed within the PROMETRA [F-2.2], EPRI [F-2.3], and NFIR-III and –IV [F-2.4 and F-2.5] programs on cladding with spalled outer surface oxide layers have shown a significant decrease in both strength and ductility when large localized hydride lenses are present in the cladding. A recent report issued by NFIR contains some key observations from the mechanical property testing [F-2.5]:

> *"The presence of one or more "large" hydride lenses inevitably leads to rupture at a lower than expected pressure in burst testing. In the case of more than one hydride lens, the largest one initiates bursting…."*
>
> *"The total circumferential elongation (TCE) is well related to the local hydrogen concentration determined from half a ring sample containing the burst opening. Only samples with the same hydride configuration (e.g. hydride lenses) are directly comparable. At the same local hydrogen concentration, the sample*

without hydride lenses revealed a considerably higher TCE compared to samples with H-lenses."

The experimental evidence from the CABRI REP Na-8 and REP Na-10 tests and the observations from mechanical properties tests illustrate that localized hydride accumulations (hydride lenses) which accompany the spallation of thick outer surface oxide layers can have a significant impact on the strength and ductility of Zircaloy cladding material, and thus the fuel enthalpy to cause cladding failure. In mechanical property tests, cladding with similarly thick oxide layers without oxide spallation exhibit higher material strength and ductility as compared to cladding with hydride localization. As a result, higher fuel enthalpy levels are required to cause failure for cladding with thick non-spalled oxide layers.

Based on these observations, it is appropriate to consider the behavior of test rods containing oxide spallation within a separate population from test rods containing thick uniform oxide layers as was done in the industry approach to develop revised RIA acceptance criteria.

The following summarizes the effect of oxide spallation on the mechanical properties of Zircaloy-4 cladding and the role of oxide spallation and localized hydride accumulations on cladding failure during RIA simulation tests:

Mechanical Property Tests on Cladding with Spalled Oxide Layers

Mechanical property tests have been performed on irradiated cladding samples removed from fuel rods containing thick non-spalled outer surface oxide layers and spalled outer surface oxide layers. Both tube burst tests and ring tension tests have been used to determine the ultimate tensile strength (UTS) and total elongation (TE) of cladding under stress and strain conditions similar to that experienced during pellet-cladding mechanical interaction in an RIA event. Figure F-2.1 contains the UTS determined from tube burst tests on samples with both non-spalled and spalled oxide layers plotted as a function of the sample average hydrogen content. Similarly, Figure F-2.2 contains the plastic TE determined from ring tension tests on samples taken from cladding with non-spalled and spalled oxide layers plotted as a function of sample average hydrogen content. Further, the spalled oxide layer samples have been separated into those samples that have been confirmed to contain localized hydride lenses and those that are free of localized hydride lenses. The presence of hydride lenses was determined through either neutron radiography (tube burst tests) or metallography (tube burst and ring tension tests) examinations.

The results of both the tube burst and ring tension tests clearly demonstrate the effect of localized hydride lenses brought about by the outer surface oxide spallation on the mechanical properties of irradiated cladding. As seen in Figure F-2.1, the UTS for samples with spalled oxide layers and hydride lenses decreases by at least a factor of 2 as compared to samples with similar average hydrogen contents, but without the presence of hydride lenses. In a few samples, oxide spallation was noted, but either small or no hydride lenses were observed within the samples. These samples had UTS values similar to non-spalled tubes. The hydride lens depths in those samples that show an impact on mechanical behavior ranged between 40% and 60% of the cladding wall thickness based on both neutron radiography and post-test metallographies. Figure

F-2.3 contains metallographic images of tube burst openings from specimens removed from spalled rods. Clearly visible in these photomicrographs are the localized hydride lenses on the cladding outer surface (dark gray regions) and the underlying Zircaloy-4 ligament (light color regions). Visual examples of burst tests with and without a hydride lens are shown in Figure F-2.4.

The effect of oxide spallation and hydride lens formation on the plastic total elongation is strongly evident in the ring tension specimens. The presence of a hydride lens within the gauge section of the sample causes a reduction in the plastic TE by a factor of 4 to 5 as compared to non-spalled ring specimens or spalled specimens without a hydride lens. Several ring samples were extracted from fuel rods that contained thick oxide layers with spallation, but the ring samples did not contain a hydride lens within the sample. This is possible because the height of the ring specimens is approximately 5 mm (0.2 in) and therefore, the sample represents a very local measurement of the cladding mechanical behavior. These specimens exhibit a much higher plastic TE than those with hydride lenses within the sample, again highlighting the importance of non-uniform hydride distributions. Post-test visual appearance of ring tension specimens with and without a hydride lens is shown in Figure F-2.5. It should be noted that these samples were extracted from the same commercial fuel rod used for the CABRI REP Na-1 experiment. Extensive outer surface oxide spallation was observed for this rod in the region (Span 6) that the ring specimens were removed for testing.

Recently, Glendening, et.al. has published the results of mechanical property tests using unirradiated Zircaly-4 material containing artificially formed hydride lenses and hydride rims [F-2.6]. Comparing the normalized fracture strain from hydride lens material and hydride rim material, Glendening, et.al., concluded that Zircaloy-4 ductility was more sensitive to hydride rim depth as compared to a hydride lens depth. Figure F-2.6 contains a comparison of the normalized strain to failure as a function of hydride lens or hydride rim depth as prepared by Glendening, et.al. These results have been used by Ralph Meyer to conclude that spallation and the formation of hydride lenses during reactor operation are not as damaging to cladding ductility as the normal uptake of hydrogen and the natural consequence of hydride rim formation during in-reactor cladding corrosion.

The results of the Penn State University (PSU) tests appear to be in direct contradiction to the mechanical property tests performed on irradiated cladding which show a significant impact of hydride lenses on the ductility of Zircaloy-4 material. The following discussion points to possible reasons why this contradiction could develop.

We should first be reminded that a test specimen containing a hydride lens or a hydride rim is a multi-material structure consisting of a brittle layer (rim) or a brittle inclusion (lens) superimposed on a substrate material that contains a complex hydride structure within a Zircaloy matrix. The mechanical response of this multi-material structure is described by two main effects. The first is a geometric effect, in which the geometry of the localized hydride accumulations, i.e. the hydride lens or hydride rim, influences the stress state within the substrate material. The second is a physico-chemical effect, in which the hydride structure that forms within the substrate material defines the material response (ductility or notch sensitivity) to the stress state locally modified by the geometric effect. Thus, the overall ductility of material

containing a hydride lens or a hydride rim is governed by the mechanical response of the hydride structure in the substrate and how such a hydride structure evolves in the material.

The design and conduct of the PSU tests are focused primarily on the geometric effects (stress state) between the two different localized hydride accumulations (hydride lens versus hydride rim). As a result, these tests are predominately measuring the ductility of the substrate material in response to the different stress states imposed by the hydride lens or hydride rim geometries. Therefore, it is important to know if the sample preparation techniques used to form the hydride lens or hydride rim produces method-independent hydrogen concentrations and hydride platelet morphologies within the substrate material before a comparison can by made between these two localized hydride geometries. Since two different procedures were used to form the hydride lens and hydride rim material, the most likely cause of the different ductility behaviors exhibited by these materials is that the hydrogen content and hydride platelet morphology within the substrate material are different; and if they are different, are these differences intrinsic, i.e. independent of the specimen preparation method, or merely an artifact of the specimen preparation procedure. Additional information is needed before any conclusions based on the PSU tests can be made about the impact of hydride lenses or hydride rims on material ductility, or extrapolation to general material behavior. The needed information should be such that, (a) it can characterize the hydride structure within the substrate material for the two different sample preparation techniques; and (b) it can show that the substrate hydride structure in the two tests are not an artifact of the specimen preparation methods. Thus, based on the reported information, it is not possible at this time to attribute the differences in ductility shown in Figure F-2.6 to a generic behavior of the hydride lens geometry or the hydride rim geometry.

Because the characteristics of the substrate material are an important factor in the ductility of cladding containing a hydride lens or hydride rim, a method is needed to determine the applicability of the PSU test results to the behavior of actual in-reactor cladding. This would require developing a method to confirm that the hydride structure within the substrate material produced in the laboratory is representative of irradiated cladding. Such an approach is needed before any comparison of the laboratory results can be made to in-reactor material. To this end, it is important to point out that the evolution of hydrides in the Zircaloy matrix occurs at the expense of causing internal stresses in the metal-hydride continuum because of the volume increase of the zirconium hydrides. In-reactor, these internal stresses evolve very slowly and are easily accommodated without geometric distortion under the combined effect of thermal and irradiation-induced stress relaxation. Such accommodation of the zirconium hydride volume does not occur in laboratory experiments, and if the internal stresses remain in the specimen they would adversely impact the outcome of any mechanical property tests, unless the specimens are heat-treated at the appropriate temperature-time regime to induce complete stress relaxation. However, such heat treatments could not be performed without causing hydrogen re-distribution and changes in hydride morphology, both in the rim/lens regions as well as, the substrate, thereby inducing fabrication method dependent behavioral differences between the rim and the hydride lens, not to mention the further deviation from prototypical irradiated cladding conditions.

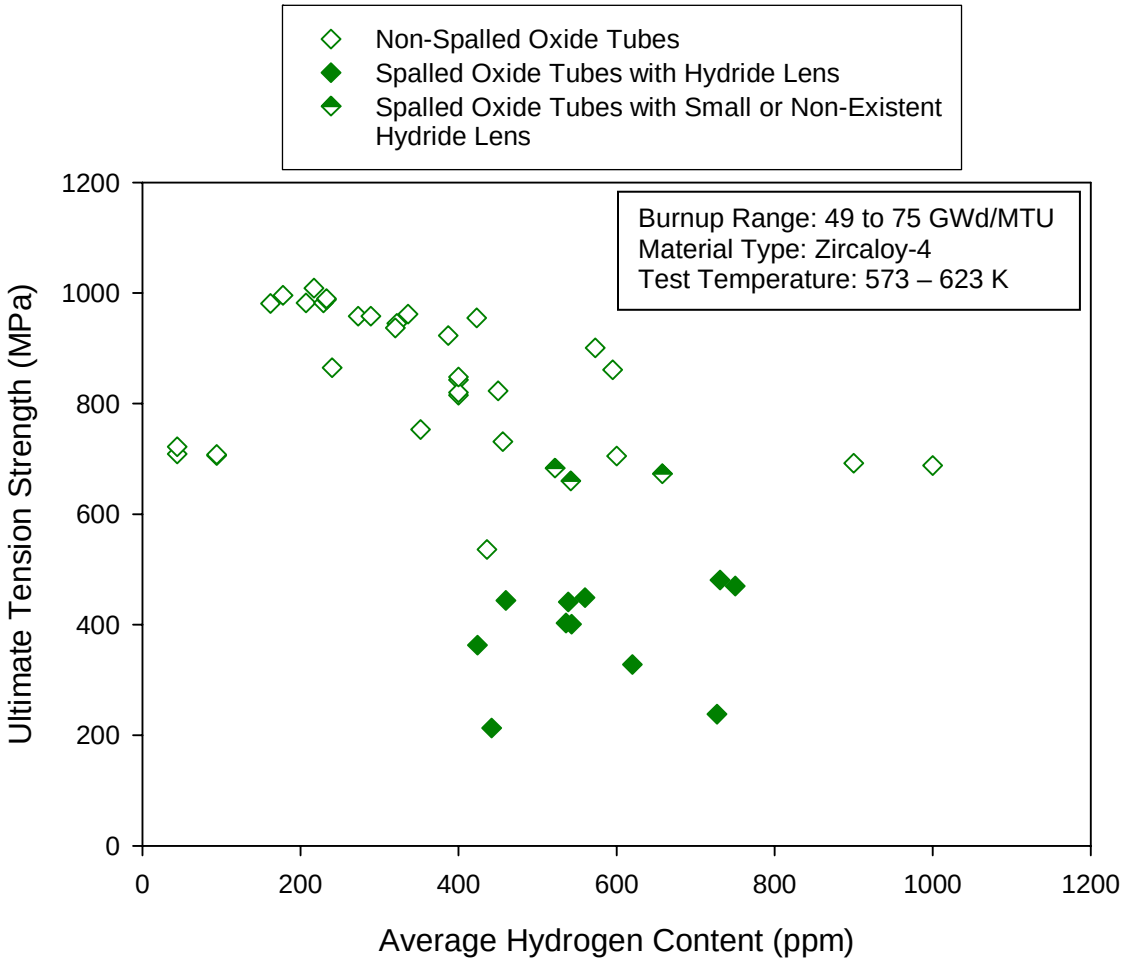

Figure F-2.1. Ultimate tensile strength from tube burst tests on cladding with both non-spalled and spalled oxide layers as a function of sample hydrogen content.

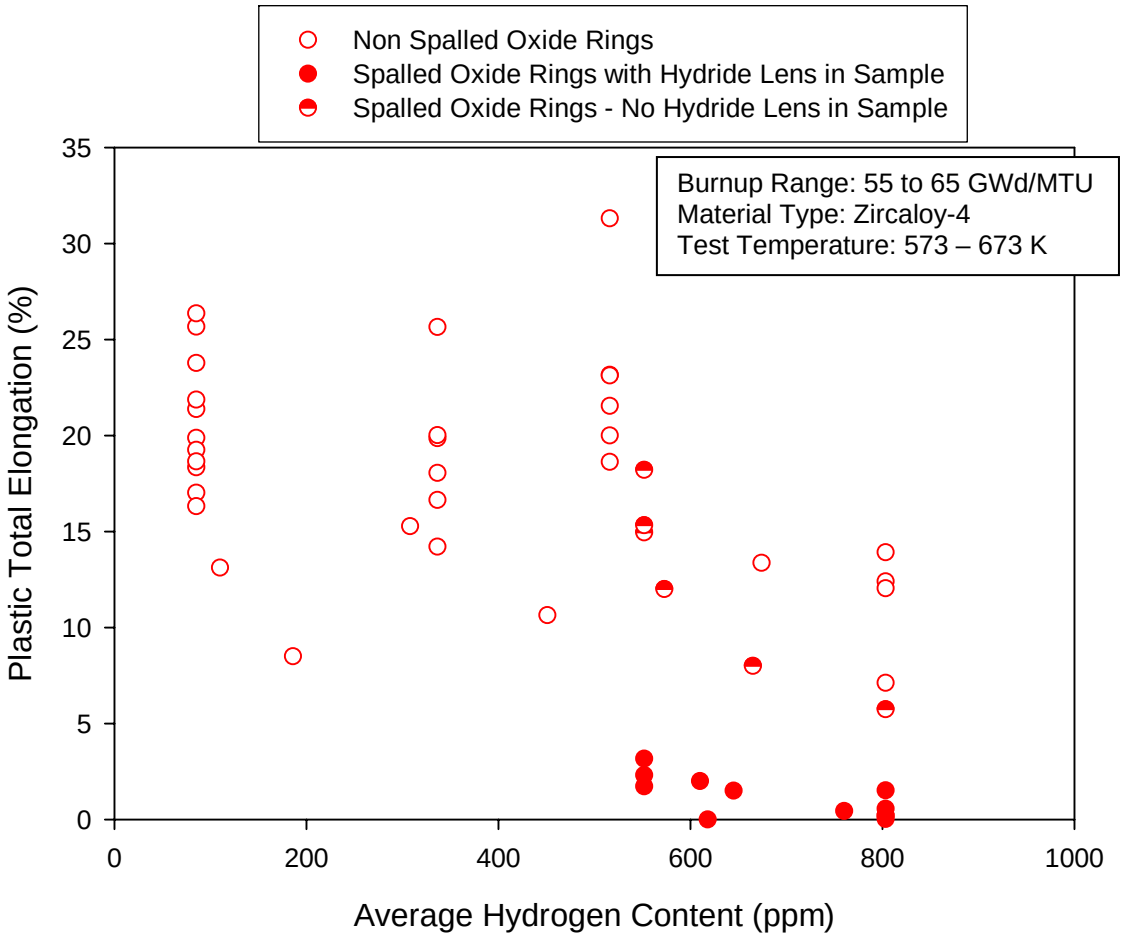

Figure F-2.2. Plastic total elongation from ring tension tests on specimens with both non-spalled and spalled oxide layers as a function of sample average hydrogen content.

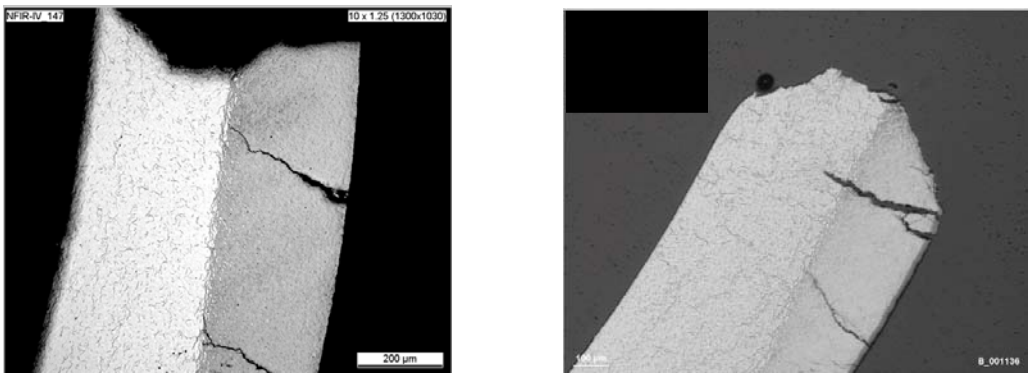

Figure F-2.3. Examples of photomicrographs of tube burst test specimens from cladding with spalled oxide layers and localized hydride lenses.

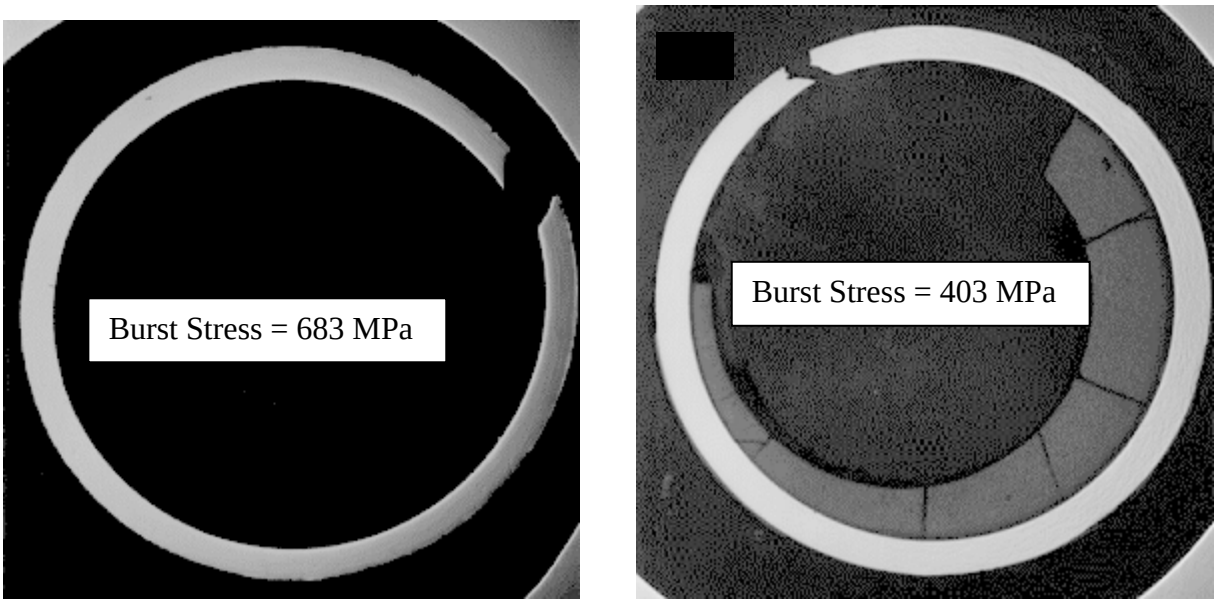

(a) (b)

Figure F-2.4. Comparison of metallographic images from (a) tube burst test without the presence of localized hydride lenses and (b) with localized hydride lenses

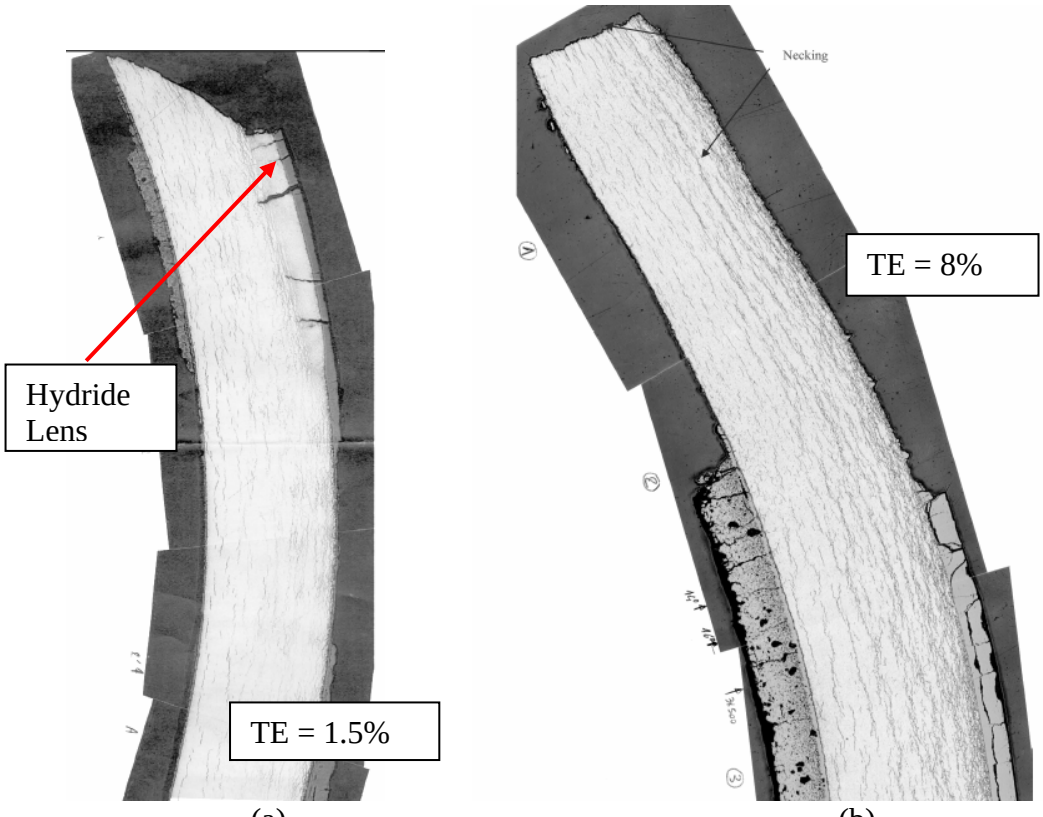

(a) (b)

Figure F-2.5 Metallographic images of the ring tension specimens with and without a hydride lens within the gauge section. Both samples were extracted from cladding with spalled oxide layers.

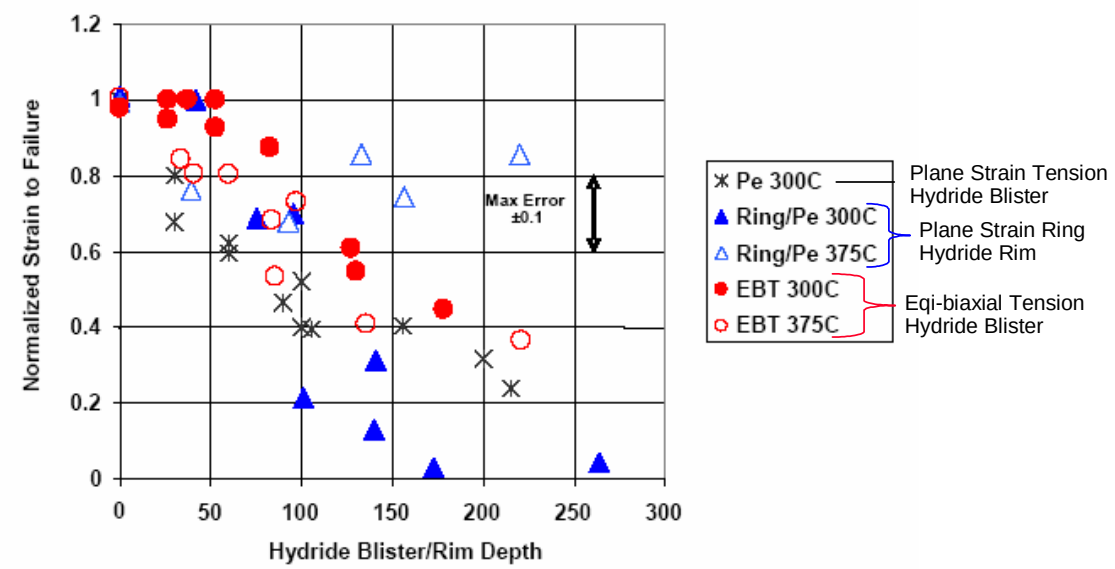

Figure F-2.6 Normalized strain to failure as a function of hydride lens or hydride blister depth (in microns) from plane strain (Pe) ring or plate samples and equibiaxial tension (EBT) plate samples.

Observations from the CABRI REP Na-8 and Na-10 Tests

Both CABRI REP Na-8 and REP Na-10 experienced cladding failure during the energy deposition phase of the tests at radial average fuel enthalpy levels around 80 cal/gm. It is necessary to identify the time and location of the initiation point for cladding failure to fully understand the mechanisms leading to through-wall crack formation in these rods. In the CABRI test facility, on-line instrumentation is used to detect the cladding failure event and to estimate the axial location on the rod where cladding failure was initiated. The instrumentation has been somewhat reliable in detecting the time of cladding failure, but still requires some interpretation of the microphone, flowmeter, and pressure transducer signals to provide confidence in the time of cladding failure. However, using on-line instrumentation to pinpoint the location on the rod where failure initiation occurred has proved to be somewhat unreliable. During the REP Na-1 Task Force review of the on-line instrumentation capabilities, it was determined that uncertainties in the evaluation of the microphone signals can lead to variations in the axial position by more than 10 cm [F-2.7].

As a result of these difficulties, the burden of identifying the location for cladding failure initiation has fallen on post-test visual and destructive examinations. Unfortunately, this has further been complicated by the fact that geometry changes have occurred in these rods during storage in the hotcell after the experiments were completed. Therefore, the identification of the mechanisms leading to cladding failure has required combining our understanding of the pre-test rod conditions with a limited amount of post-test destructive examination data, our experience from mechanical property tests, and analytical evaluations.

The maximum outer surface oxide thickness for REP Na-8 and REP Na-10 was estimated to be ~120 microns and ~80 microns, respectively. Profilometry and eddy current traces of the outer

surface oxide thickness showed evidence of oxide spallation in both rods. The oxide layer spallation in the fuel segment used for REP Na-8 was localized to a narrow region azimuthally oriented around the fuel rod. REP Na-10 also displayed a significant amount of oxide thickness spallation over the upper two-thirds of the segment used in the experiment. Pre-test neutron radiographies were performed and maps of the numerous localized hydride lenses were developed for both fuel segments.

Post-test visual examinations were performed on REP Na-8 approximately 4 months after the test and a second time ~11 months after the test. Multiple cladding cracks were found on the test rod during both visual exams. These observations revealed that the cladding cracks were widening and possibly extending while in post-test storage within the hot-cell. Similarly, three post-test visual examinations were performed on REP Na-10, ~4.5 months after the test, ~11 months after the test, and finally, ~31 months after the test. A single crack is observed in the cladding and this crack was noted to have grown from ~7 cm long in the first visual exam to ~22 cm long in the last visual exam. This widening and extension of the cladding cracks after the test is a consequence of sodium-UO_2 interaction leading to pellet swelling. The fact that the cladding cracks are extending during storage complicates the post-test examination process and the assessment of the location and processes leading to crack initiation.

Figure F-2.7 is a diagram containing a map of the axial and azimuthal locations of the cladding cracks found in REP Na-8. Also shown are the locations of metallographic samples cut from the test rod and a box highlighting the region of the most obvious oxide spallation. A diagram is also provided showing the axial and azimuthal locations of the localized hydride lenses observed in the pre-test neutron radiography exams. It can be seen that a cluster of localized hydride lenses is located between 300 mm to 420 mm above the bottom of the fuel column. Isolated hydride lenses are also located below this region. Based on the mechanical property tests on material containing hydride lenses, these hydride lenses in the cladding can act as incipient defects in the cladding, weakening the cladding and making it more susceptible to through-wall cracking after a load is applied.

Three main cracks are observed in Figure F-2.7, one located between 130 mm to 280 mm from the bottom of the fuel column, a second crack located between 300 and 330 mm from the bottom of the fuel column, and a third crack located between 390 and 550 mm from the bottom of the fuel column. Comparing to the neutron radiography, the axial position of the lowest crack coincides with one small hydride lens near 260 mm from the bottom of the fuel column and the middle crack coincides with a large hydride lens at ~315 mm from the bottom of the fuel column. The upper crack also coincides with several hydride lenses between 400 and 430 mm from the bottom of the fuel column. It should be noted that identification of the presence of hydride lenses by neutron radiography is subject to some uncertainty and it is possible that smaller hydride lenses were not identified in the pre-test examinations.

The key to understanding the cladding failure during an RIA event is to identify the mechanisms within the cladding that cause through-wall crack initiation during the energy deposition. This means that post-test examinations must focus on the locations in the cladding at which crack initiation occurred during the tests. Regions of the cracks that extended axially during the test or following the test during cooldown or in storage in the hot-cell are of considerably less interest.

No metallography was performed on the lower crack and therefore it is not possible to determine the crack initiation process for this crack. The presence of a hydride lens within the axial extent of the lower crack suggests that crack initiation could have occurred at that location because of the reduced strength and ductility caused by a hydride lens. The crack then extended axially under additional PCMI loading during the energy deposition or during storage within the hotcell. However, without metallographic examinations to confirm this point, it is not possible to be certain of the crack initiation process. The metallographic examinations in the vicinity of the middle crack located between 300 mm and 330 mm from the bottom of the fuel column shows a hydride lens coincident with the through-wall cladding crack, as shown in Figure F-2.8. The visual appearance of the crack is consistent with brittle fracture of the hydride lens normal to the azimuthal plane and then radial propagation of the crack through the remaining Zircaloy ligament at ~45° from the azimuthal plane. Many similarities can be noted between the metallographic image shown in Figure F-2.8 and the mechanical property test on a sample with a hydride lens shown in Figure F-2.5(a). These visual examinations strongly indicate that crack initiation occurred at a localized hydride lens. Several metallographic examinations were performed along the length of the upper crack. All of these examinations appear to coincide with regions of the crack that extended axially during the energy deposition, during cooldown, or storage in the hot-cell. The crack initiation site (or sites) was not identified during the metallographic exams. Again, the presence of hydride lenses in the vicinity of the upper crack suggests that crack initiation could have occurred at these locations. However, without additional metallographic data it is not possible to ascertain with any certainty the crack initiation process for the upper crack.

A plot of the crack opening strain for REP Na-10 as a function of axial position is shown in Figure F-2.9 based on the three post-test visual examinations performed ~4.5 months, ~11 months, and ~31 months after the test in CABRI. The post-test axial extension of the cladding crack from ~7 cm to 22 cm is clearly evident in the figure. IRSN used a linear extrapolation of the crack length as a function of time after the test to estimate an initial crack length of ~ 3 mm at completion of the test. This initial crack length is shown in Figure F-2.9 at an axial position corresponding to the maximum opening strain after the first visual examination. There are two issues with the IRSN approach to estimate the length and axial position of the initial cladding crack that must be considered. First, the growth rate of the initial crack may not have been constant with time during the first 4.5 months after the test. A much faster crack growth rate initially would result in a smaller initial crack. Second, the axial position cannot be estimated with this approach and it is only an assumption that the initial crack would correspond to the position shown in Figure F-2.9.

A map of the localized hydride lenses identified from the neutron radiography is shown above the plot of the crack opening strain. A number of different sized hydride localizations were found between 150 mm to 400 mm above the bottom of the fuel column. From this diagram, it appears that the cladding crack in REP Na-10 initiated during the power pulse in the vicinity of a hydride lens as a short crack less than 3 mm long which consequently extended axially during storage in the hot-cell.

The post-test destructive examinations performed on REP Na-10 were limited to a single metallographic examination. The axial position of the metallographic exam performed on REP

Na-10 is also indicated in Figure F-2.9. A picture of the cladding metallography is shown in Figure F-2.10. The main features observed in Figure F-2.10 are a through-wall crack with a brittle appearance (i.e. crack faces normal to the azimuthal direction) and several part-wall cracks in hydride blisters that are ~30% of the cladding thickness. Figure F-2.11 contains a detailed view of the cladding in the vicinity of the through-wall crack after etching of the sample to view the zirconium hydride platelets. One important feature that can be observed in Figure F-2.11 is the numerous radial hydrides throughout the cladding in the vicinity of the crack. These radial hydrides were not present in the cladding prior to the test. Typically, radial hydrides form in Zircaloy-4 cladding when a tensile hoop stress exists upon cooling. Such is the case immediately following the power pulse experiment in the CABRI test. The presence of these radial hydrides indicates that the through-wall crack observed in Figure F-2.10 most likely occurred shortly after the experiment as a result of axial crack propagation assisted by the radial hydrides. IRSN has drawn similar conclusions [F-2.7, F-2.8]. Based on this information, the actual cladding crack initiation site is located elsewhere on the rod. The existence of several hydride lenses in the likely vicinity of the initial crack location, which is also near the peak power location, strongly suggests that the initial cladding crack formed as a result of fracture of a hydride lens and further propagation radially and axially under tensile hoop stresses. As discussed above, the presence of hydride lenses can have a significant effect on both the ultimate tensile strength and total elongation of the cladding.

In summary, pre-test neutron radiography combined with post-test examinations of CABRI REP Na-8 and REP Na-10 show that cladding failure initiation occurred in cladding regions containing localized hydrides (hydride lenses) resulting from outer surface oxide layer spallation. Metallographic data for REP Na-8 finds a clear example of crack initiation within a hydride lens and then radial propagation through the remaining cladding ligament. Because of the limited amount of destructive examinations performed on both REP Na-8 and REP Na-10, it is not possible to determine the crack initiation processes for all the cracks observed in these tests. However, the presence of numerous localized hydride lenses in the cladding for both test rods strongly suggests the fuel enthalpy required to cause cladding failure in these tests was influenced by the oxide layer spallation and resulting redistribution of hydrogen in to localized lenses. Mechanical property tests on cladding with localized hydride lenses supports this assessment.

Fuel Rod Failure Threshold Development

The industry recognizes the adverse impact oxide spallation can have on mechanical performance and has made a commitment to move away from operating with fuel rods containing large amounts of oxide spallation and hydride lenses. This is evidenced by the development of newer cladding alloys with improved outer surface corrosion capabilities. As a result, it is logical to consider that cladding failure of fuel rods with uniform oxide layers should be treated separately from fuel rods with spalled oxide layers. This is the main reason that the spalled rods have been excluded in the development of the fuel rod failure threshold included in the Topical Report. However, it is possible to develop a separate fuel rod failure threshold for use in situations where fuel rods are operated in a condition of significant oxide spallation. Such a threshold would include the impact of oxide spallation on the ability of the cladding to withstand the PCMI forces generated during an RIA event. By providing two separate fuel rod

failure thresholds, it is therefore possible to account for the presence of oxide spallation, if needed, without unfairly penalizing those plants/fuel designs that operate with good cladding corrosion performance. The responsibility of justifying which threshold applies would then fall on the fuel suppliers or licensees.

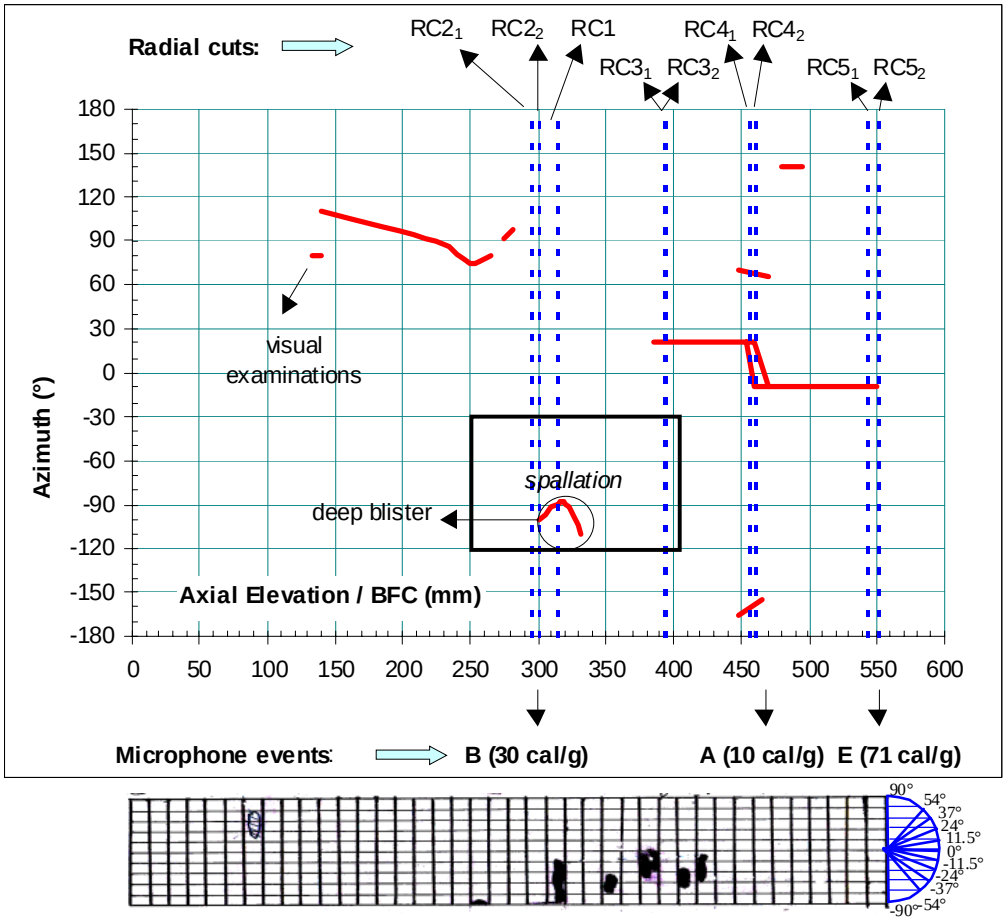

Figure F-2.7: Diagram of the locations of the axial cracks in CABRI REP Na-8 observed in post-test examinations. Map of localized hydride lenses observed in pre-test neutron radiography is shown at the bottom of the diagram.

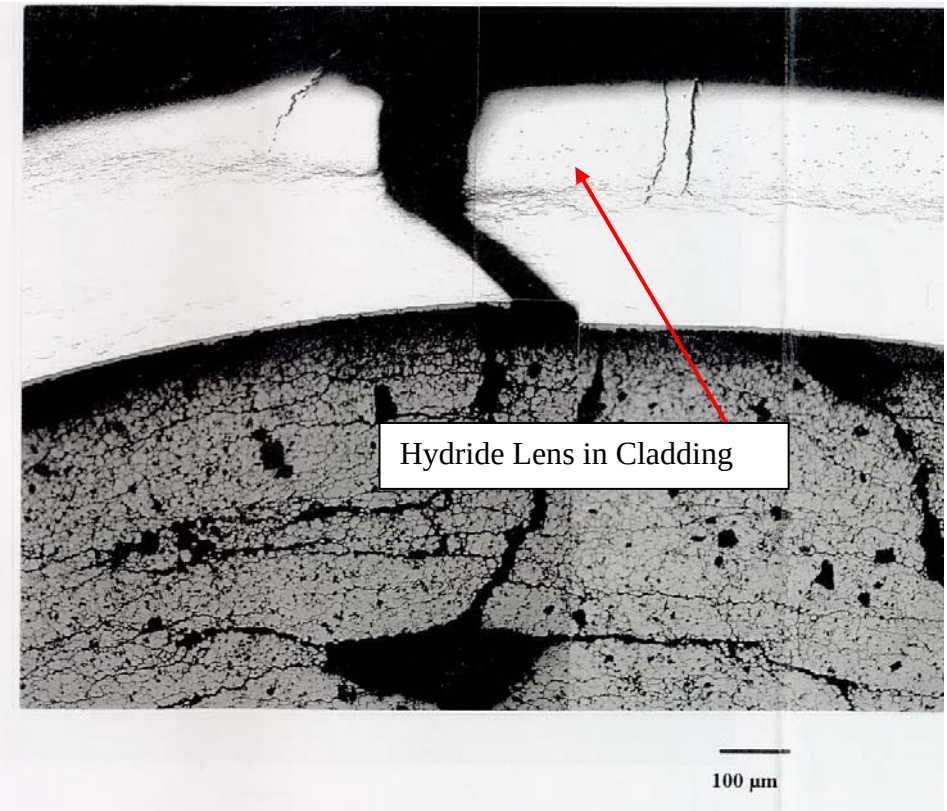

Figure F-2.8: Metallography showing hydride lens and cladding crack at 320 mm from the bottom of the fuel stack.

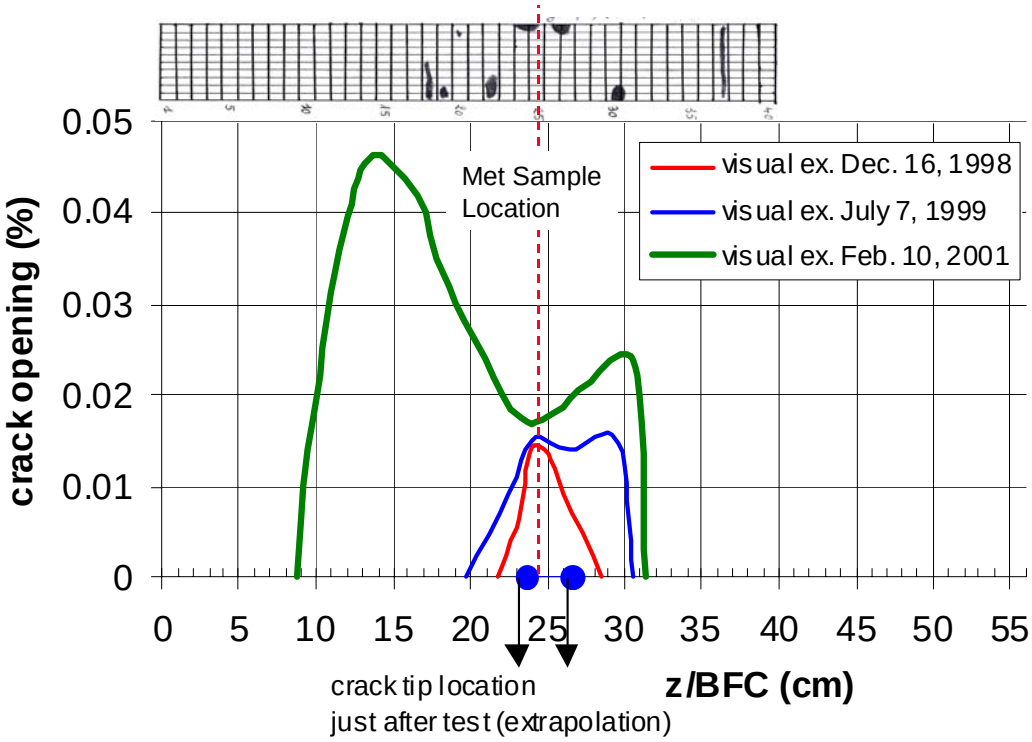

Figure F-2.9: Plot of crack opening strain as a function axial position above the bottom of the fuel column as observed during each of the visual examinations of REP Na-10. A map of the localized hydride lenses observed in pre-test neutron radiography is shown at the top of the diagram.

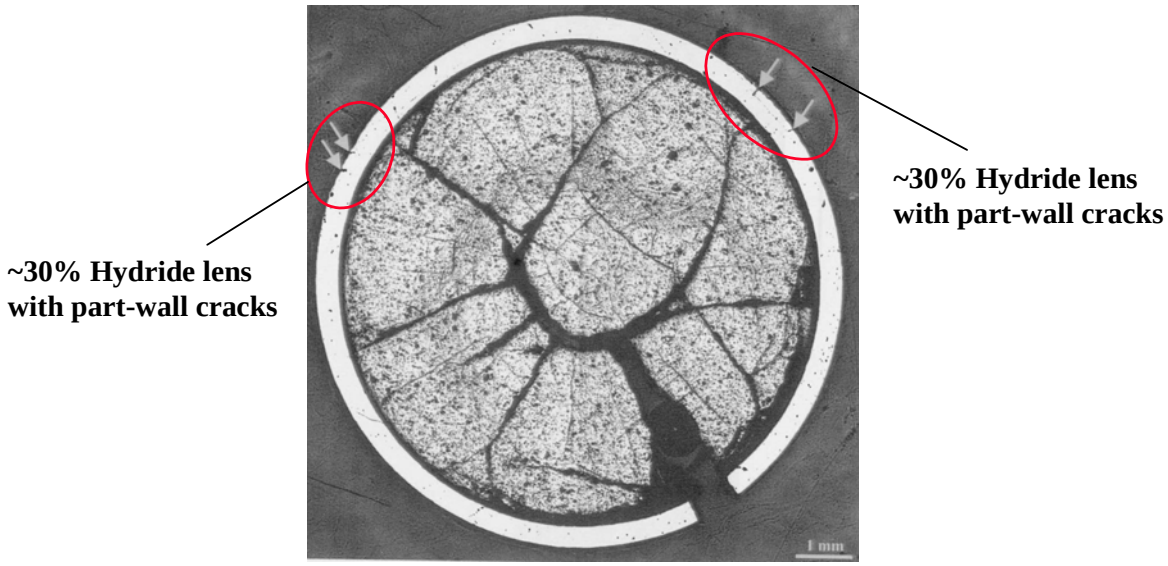

Figure F-2.10: Optical metallography sample from CABRI REP Na-10 at 244 mm above the bottom of the fuel column. Through-wall radial crack is observed near bottom of the picture. Part-wall cladding cracks were noted within two hydride lenses.

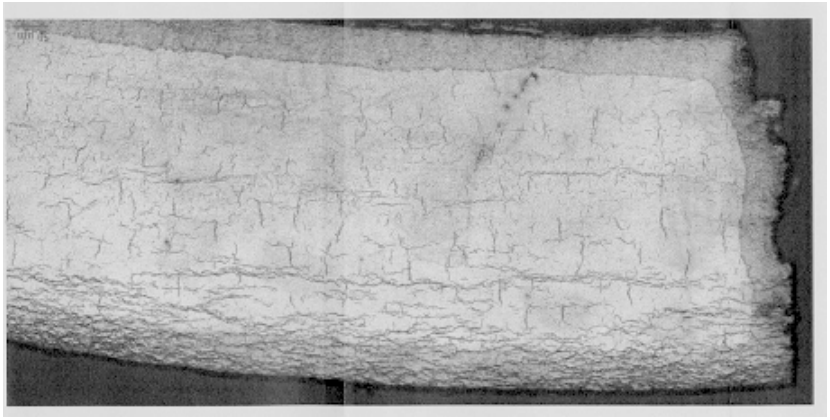

(a)

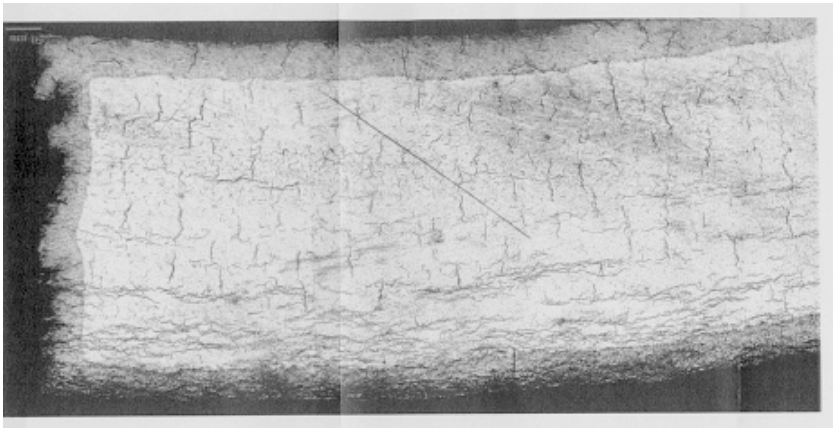

(b)

Figure F-2.11: Closeup view of etched cladding metallography near through-wall crack in Figure F-2.10. Note numerous radial hydrides in the cladding on both sides of the crack.

References:

F-2.1 J. Papin, B. Cazalis, J.M. Frizonnet, E. Fédérici, F. Lemoine, "Synthesis of CABRI-RIA Tests Interpretation," *Eurosafe Forum 2003*, Paris, November 2003.

F-2.2 Desquines, J., et. al., "Mechanical Properties of Zircaloy-4 PWR Fuel Cladding with Burnup 54-64 MWd/kgU and Implications for RIA Behavior," Journal of ASTM International, *Vol. 2, No. 6, June 2005.*

F-2.3 Smith, G., Pirek, R., and Griffiths, M., "Hot Cell Examination of Extended Burnup Fuel from Calvert Cliffs-1: Volume 2," EPRI TR-103302-V2, July 1994.

F-2.4 Hermann, A., Poerschke, P., and Martin, M., "Fuel Cladding Integrity at High Burnup: Part 1: Hydraulic Burst Tests and Tensile Tests on Large Samples, Revision 1 of TR-108753-P1," EPRI, Palo Alto, CA, Nuclear Fuel Industry Research (NFIR) III Group: 2000. 1000605.

F-2.5 Hermann, A., et. al., “Effect of Localized Hydride Accumulations on Zircaloy Cladding Mechanical Properties, EPRI, Palo Alto, CA: 2004. 1003401.

F-2.6 .Glendening, A., Koss, D. A., Motta, A. T., Pierron, O. N., and Daum, R. S., “Failure of Hydrided Zircaloy-4 Under Equal-Biaxial and Plane-Strain Tensile Deformation,” *Journal of ASTM International, June 2005, Vol. 2, No. 6.*

F-2.7 Rosenbaum, H., *Resolving our Understanding of REP-Na1: Volume 1: Microstructural Analysis*, EPRI, Palo Alto, CA: 2004. 1010958.

F-2.8 Desquines, J., Communication to REP Na-1 Task Force, “Discussion on REP Na-10 Test,” March 2003.

Response to Requests for Additional Information (RAI's)
NRR Safety Evaluation Report – Project No. 689

F-3. The single mixed-oxide (MOX) fuel failure in the French Test Reactor (CABRI) series was assumed to be different from the uranium dioxide (UO_2) failures because of inhomogeneities and a gas expansion model was invoked for only this test. We are not convinced that gas expansion can significantly enhance the cladding stress as postulated. Thermal expansion of MOX and UO_2 are almost identical, so the loading from expansion should not depend on homogeneity.

Response to RAI F-3

Experimental data from both the CABRI and NSRR RIA tests show that irradiated MOX fuel behavior is different than irradiated UO_2 fuel under RIA conditions at similar burnup and fuel enthalpy levels [F-3.1, F-3.2]. Post-test ceramography examinations and measurements of cladding permanent hoop strain and fission gas release reported in the literature finds that MOX fuel experiences stronger pellet-cladding mechanical interaction (PCMI) and higher fission gas release during rapid energy deposition events as compared to UO_2 fuel. These post-test observations are supported by in-pile measurements of dynamic fuel rod volume changes during the CABRI experiments.

Table F-3.1 contains the measured maximum residual cladding hoop strain and the transient fission gas release for several rods tested in the CABRI reactor. As can be seen, the MOX test rods experienced about two times the cladding hoop strain and fission gas release as compared to the UO_2 test rods with similar burnup levels and maximum fuel enthalpy. The residual cladding hoop strain for the UO_2 test REP Na-3 is shown in Table F-3.1 with a range of values due to uncertainties in estimating the residual hoop strain from the pre-test rod and post-test diameter measurements. The uncertainty arises from the treatment of the outer cladding surface oxide layer thickness in the calculation of the residual strain.

Table F-3.1 Comparison of UO_2 and MOX Rods in CABRI REP Na Tests

Test Rod # and Burnup (GWd/MTU)	Maximum Fuel Enthalpy (cal/gm)	Max. Residual Hoop Strain (%)	Fission Gas Release (%)	Fuel Type
REP Na-2 (33)	199	3.5	5.5	UO_2
REP Na-9 (28)	197	7.2	33.4	MOX
REP Na-3 (52)	124	1.3 - 2.2*	13.7	UO_2
REP Na-6 (47)	133	2.6	21.0	MOX
REP Na-5 (64)	108	1.1	15.1	UO_2

* - Uncertainty in the estimation of the cladding strain for this test

Figure F-3.1 contains ceramography images from the UO_2 tests REP Na-2 and REP Na-3 and the MOX tests REP Na-6 and REP Na-9. It should be noted that some grain pullout has occurred in the preparation of the REP Na-2 ceramography sample. Further some fuel pieces have also been removed during the preparation of the MOX samples. These visual appearances are artifacts of the sample preparation process and do not reflect the actual behavior of the fuel pellet.

The appearance of the irradiated MOX fuel rods is significantly different than UO_2 rods. The MOX fuel exhibits a higher density of radial cracks near the pellet periphery and circumferential cracks at the mid-pellet radius location. The presences of these fine cracks are an indication of the high level of PCMI experienced in these rods. These images further show that large swelling has occurred in the MOX fuel pellets and there is almost no increase in the free volume due to cladding strains above 3%. In comparison, the pellet-cladding gap in the UO_2 test rod REP Na-2 is clearly evident and post-test measurements finds that the pellet-cladding gap has increased from ~15 microns to ~50 microns. The change in pellet-cladding gap thickness for REP Na-2 is representative of the amount of pellet thermal expansion experienced during the power pulse.

Another indication of the enhanced PCMI due to pellet swelling in the MOX rods comes from the dynamic rod volume changes measured in the CABRI reactor. Table F-3.2 provides the estimated sodium volume displaced from the flow channel in UO_2 and MOX rods tested in CABRI at an injected energy of 70 cal/gm. The amount of sodium displaced from the flow channel is determined by integrating the difference between the channel outlet and inlet flowmeter measurements. Sodium volume displacement from the flow channel is caused mostly by the radial and axial expansion of the test rod during the early energy deposition phase of the RIA tests in CABRI. As a result, early time measurements of the displaced sodium volume represent the fuel rod volume change due to PCMI. In the later portion of the transient, heat conduction causes dilation of the sodium, leading to a further increase in displaced sodium volume. Because different fuel column lengths were used in the CABRI tests, the displaced sodium volume results shown in Table F-3.2 have been normalized to an active fuel column length of ~560 mm.

The measured values shown in Table F-3.2 demonstrate that the fuel rod volume increases at a faster rate in the MOX rods as compared to the UO_2 rods during the energy deposition phase of the experiments. The effect of MOX on the fuel rod expansion process is shown clearly in Figure F-3.2 which contains a plot of the displaced sodium volume at an injected energy of 70 cal/gm as a function of test rod burnup. The comparison of the displaced sodium volume was selected at a fuel enthalpy of 70 cal/gm because the fuel rod volume change is caused primarily by PCMI during the early phase of the energy deposition. Later in the power pulse, sodium dilation from heat conduction from the fuel rod further increases the displaced sodium volume beyond that caused by PCMI. For the UO_2 rods, the displaced sodium volume results shown in Table F-3.2 and Figure F-3.2 reflect the amount of fuel rod volume change caused by thermal expansion of the UO_2 pellet. This has been confirmed by analysis. Such is not the case for the MOX rods, where the increase in fuel rod volume is much higher than expected based only on pellet thermal expansion. From the linear trend of the data shown in Figure F-3.2, the effect of burnup on the fuel rod expansion rate is about 2 times higher in MOX fuel than a UO_2 fuel. An example of this difference is shown in Figure F-3.3 which compares the measured displaced sodium volume for two UO_2 test rods, REP Na-3 and REP Na-5 with the results from the MOX

REP Na-7 test as a function of injected energy. Also shown for comparison are the FALCON analysis results for REP Na-7 assuming that UO_2 thermal expansion is the only contribution to PCMI. These results highlight the faster rate of fuel rod volume increase in the MOX test REP Na-7 as compared to the UO_2 tests with similar burnup levels. The FALCON analysis results also confirm that unlike the fuel rod volume increase in the UO_2 rods, which is caused by pellet thermal expansion, REP Na-7 has a fuel rod volume increase that is much higher than that expected from simply pellet thermal expansion. Enhanced swelling of the pellet by the fission gas located on grain boundaries is the most likely explanation for the behavior of the MOX rods.

Table F-3.2 Displaced Sodium Volume for UO_2 and MOX Rods in CABRI REP Na Tests at an Injected Energy of 70 cal/gm

Test Rod # and Burnup (GWd/MTU)	**Maximum Fuel Enthalpy (cal/gm)**	**Displaced Sodium Vol. (cm^3)**	**Fuel Type**
REP Na-2 (33)	199	0.13†	UO_2
REP Na-9 (28)	197	0.20	MOX
REP Na-3 (52)	124	0.32‡	UO_2
REP Na-6 (47)	133	0.70	MOX
REP Na-5 (64)	108	0.5	UO_2
REP Na-7 (55)	138*	0.9	MOX

† - Adjusted to account for active fuel column length of 657 mm
‡ - Adjusted to account for active fuel column length of 441 mm
* - Maximum fuel enthalpy without consideration of cladding failure at ~113 cal/gm

Finally, ceramography results at the peak power location for the MOX REP Na-7 test rod and the failed UO_2 REP Na-8 test rod are shown in Figure F-3.4. This comparison finds some significant differences between the appearance of the MOX test rod and the UO_2 test rod. First, the UO_2 pellet exhibits only minor effects of the power pulse with the largest impact in the pellet periphery region. In comparison, the MOX pellet exhibits significant cracking throughout the entire pellet which is indicative of gas expansion. Second, the cladding crack in the UO_2 rod exhibits a mixed brittle/ductile fracture with a limited opening. The cladding of the MOX rod contains a ductile fracture with measurable wall-thinning at the crack faces. The crack opening is considerably larger than that observed in the high burnup UO_2 rod. These results lead to the conclusion that the failure process in high burnup UO_2 fuel rods is controlled more by the ductility of the cladding whereas the failure process in irradiated MOX fuel rods is controlled more by the gas expansion process within the pellet.

This assessment is consistent with positions expressed by other industry experts who have reviewed the results of RIA-simulation tests on irradiated MOX fuel [F-3.1 and F-3.2]. Experimentalists from both the CABRI and NSRR programs have postulated that fission gas within the Pu-rich agglomerates may have enhanced the swelling rate of MOX pellets, leading to more PCMI and higher cladding strains as compared to UO_2 pellets.

Recently, NRC-RES has stated the position that the higher cladding strains observed in the non-failed MOX tests REP Na-6 and REP Na-9 are a result of the higher fission gas release for these rods and are not related to differences in the pellet expansion process [F-3.3]. It is the NRC-RES point of view that the increased cladding radial displacements are due to ballooning-like deformations caused by an increase in the test rod internal pressure from the higher fission gas release. Two observations from post-test examinations discredit this hypothesis. First, the cladding radial deformations for the MOX rods follow closely the axial power distribution and thus the pellet temperatures. However, clad ballooning deformations are typically more localized as exhibited in the NSRR TK-1 and TK-6 tests [F-3.4]. In these tests, localized cladding deformations above 10% were observed at axial positions on the fuel rod that experienced high cladding temperatures due to departure from nucleate boiling (DNB). Second, ceramography examinations find that the entire volume within the cladding is filled with fuel pellet material in the CABRI and NSRR MOX tests, with only narrow pellet cracks observable. This is not the case for the NSRR TK-1 and TK-6 tests which experienced ballooning-like cladding deformations. Ceramography results from TK-1 show large gaps or cracks within the fuel pellet with the appearance that the internal gas pressure within the cracks pushed the fuel pellet pieces outward. Based on these two observations, it is unlikely that the cladding radial deformations observed in the MOX tests REP Na-6 and REP Na-9 were caused by high rod internal pressure leading to ballooning-like deformations. Finally, the results from the high burnup UO_2 test rod REP Na-5 indicate that the presence of high fission gas release does not necessarily lead to enhanced cladding deformations. As shown in Table F-3.1, the cladding strains for REP Na-5 are around 1% which is consistent with pellet thermal expansion even though the fission gas release was greater than 15% for this rod.

In addition to the presence of plutonium isotopes in MOX pellets, a key difference between a UO_2 pellet and a MOX pellet is the uniformity of the fissile material. In UO_2 pellets, the initial fissile material (^{235}U) is distributed uniformly within the pellet. As burnup proceeds, the self-shielding effect and the formation of plutonium isotopes near the pellet periphery leads to a non-uniform fissile content and a variation in the burnup profile across the pellet. The local burnup in the periphery of a UO_2 pellet can be 2 to 3 times the pellet average burnup and microstructural changes occur in the pellet periphery beyond a local burnup of ~65 GWd/MTU. These changes, referred to has the high burnup structure (HBS) or rim structure, causes the gaseous fission products to be removed from the grains and relocated to bubbles on the grain boundaries. This behavior is limited to the outer ~200 microns of the pellet periphery. In MOX pellets, the fissile isotopes are not distributed uniformly, but are located in Pu-rich clusters or agglomerates distributed randomly throughout the pellet. Because of the heterogeneity of MOX pellets, the enriched Pu agglomerates accumulate burnup much faster than the pellet average burnup. The resulting burnup distribution contains localized spikes within the agglomerates. Furthermore, Pu-rich agglomerates form a HBS with a large inventory of fission gas within grain boundary bubbles. As a result, MOX pellets have HBS locally distributed throughout the entire pellet.

The industry assessment of MOX fuel behavior finds that the pellet expansion process in MOX rods is 1.5 to 2.0 times greater than UO_2 fuel rods at the same radial average peak fuel enthalpy level. Others have proposed that the cause of the enhanced pellet expansion process is the large inventory of fission gas bubbles on the grain boundaries in the regions of Pu-rich agglomerates

[F-3.1 and F-3.2]. The higher pellet expansion increases the PCMI forces on the cladding, thus increasing cladding deformations in MOX fuel rods. As a result, the failure of REP Na-7 at a radial average peak fuel enthalpy of 113 cal/gm does not represent a UO_2 fuel rod at the same fuel enthalpy.

References:

F-3.1 J. Papin, B. Cazalis, J.M. Frizonnet, E. Fédérici, F. Lemoine, "Synthesis of CABRI-RIA Tests Interpretation," *Eurosafe Forum 2003*, Paris, November 2003.

F-3.2 Sasajima, H., et.al., "Behavior of Irradiated ATR/MOX Fuel under Reactivity Initiated Accident Conditions," Journal of Nuclear Science and Technology, Vol. 37, No. 5, May 2000, pp. 455-464.

F-3.3 Meyer, R.O., Presentation to the Fuels Subcommittee of the Advisory Committee for Reactor Safeguards, July 28, 2005.

F-3.4 Fuketa, T., Sasajima, H., and Sugiyama, T., "Behavior of High-Burnup PWR Fuels with Low-Tin Zircaloy-4 Cladding Under Reactivity-Initiated-Accident Conditions," Nuclear Technology, Vol. 133, Jan. 2001.

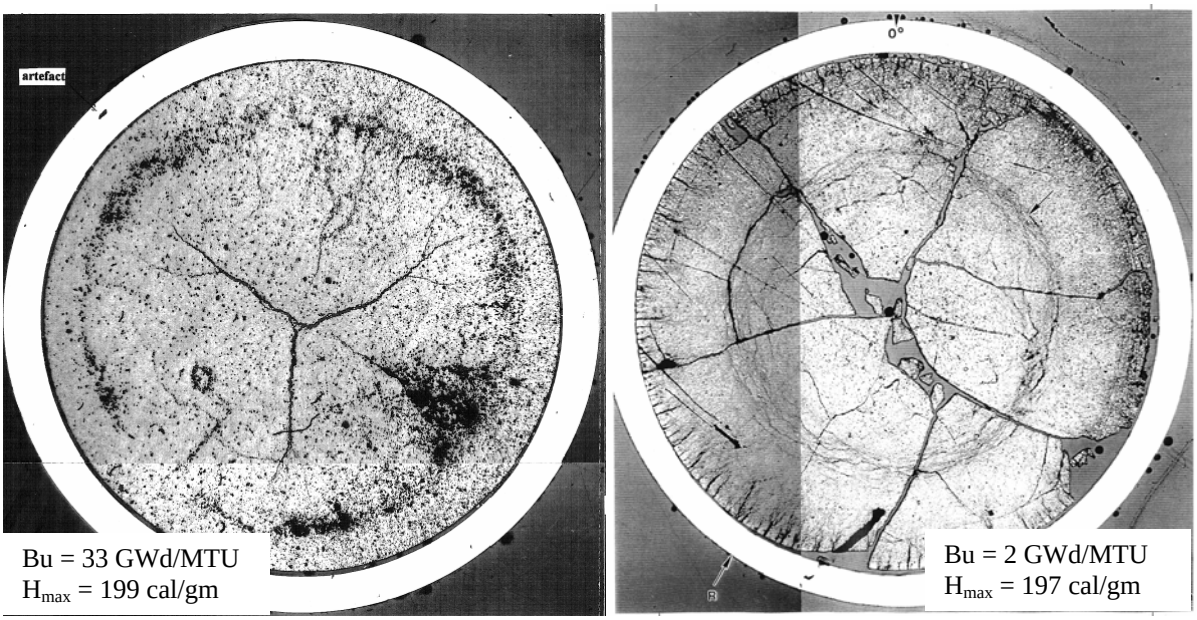

(a) UO_2 Rod REP Na-2 (b) MOX Rod REP Na-9

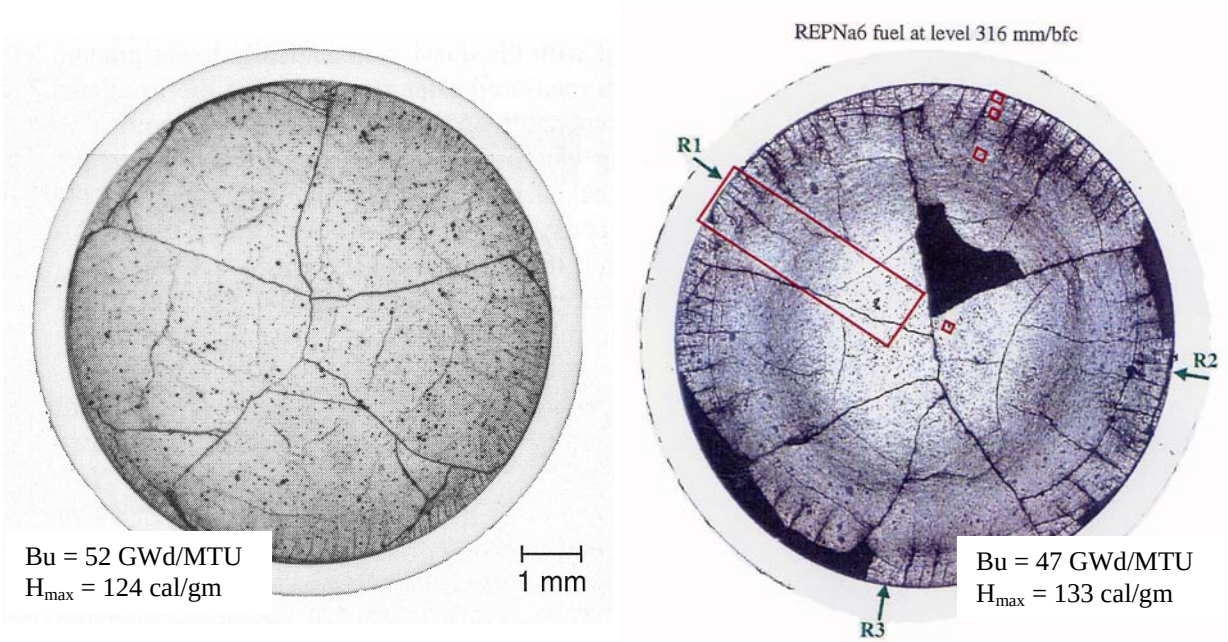

(c) UO_2 Rod REP Na-3 (d) MOX Rod REP Na-6

Figure F-3.1. Ceramography images near the peak power location from RIA-simulation tests on both UO_2 and MOX fuel in the CABRI reactor.

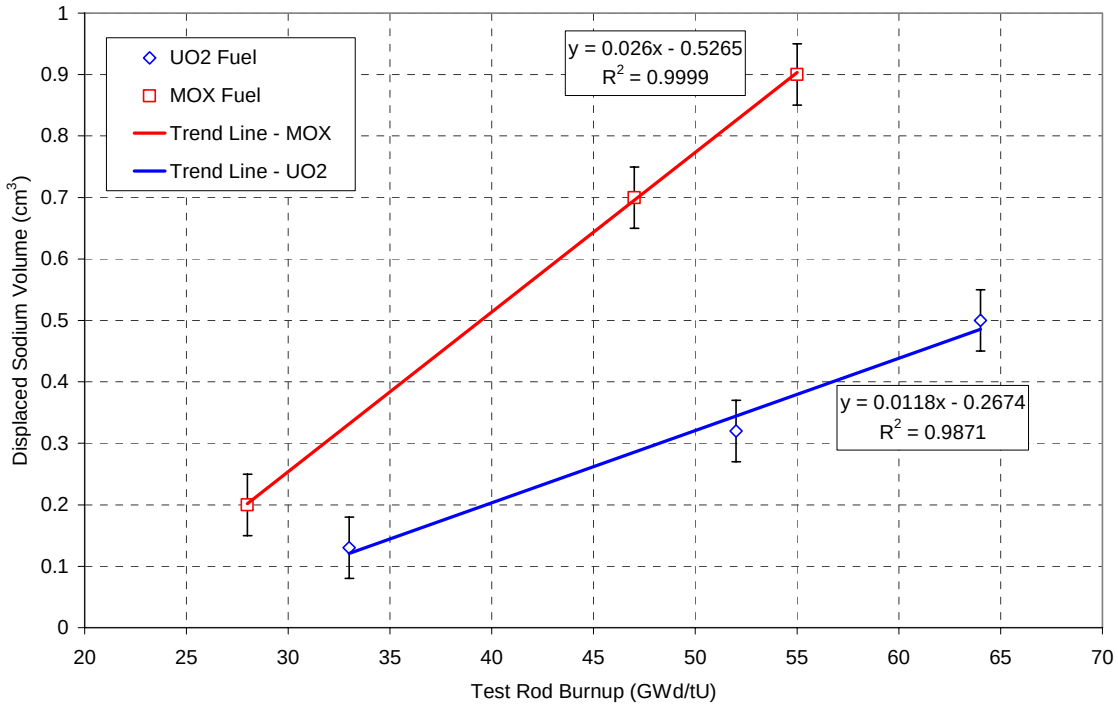

Figure F-3.2 Displaced sodium volume at an injected energy of 70 cal/gm as a function of test rod burnup for both MOX and UO_2 rods tested in the CABRI facility.

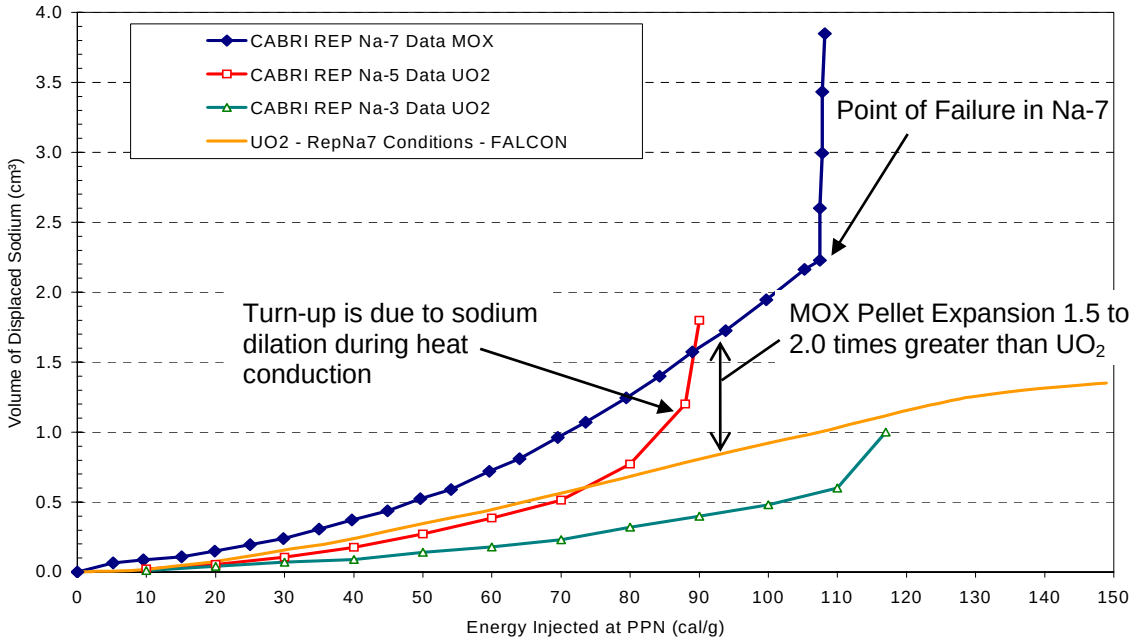

Figure F-3.3 Displaced sodium volume data for the MOX REP Na-7 and the UO_2 REP Na-3 and REP Na-5 rods in CABRI as a function of the energy deposition at the peak power node (PPN).

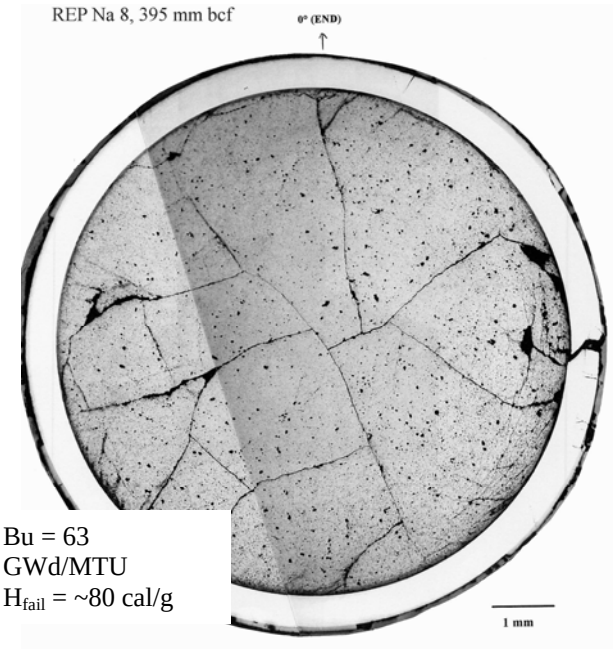

Bu = 63
GWd/MTU
H_{fail} = ~80 cal/g

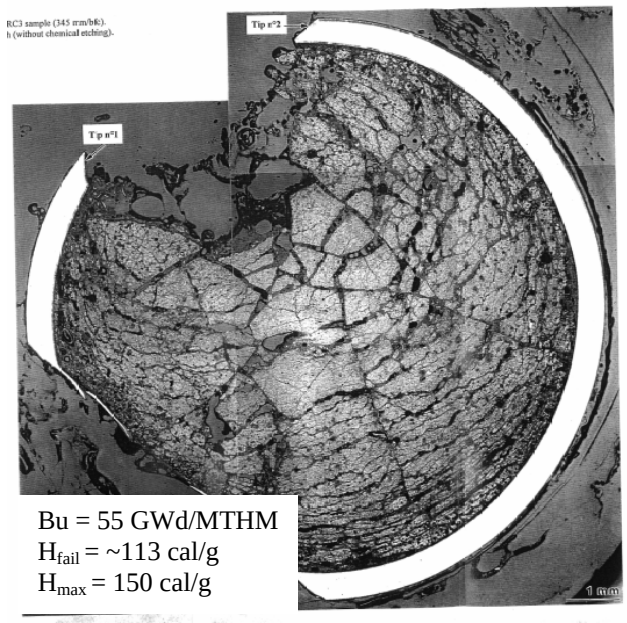

Bu = 55 GWd/MTHM
H_{fail} = ~113 cal/g
H_{max} = 150 cal/g

(a) UO_2 Rod REP Na-8 (b) MOX Rod REP Na-7

Figure F-3.4 Ceramography images near the peak power location from UO_2 and MOX tests with cladding failure.

Response to Requests for Additional Information (RAI's)
NRR Safety Evaluation Report – Project No. 689

F-3. The single mixed-oxide (MOX) fuel failure in the French Test Reactor (CABRI) series was assumed to be different from the uranium dioxide (UO_2) failures because of inhomogeneities and a gas expansion model was invoked for only this test. We are not convinced that gas expansion can significantly enhance the cladding stress as postulated. Thermal expansion of MOX and UO_2 are almost identical, so the loading from expansion should not depend on homogeneity.

Response to RAI F-3

Experimental data from both the CABRI and NSRR RIA tests show that irradiated MOX fuel behavior is different than irradiated UO_2 fuel under RIA conditions at similar burnup and fuel enthalpy levels [F-3.1, F-3.2]. Post-test ceramography examinations and measurements of cladding permanent hoop strain and fission gas release reported in the literature finds that MOX fuel experiences stronger pellet-cladding mechanical interaction (PCMI) and higher fission gas release during rapid energy deposition events as compared to UO_2 fuel. These post-test observations are supported by in-pile measurements of dynamic fuel rod volume changes during the CABRI experiments.

Table F-3.1 contains the measured maximum residual cladding hoop strain and the transient fission gas release for several rods tested in the CABRI reactor. As can be seen, the MOX test rods experienced about two times the cladding hoop strain and fission gas release as compared to the UO_2 test rods with similar burnup levels and maximum fuel enthalpy. The residual cladding hoop strain for the UO_2 test REP Na-3 is shown in Table F-3.1 with a range of values due to uncertainties in estimating the residual hoop strain from the pre-test rod and post-test diameter measurements. The uncertainty arises from the treatment of the outer cladding surface oxide layer thickness in the calculation of the residual strain.

Table F-3.1 Comparison of UO_2 and MOX Rods in CABRI REP Na Tests

Test Rod # and Burnup (GWd/MTU)	Maximum Fuel Enthalpy (cal/gm)	Max. Residual Hoop Strain (%)	Fission Gas Release (%)	Fuel Type
REP Na-2 (33)	199	3.5	5.5	UO_2
REP Na-9 (28)	197	7.2	33.4	MOX
REP Na-3 (52)	124	1.3 - 2.2*	13.7	UO_2
REP Na-6 (47)	133	2.6	21.0	MOX
REP Na-5 (64)	108	1.1	15.1	UO_2

* - Uncertainty in the estimation of the cladding strain for this test

Figure F-3.1 contains ceramography images from the UO_2 tests REP Na-2 and REP Na-3 and the MOX tests REP Na-6 and REP Na-9. It should be noted that some grain pullout has occurred in the preparation of the REP Na-2 ceramography sample. Further some fuel pieces have also been removed during the preparation of the MOX samples. These visual appearances are artifacts of the sample preparation process and do not reflect the actual behavior of the fuel pellet.

The appearance of the irradiated MOX fuel rods is significantly different than UO_2 rods. The MOX fuel exhibits a higher density of radial cracks near the pellet periphery and circumferential cracks at the mid-pellet radius location. The presences of these fine cracks are an indication of the high level of PCMI experienced in these rods. These images further show that large swelling has occurred in the MOX fuel pellets and there is almost no increase in the free volume due to cladding strains above 3%. In comparison, the pellet-cladding gap in the UO_2 test rod REP Na-2 is clearly evident and post-test measurements finds that the pellet-cladding gap has increased from ~15 microns to ~50 microns. The change in pellet-cladding gap thickness for REP Na-2 is representative of the amount of pellet thermal expansion experienced during the power pulse.

Another indication of the enhanced PCMI due to pellet swelling in the MOX rods comes from the dynamic rod volume changes measured in the CABRI reactor. Table F-3.2 provides the estimated sodium volume displaced from the flow channel in UO_2 and MOX rods tested in CABRI at an injected energy of 70 cal/gm. The amount of sodium displaced from the flow channel is determined by integrating the difference between the channel outlet and inlet flowmeter measurements. Sodium volume displacement from the flow channel is caused mostly by the radial and axial expansion of the test rod during the early energy deposition phase of the RIA tests in CABRI. As a result, early time measurements of the displaced sodium volume represent the fuel rod volume change due to PCMI. In the later portion of the transient, heat conduction causes dilation of the sodium, leading to a further increase in displaced sodium volume. Because different fuel column lengths were used in the CABRI tests, the displaced sodium volume results shown in Table F-3.2 have been normalized to an active fuel column length of ~560 mm.

The measured values shown in Table F-3.2 demonstrate that the fuel rod volume increases at a faster rate in the MOX rods as compared to the UO_2 rods during the energy deposition phase of the experiments. The effect of MOX on the fuel rod expansion process is shown clearly in Figure F-3.2 which contains a plot of the displaced sodium volume at an injected energy of 70 cal/gm as a function of test rod burnup. The comparison of the displaced sodium volume was selected at a fuel enthalpy of 70 cal/gm because the fuel rod volume change is caused primarily by PCMI during the early phase of the energy deposition. Later in the power pulse, sodium dilation from heat conduction from the fuel rod further increases the displaced sodium volume beyond that caused by PCMI. For the UO_2 rods, the displaced sodium volume results shown in Table F-3.2 and Figure F-3.2 reflect the amount of fuel rod volume change caused by thermal expansion of the UO_2 pellet. This has been confirmed by analysis. Such is not the case for the MOX rods, where the increase in fuel rod volume is much higher than expected based only on pellet thermal expansion. From the linear trend of the data shown in Figure F-3.2, the effect of burnup on the fuel rod expansion rate is about 2 times higher in MOX fuel than a UO_2 fuel. An example of this difference is shown in Figure F-3.3 which compares the measured displaced sodium volume for two UO_2 test rods, REP Na-3 and REP Na-5 with the results from the MOX

REP Na-7 test as a function of injected energy. Also shown for comparison are the FALCON analysis results for REP Na-7 assuming that UO_2 thermal expansion is the only contribution to PCMI. These results highlight the faster rate of fuel rod volume increase in the MOX test REP Na-7 as compared to the UO_2 tests with similar burnup levels. The FALCON analysis results also confirm that unlike the fuel rod volume increase in the UO_2 rods, which is caused by pellet thermal expansion, REP Na-7 has a fuel rod volume increase that is much higher than that expected from simply pellet thermal expansion. Enhanced swelling of the pellet by the fission gas located on grain boundaries is the most likely explanation for the behavior of the MOX rods.

Table F-3.2 Displaced Sodium Volume for UO_2 and MOX Rods in CABRI REP Na Tests at an Injected Energy of 70 cal/gm

Test Rod # and Burnup (GWd/MTU)	**Maximum Fuel Enthalpy (cal/gm)**	**Displaced Sodium Vol. (cm^3)**	**Fuel Type**
REP Na-2 (33)	199	0.13†	UO_2
REP Na-9 (28)	197	0.20	MOX
REP Na-3 (52)	124	0.32‡	UO_2
REP Na-6 (47)	133	0.70	MOX
REP Na-5 (64)	108	0.5	UO_2
REP Na-7 (55)	138*	0.9	MOX

† - Adjusted to account for active fuel column length of 657 mm
‡ - Adjusted to account for active fuel column length of 441 mm
* - Maximum fuel enthalpy without consideration of cladding failure at ~113 cal/gm

Finally, ceramography results at the peak power location for the MOX REP Na-7 test rod and the failed UO_2 REP Na-8 test rod are shown in Figure F-3.4. This comparison finds some significant differences between the appearance of the MOX test rod and the UO_2 test rod. First, the UO_2 pellet exhibits only minor effects of the power pulse with the largest impact in the pellet periphery region. In comparison, the MOX pellet exhibits significant cracking throughout the entire pellet which is indicative of gas expansion. Second, the cladding crack in the UO_2 rod exhibits a mixed brittle/ductile fracture with a limited opening. The cladding of the MOX rod contains a ductile fracture with measurable wall-thinning at the crack faces. The crack opening is considerably larger than that observed in the high burnup UO_2 rod. These results lead to the conclusion that the failure process in high burnup UO_2 fuel rods is controlled more by the ductility of the cladding whereas the failure process in irradiated MOX fuel rods is controlled more by the gas expansion process within the pellet.

This assessment is consistent with positions expressed by other industry experts who have reviewed the results of RIA-simulation tests on irradiated MOX fuel [F-3.1 and F-3.2]. Experimentalists from both the CABRI and NSRR programs have postulated that fission gas within the Pu-rich agglomerates may have enhanced the swelling rate of MOX pellets, leading to more PCMI and higher cladding strains as compared to UO_2 pellets.

Recently, NRC-RES has stated the position that the higher cladding strains observed in the non-failed MOX tests REP Na-6 and REP Na-9 are a result of the higher fission gas release for these rods and are not related to differences in the pellet expansion process [F-3.3]. It is the NRC-RES point of view that the increased cladding radial displacements are due to ballooning-like deformations caused by an increase in the test rod internal pressure from the higher fission gas release. Two observations from post-test examinations discredit this hypothesis. First, the cladding radial deformations for the MOX rods follow closely the axial power distribution and thus the pellet temperatures. However, clad ballooning deformations are typically more localized as exhibited in the NSRR TK-1 and TK-6 tests [F-3.4]. In these tests, localized cladding deformations above 10% were observed at axial positions on the fuel rod that experienced high cladding temperatures due to departure from nucleate boiling (DNB). Second, ceramography examinations find that the entire volume within the cladding is filled with fuel pellet material in the CABRI and NSRR MOX tests, with only narrow pellet cracks observable. This is not the case for the NSRR TK-1 and TK-6 tests which experienced ballooning-like cladding deformations. Ceramography results from TK-1 show large gaps or cracks within the fuel pellet with the appearance that the internal gas pressure within the cracks pushed the fuel pellet pieces outward. Based on these two observations, it is unlikely that the cladding radial deformations observed in the MOX tests REP Na-6 and REP Na-9 were caused by high rod internal pressure leading to ballooning-like deformations. Finally, the results from the high burnup UO_2 test rod REP Na-5 indicate that the presence of high fission gas release does not necessarily lead to enhanced cladding deformations. As shown in Table F-3.1, the cladding strains for REP Na-5 are around 1% which is consistent with pellet thermal expansion even though the fission gas release was greater than 15% for this rod.

In addition to the presence of plutonium isotopes in MOX pellets, a key difference between a UO_2 pellet and a MOX pellet is the uniformity of the fissile material. In UO_2 pellets, the initial fissile material (^{235}U) is distributed uniformly within the pellet. As burnup proceeds, the self-shielding effect and the formation of plutonium isotopes near the pellet periphery leads to a non-uniform fissile content and a variation in the burnup profile across the pellet. The local burnup in the periphery of a UO_2 pellet can be 2 to 3 times the pellet average burnup and microstructural changes occur in the pellet periphery beyond a local burnup of ~65 GWd/MTU. These changes, referred to has the high burnup structure (HBS) or rim structure, causes the gaseous fission products to be removed from the grains and relocated to bubbles on the grain boundaries. This behavior is limited to the outer ~200 microns of the pellet periphery. In MOX pellets, the fissile isotopes are not distributed uniformly, but are located in Pu-rich clusters or agglomerates distributed randomly throughout the pellet. Because of the heterogeneity of MOX pellets, the enriched Pu agglomerates accumulate burnup much faster than the pellet average burnup. The resulting burnup distribution contains localized spikes within the agglomerates. Furthermore, Pu-rich agglomerates form a HBS with a large inventory of fission gas within grain boundary bubbles. As a result, MOX pellets have HBS locally distributed throughout the entire pellet.

The industry assessment of MOX fuel behavior finds that the pellet expansion process in MOX rods is 1.5 to 2.0 times greater than UO_2 fuel rods at the same radial average peak fuel enthalpy level. Others have proposed that the cause of the enhanced pellet expansion process is the large inventory of fission gas bubbles on the grain boundaries in the regions of Pu-rich agglomerates

[F-3.1 and F-3.2]. The higher pellet expansion increases the PCMI forces on the cladding, thus increasing cladding deformations in MOX fuel rods. As a result, the failure of REP Na-7 at a radial average peak fuel enthalpy of 113 cal/gm does not represent a UO_2 fuel rod at the same fuel enthalpy.

References:

F-3.1 J. Papin, B. Cazalis, J.M. Frizonnet, E. Fédérici, F. Lemoine, "Synthesis of CABRI-RIA Tests Interpretation," *Eurosafe Forum 2003*, Paris, November 2003.

F-3.2 Sasajima, H., et.al., "Behavior of Irradiated ATR/MOX Fuel under Reactivity Initiated Accident Conditions," Journal of Nuclear Science and Technology, Vol. 37, No. 5, May 2000, pp. 455-464.

F-3.3 Meyer, R.O., Presentation to the Fuels Subcommittee of the Advisory Committee for Reactor Safeguards, July 28, 2005.

F-3.4 Fuketa, T., Sasajima, H., and Sugiyama, T., "Behavior of High-Burnup PWR Fuels with Low-Tin Zircaloy-4 Cladding Under Reactivity-Initiated-Accident Conditions," Nuclear Technology, Vol. 133, Jan. 2001.

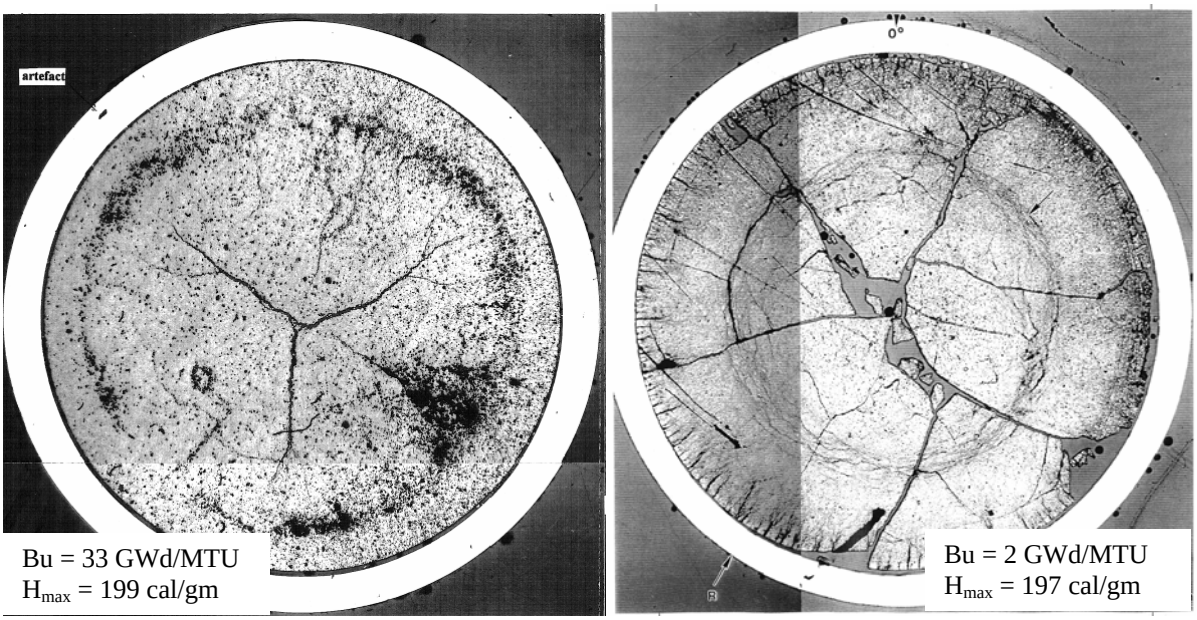

(a) UO_2 Rod REP Na-2 (b) MOX Rod REP Na-9

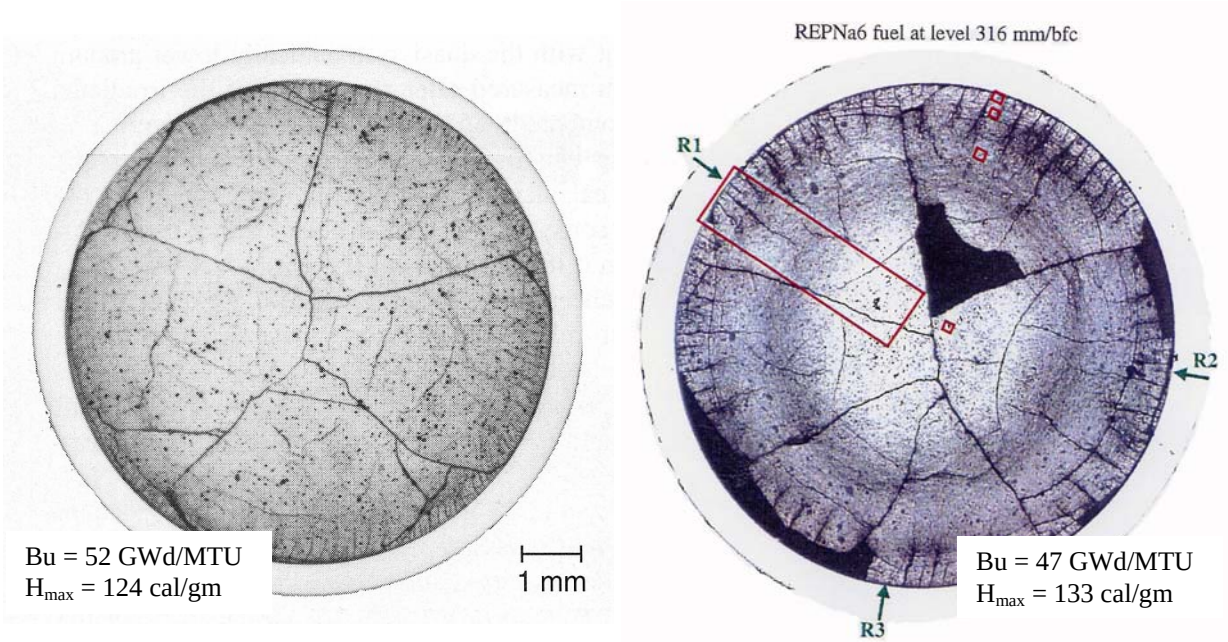

(c) UO_2 Rod REP Na-3 (d) MOX Rod REP Na-6

Figure F-3.1. Ceramography images near the peak power location from RIA-simulation tests on both UO_2 and MOX fuel in the CABRI reactor.

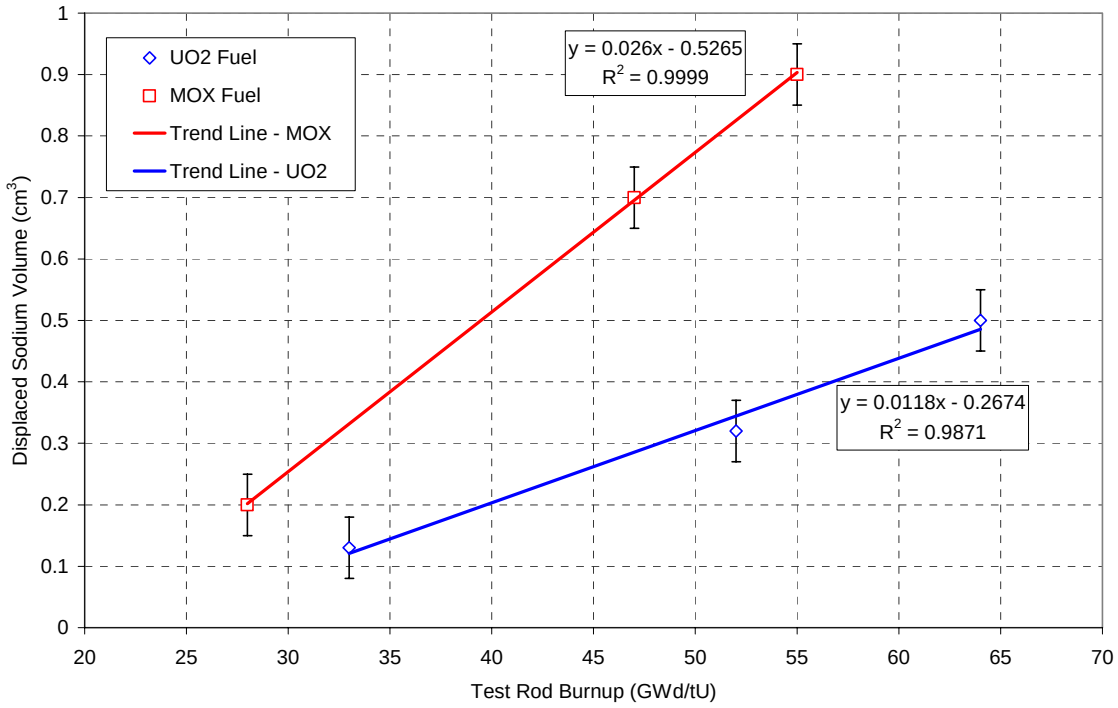

Figure F-3.2 Displaced sodium volume at an injected energy of 70 cal/gm as a function of test rod burnup for both MOX and UO_2 rods tested in the CABRI facility.

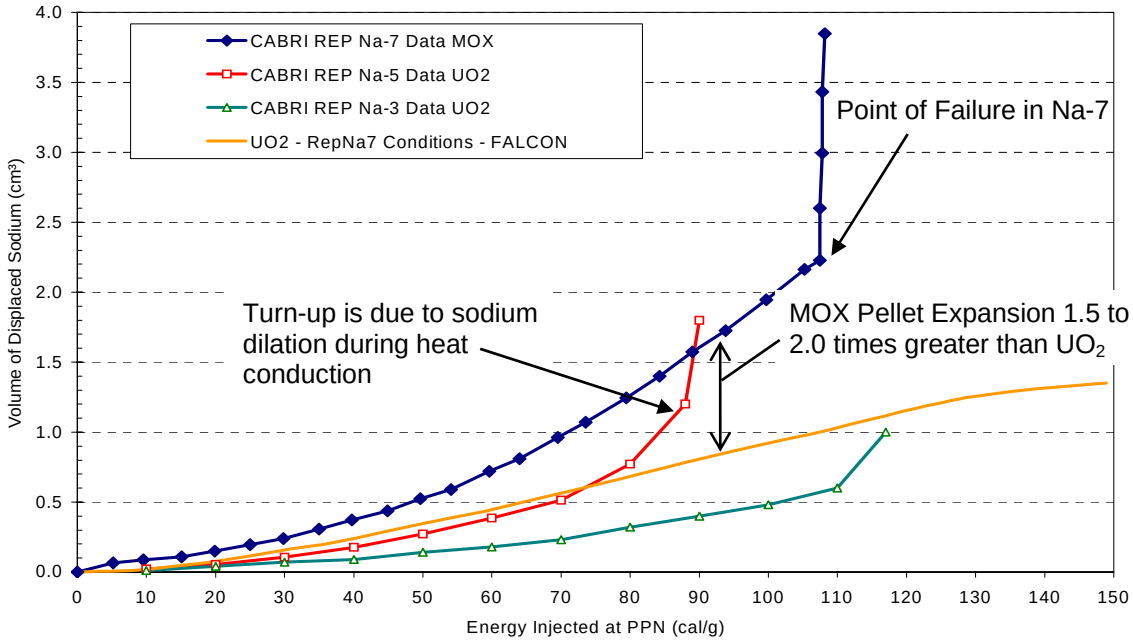

Figure F-3.3 Displaced sodium volume data for the MOX REP Na-7 and the UO_2 REP Na-3 and REP Na-5 rods in CABRI as a function of the energy deposition at the peak power node (PPN).

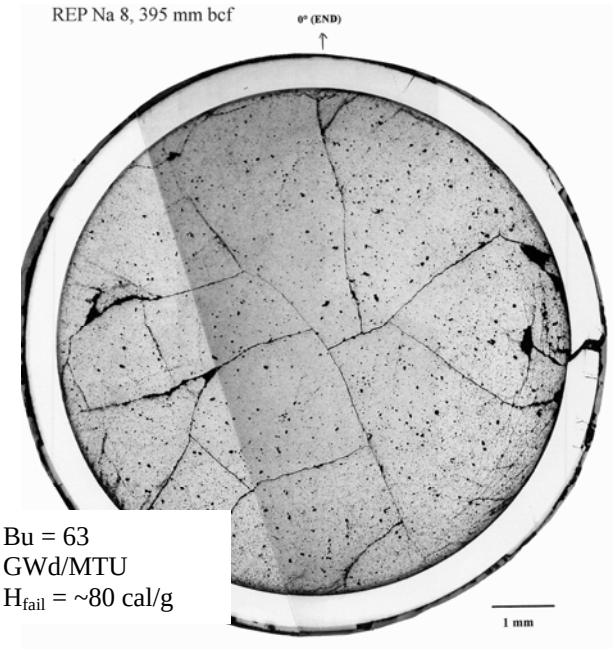

Bu = 63
GWd/MTU
H_{fail} = ~80 cal/g

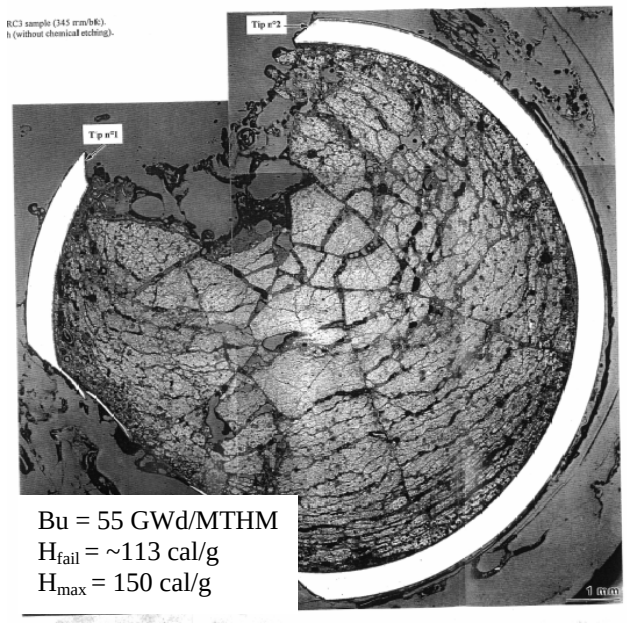

Bu = 55 GWd/MTHM
H_{fail} = ~113 cal/g
H_{max} = 150 cal/g

(a) UO_2 Rod REP Na-8 (b) MOX Rod REP Na-7

Figure F-3.4 Ceramography images near the peak power location from UO_2 and MOX tests with cladding failure.

Response to Requests for Additional Information (RAI's)
NRR Safety Evaluation Report – Project No. 689

F-4. We agree that the method of determining oxidation of the two Special Power Excursion Reactor Test tests was not accurate. We do not agree that adjusting that result for densities (Pilling-Bedworth ratio) corrects the problem. Our previous analysis for the irradiation conditions of these specimens indicates that the oxide thickness should be less than 65 microns, rather than larger as was concluded in the report. Moving these points out to 130 microns produces a non-conservative acceptance limit.

Response to RAI F-4

The Industry review of the Special Power Excursion Reactor Test (SPERT) test rods 756 and 859 tested in the Capsule Driver Core (CDC) finds that the failure of these rods by PCMI was caused by the excessive cladding outer surface corrosion combined with the thin cladding wall thickness and the low coolant temperature. The fuel design, cladding material, and the conditions during the base irradiation were not typical of modern BWR fuel rods and the performance of these two test rods should not be considered representative of current high burnup fuel. Their use directly in establishing a fuel rod failure threshold is overly conservative because of these atypical characteristics. However, the test rod failures in the SPERT-CDC program are valuable in understanding the failure processes during the PCMI phase of an RIA event, provided the atypical cladding wall thickness and oxide layer thickness are considered properly.

No direct measurement of the oxide thickness was made in the case of SPERT test rods 756 and 859 prior to testing in the Capsule Driver Core. Only visual examinations and profilometry data were obtained after the base irradiation in the Engineering Test Reactor (ETR) [F-4.1]. The only reference to the outer surface corrosion conditions for these rods is a single statement in Reference F-4.1 in the pre-test description of Rod 756. This statement is given below;

> *"Visually, the rod appeared to be in good condition, but exhibited more corrosion than any of the previous rods. The corrosion increased the measured diameter of the rod by about 0.005 in. and occurred over the active length of the cladding only."*

Several analysts have used the increase in outer diameter as a method to estimate the oxide layer thickness for these two rods. Converting the 5 mils (0.005 in) value to microns and dividing by two yields an apparent oxide thickness of 64 microns using this method, which is the value used in RIL 0401. This approach does not consider the fact that the oxidation process consumes Zr atoms from the cladding wall, thus thinning it, and the density difference between ZrO_2 molecules and Zr atoms. Because of these factors, the oxide thickness estimated using the method above would be underpredicted by a factor ranging between 2.0 and 2.8, depending on the characteristics of the oxide layer. The appropriate method to estimate the oxide layer thickness from the pre-test profilometry data is by the use of the Pilling-Bedworth ratio.

The reaction of zirconium alloys with water is given by;

$$Zr + 2H_2O \Rightarrow ZrO_2 + 2H_2 \qquad \text{F-4.1}$$

In this process, a zirconium atom on the cladding outer surface reacts with a water molecule in the coolant to form zirconium oxide (ZrO_2) molecules and hydrogen molecules. If the volume occupied by the ZrO_2 molecules were identical to the Zr atoms, then no change in the rod outer diameter would occur and the metal-oxide interface location would progressively move inward towards the inner cladding surface as the corrosion process proceeded. In this case, it would not be possible to estimate the thickness of the oxide layer by measuring the final cladding outer diameter and subtracting the as-manufactured cladding outer diameter. In reality, the theoretical density of ZrO_2 is lower than zirconium and the oxidation process results in the formation of porosity that further decreases the ZrO_2 density as compared to the zirconium reacted. Any increase in outer diameter of the cladding is due to the volume difference between ZrO_2 and zirconium.

Generally, the Pilling-Bedworth ratio is used to address the differences in volume occupied by an oxide relative to the reacted metal. The Pilling-Bedworth (P-B) ratio is defined as the volume ratio of the oxide formed by the reaction to the metal consumed [F-4.2]. Mathematically, the ratio is expressed as:

$$P\text{–}B = \left[\frac{W_{ox}}{W_m}\right] \cdot \left[\frac{\rho_m}{\rho_{ox}}\right] \qquad \text{F-4.2}$$

where

W_{ox} = molecular weight of oxide,
W_m = atomic weight of metal,
ρ_{ox} = density of oxide, and
ρ_m = density of metal.

The atomic weight of Zr is 91.2 and the molecular weight of ZrO_2 is taken as 123.2 [F-4.3]. Therefore the first term in equation F-4.2 9 (weight ratio of ZrO_2 to Zr) is (123.2/91.2) = 1.351.

The density of Zircaloy (at room temperature) is approximately 6550 kg/m^3 (6.55 g/cm^3) [F-4.4]. Using these values, Equation F-4.2 can be rewritten as;

$$P\text{-}B = 8.848/\rho_{ox} \qquad \text{F-4.3}$$

where ρ_{ox} is in g/cm^3

The only remaining parameter to determine the P-B ratio is the ZrO_2 oxide density. The theoretical maximum density of ZrO_2 may be taken to be 5.8 gm/cm^3 [F-4.5, F-4.6], which is the dark or black oxide near the metal/oxide interface. The white or lighter oxide is generally taken to have a density of approximately 5.6 gm/cm^3, which corresponds to a PB ratio of 1.58 [F-4.11]. On the other hand, the P-B ratio is commonly reported in the literature as 1.56 [F-4.7,F-4.8],

which corresponds to an oxide density of 5.67 gm/cm^3. From Equation F-4.3, the ZrO_2 density and P-B ratio are provided in Table F-4.1 and presented graphically in Figure F-4.1, for various oxide densities or P-B ratios reported in the literature for zirconium oxide.

Table F-4.1. Pilling Bedworth ratio as a function of zirconium oxide density

Density of Zr-oxide	Weight gain (mg/dm^2) per micron of ZrO_2	Porosity (%)	P-B Ratio
5.057	13.14	12.8%	1.750 [F-4.9]
5.35 [F-4.10]	13.90	7.8%	1.654
5.6 [F-4.11]	14.55	3.4%	1.580
5.67	14.7	2.2%	1.56 [F-4.7]
5.8 [F-4.5]	15.06	0.0%	1.526

Knowing the P-B ratio, it is possible to estimate the oxide layer thickness from the cladding outer diameter measurement. The end of irradiation cladding outer diameter (D_f) can be written as;

$$D_f = D_i - \Delta D_m + \Delta D_{ox} + \Delta D_{PCMI} \qquad \text{F-4.4}$$

where,

D_i = initial cladding outer diameter
ΔD_m = change in outer diameter due to metal loss by corrosion
ΔD_{ox} = change in outer diameter due to oxide layer growth
ΔD_{PCMI} = change in diameter due to pellet-cladding mechanical interaction (PCMI)

Since these rods were base irradiated under near BWR coolant temperature and pressure conditions along with a low fast flux, changes in cladding diameter due to Zircaloy creep can be neglected for this evaluation. The volume of metal loss by corrosion and the volume of ZrO_2 can be estimated by;

$$V_m = \pi \cdot R_{od} \cdot L \cdot \Delta D_m \qquad \text{F-4.5}$$

$$V_{ox} = \pi \cdot R_{od} \cdot L \cdot \Delta D_{ox} \qquad \text{F-4.6}$$

where

R_{od} = the outer radius of the cladding
L = the length of the cladding undergoing oxidation

The Pilling-Bedworth ratio is defined as the ratio of the oxide volume to metal consumed volume, which can be written as;

$$P - B = \frac{V_{ox}}{V_m} = \frac{\Delta D_{ox}}{\Delta D_m} \qquad \text{F-4.7}$$

Combining Equations F-4.4 and F-4.7, the change in outer diameter due to oxide layer growth can be written as;

$$\Delta D_{ox} = \frac{D_f - D_i - \Delta D_{PCMI}}{\left[1 - \frac{1}{P - B}\right]} \qquad \text{F-4.8}$$

Assuming the cladding outer diameter change is caused entirely by the corrosion process ($\Delta D_{PCMI} = 0$), the estimated oxide layer thickness ($\Delta D_{ox}/2$) from Equation F-4.8 ranges between 148 and 184 microns for the Pilling-Bedworth ratios shown in Table F-4.1. This is much higher than the 65 microns used in the RIL 0401 evaluation.

Using Equation F-4.8 and setting ΔD_{ox} to 64 microns it is possible to estimate the required amount of cladding outer displacement by PCMI (ΔD_{PCMI}) during the base irradiation to yield the pre-test dimensional change. The PCMI diameter change would need to be 41 microns (1.6 mils) or approximately 65% of the total amount of the dimensional changes observed in the pre-test examinations for these rods to yield an outer surface corrosion layer thickness of 64 microns. This evaluation highlights the importance of considering the metal consumption and volume expansion during the oxidation process on the cladding dimensional changes.

FALCON calculations have been performed for the base irradiation of rods 756 and 859 to gain an understanding of the corrosion behavior during irradiation in the Experimental Test Reactor (ETR) and to estimate the amount of PCMI induced cladding displacements that may have occurred during the base irradiation. Two factors about these rods make it possible that the corrosion behavior of these rods could be atypical compared to standard PWR and BWR fuel rods. First, the rod diameter and cladding wall thickness were considerably smaller than modern fuel rods. The fuel rod outer diameter was 0.3125 in (7.938 mm) and the cladding wall thickness was 20 mils (508 microns), which is about 30% small than a 10x10 BWR rod and about 20% small than a 17x17 PWR fuel rod. This translates into a higher cladding surface heat flux in the SPERT-CDC as compared to modern LWR fuel rods at equivalent linear power levels. Also, the thinner cladding wall thickness in the SPERT-CDC increases the hydrogen volume fraction as compared to modern cladding for the same corrosion layer thickness. Second, the fuel rod linear powers experienced by these rods were in the range of 14 to 16 kW/ft (46 to 52 kW/m) with maximum values of 18 kW/ft (59 kW/m). The combination of these two factors produces a cladding surface heat flux that was between 1.5 to 2.5 times greater than a peak operating fuel rod in a BWR.

A description of the FALCON calculations for rod 859 can be found in Appendix F-4.A. The main conclusions from this analysis are;

1). The high cladding heat flux combined with a corrosion layer of ~20 microns results in a condition of accelerated corrosion rate due to the feedback of the thermal resistance of the corrosion layer on the metal-oxide interface temperature. As shown in Figure F-4.2, the accelerated corrosion occurred sometime after 150 days of irradiation. The corrosion would easily have exceeded 50 microns at the end of life and most likely exceeded 100 microns, depending on the metallurgical and surface conditions of the cladding. As a consequence of

this effect, high levels of corrosion would be expected only for the test rods 859 and 756 because of their longer resistance time in the ETR (~216 days). Visual examinations of the lower burnup rods 684 and 685 (~13 GWd/tU) found no outer surface diameter changes from the base irradiation nor any notable outer corrosion features after 98 days of operation [F-4.1]. Based on the results shown in Figure F-4.2 rods 685 and 684 would have had less than 10 microns of outer surface corrosion which is consistent with the visual observations.

2). FALCON calculated only limited outward cladding deformations due to PCMI during the base irradiation of test rod 859. Pellet swelling is calculated to close the fuel-cladding gap after ~50 days of irradiation; however, insufficient PCMI is developed to induce any significant permanent deformations in the cladding during the remainder of the irradiation. This suggests that cladding oxidation caused most of the fuel rod dimensional changes observed in the pre-test examinations.

This review finds that the atypical fuel rod design, cladding material, and base irradiation conditions for test rods 859 and 756 led to excessive corrosion and hydrogen uptake that significantly impacted the cladding residual ductility, thus, making them susceptible to failure by PCMI during the RIA power pulse. For the thin-walled cladding used in the design of test rods 859 and 756 (~508 microns), a corrosion thickness greater than 90 microns exceeds the oxide to cladding thickness ratio used to develop the fuel rod failure threshold in the Topical Report. Moreover, the impact of the reduced residual cladding ductility caused by the excessive outer surface corrosion was further amplified by the room temperature coolant conditions used in the SPERT-CDC test capsules. Based on all these factors, the industry has determined that the irradiated SPERT-CDC tests 859 and 756 should not be used in the development of performance limits for modern LWR fuel. Use of these tests would result in an overly conservative estimate of the fuel enthalpy required to fail the cladding of modern fuel designs.

References

F-4.1 Miller, R.W., “The Effects of Burnup on Fuel Failure, II. Power Burst Tests on Fuel Rods with 13,000 and 32,000 MWd/MTU Burnup,” IN-ITR-118, April 1971.

F-4.2 M. G. Fontana and N. G. Greene, "Corrosion Engineering," McGraw-Hill, Inc., 1978, p.347.

F-4.3 F. Walker, D. Miller and F. Feiner, "Chart of the Nuclides," Thirteenth Edition, GE, 1984.

F-4.4 J. K. Hohorst et al, "SCDAP/RELAP5/MOD2 Code Manual, Volume 4: MATPRO-A, Library of Materials Properties for Light-Water-Reactor Accident Analysis," NUREG/CR-5273, 1990, p. 4.5-25.

F-4.5 J. K. Hohorst et al, "SCDAP/RELAP5/MOD2 Code Manual, Volume 4: MATPRO-A, Library of Materials Properties for Light-Water-Reactor Accident Analysis," NUREG/CR-5273, 1990, p. 5.5-2.

F-4.6 K. E. Gilchrist, "Thermal Property Measurements on Zircaloy-2 and Associated Oxide Layers," Journal of Nuclear Materials, 62, 1976, pp. 257-264.

F-4.7 "Waterside corrosion of zirconium alloys in nuclear power plants," IAEA-TECDOC-996, January 1998, p. 40.

F-4.8 A. J. Machiels, "Corrosion of Zircaloy-Clad LWR Fuel Rods," in Metals Handbook, Ninth Edition, Volume 13, Corrosion, ASM International, 1987, p. 946.

F-4.9 H. Tsai and M. Billone, "Characterization of High-Burnup PWR and BWR Rods", Presented at the Nuclear Safety Research Conference 2002, Washington, D. C., October, 28-30, 2002.

F-4.10 F. Groeschel et al, "Additional Post-Irradiation Characterization of Goesgen Rods," TR-105060 - Addendum, Sept. 1997

F-4.11 CRC Handbook of Chemistry and Physics, 65th Edition, CRC Press Inc. Boca Raton Florida, 1984, p. B-161.

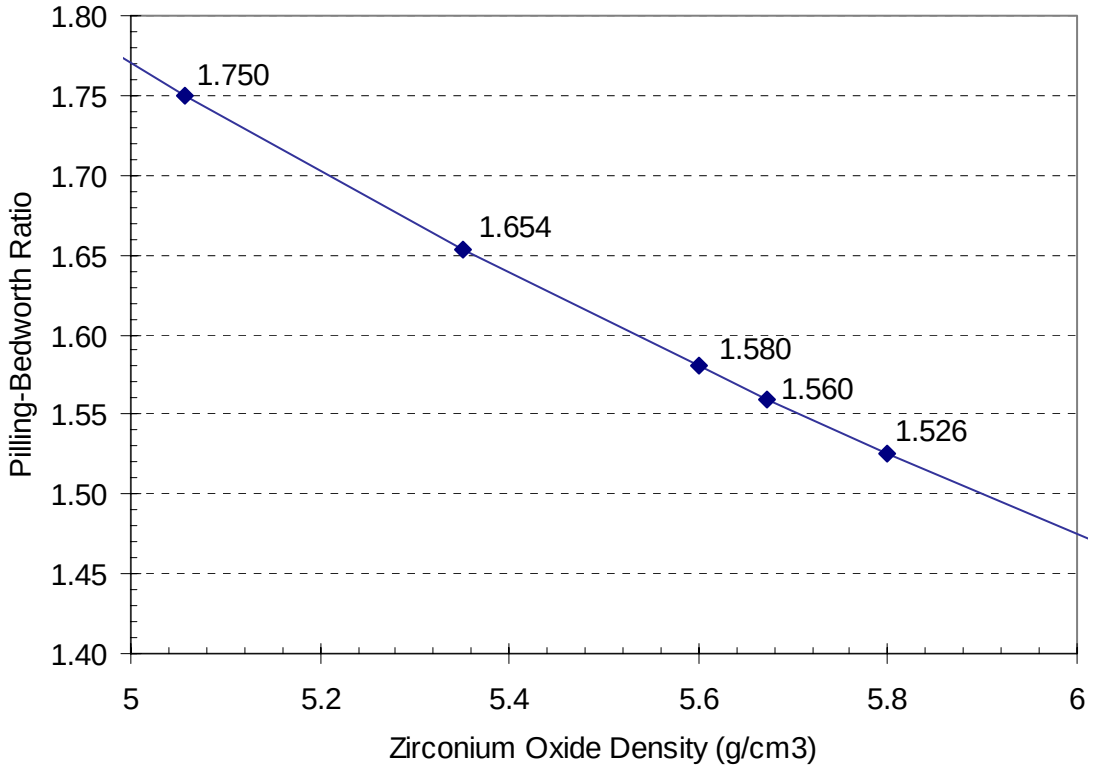

Figure F-4.1 Pilling-Bedworth ratio for zirconium oxide (ZrO_2) as a function of the ZrO_2 density from Equation F-4.3.

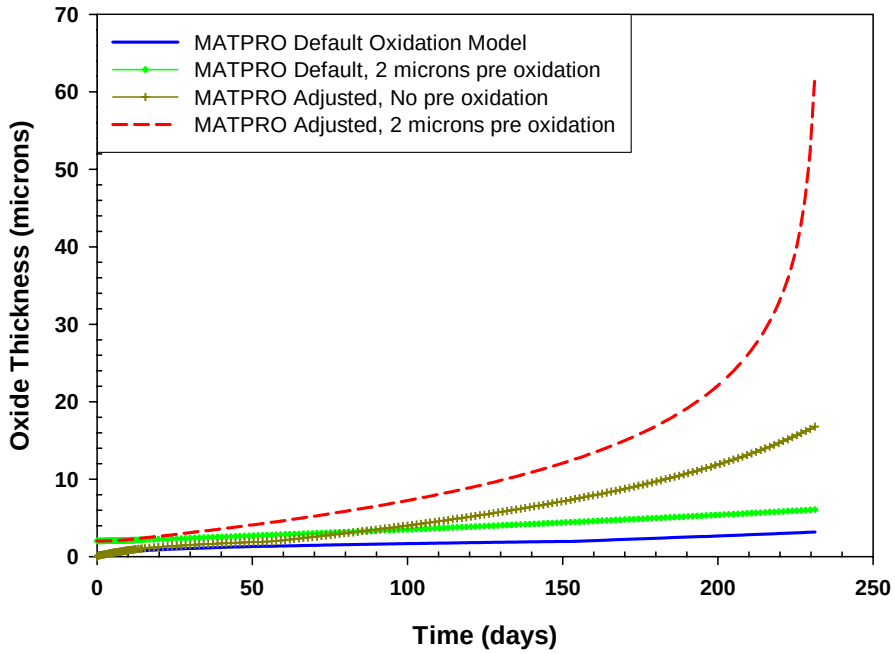

Figure F-4.2. Outer surface oxide layer thickness as a function of time during the irradiation of Test 856 (SE-33) in the ETR. Several variations of the MATPRO corrosion model for BWR conditions are shown for comparison.

Appendix F-4.A

Base Irradiation Analysis of the SPERT Test 859 GEX Fuel Rod With FALCON MOD01

1. Introduction

The SPERT-CDC test 859 was performed with a GEX (General Electric Experimental) fuel rod, pre irradiated to 31,800 MWd/tU, to determine the safe fuel enthalpy limit for irradiated fuel subject to a reactivity initiated accident. The GEX fuel rods were designed as a scaled-down version of standard BWR type fuel rods. These rods differ from conventional fuel rods in dimension and enrichment. The outer diameter of the Zr-2 cladding GEX fuel rod was reduced from the conventional 7x7 design of 0.563 in. to 0.3125 in., cladding thickness was reduced from 35 mils to 20 mils and the radial gap thickness from 4 mils to 2 mils. Enrichment of these rods was set at 7% - a compromise between power depression (35%) and attainable energy density in the CDC. These rods contain gas plenum spaces equaling about 11% of the fuel volumes.

The Engineering Test Reactor (ETR) at the National Reactor Testing Station was used for the base irradiation of the SPERT test rods. The ETR core consists of 3-in. by 3-in. square assemblies of fuel plates. The P-7 position in the ETR was a reflector position and was occupied by eight test fuel rods in a 3-level array. The fuel assembly was shielded within stainless steel and the P-7 system formed a complete pressurized water-cooling system. The irradiation was carried out in the loop with typical BWR thermodynamic and nuclear conditions, except for a slightly lowered fast-to-thermal flux ratio (between 0.15 and 0.2). The SE-33 fuel rod was charged into the reactor on May 14, 1969 and discharged on February 27, 1970 with an exposure of 182.3 effective days at a reactor power of 175 MW.

2. FALCON Analysis

The objective of the FALCON analysis of the SE-33 test rod base irradiation was to calculate the buildup of the outer surface corrosion layer and to estimate the outward cladding deformations caused by pellet-cladding mechanical interaction (PCMI) that may have occurred during the base irradiation in the ETR. These parameters establish the initial condition of the test rod prior to the reactivity accident test 859 in the CDC-SPERT facility. Because of the unique fuel rod design and the irradiation conditions in the ETR facility, we cannot rely on conventional experience to estimate the end of life corrosion characteristics of this rod. The smaller outer diameter combined with the high power levels require to achieve a burmup level of ~32 GWd/tU in less than 190 effective fuel power days resulted in high cladding surface heat fluxes. It is possible that these conditions combined with the metallurgical characteristics of the cladding material could have resulted in larger than expected cladding corrosion rates, especially at thick corrosion layers.

2.1 Model Development

The fuel rod dimensions for this analysis are mainly extracted from Reference F-4.A-1 and summarized in Table F-4.A-1. An axisymmetric r-z finite element grid was used to model the fuel column, cladding, gap, upper and lower plena, and upper and lower end caps. A total of five radial elements for the fuel column, one radial element for cladding and 20 axial elements were used to construct the FALCON model. Two-node gap elements were used to represent the fuel-cladding gap, and upper and lower plena.

Symmetry thermal and mechanical boundary conditions are used at the centerline of the fuel column and endcaps. The rod was filled with He with an initial pressure of 3 bars.

Table F-4.A-1: GEX fuel rod design parameters

Description	Value
Cladding outer diameter (inch)	0.3125
Cladding inner diameter (inch)	0.2725
Pellet outer diameter (inch)	0.268
Diametric gap (mils)	4.0
Enrichment (%)	7.0
Fuel density [% of T.D.]	94
Internal gas pressure [He] (bar)	3.0
Plenum volume (in^3)	7.5E-2
Active Fuel length (inch)	5.2
Lower Blanket Pellet Length (inch)	0.4
Upper Blanket Pellet Length (inch)	0.6
Blanket Pellet Enrichment (%)	0.7

2.2 Power Histories and Operating Conditions

A representative power history of the ETR reactor were developed and used in FALCON calculation. The rod was under irradiation for 216 days during which its average linear power was 13.9 kW/ft and its maximum linear power was 18.1 kW/ft. A hot-sport factor of 1.04 raised the linear power to 18.8 kW/ft over the mid section of the rod. The fuel rod received an average burnup of 31,800 MWd/tU. A combination of lower fuel enrichment (0.7%) and small axial power factors were used to model the top and bottom blanket fuel pellet regions.

Loop and reactor operating conditions during the irradiation are listed in Table F-4.A-2. The first analysis was performed using the bulk coolant temperature, pressure and mass flux. In this case, FALCON coolant channel enthalpy rise model calculate the cladding surface temperature based on the input flow conditions. The second analysis was performed with the estimated cladding surface temperature as input to eliminate any uncertainty in the flow conditions that might influence the cladding surface temperature calculations.

Table F-4.A-2: Loop and reactor operating conditions

Description	Value
Bulk Inlet Water Temperature, ^oF	*460*
Bulk Coolant ΔT, ^oF	*~ 10*
Coolant Pressure (psi)	*1000*
Coolant Mass Flux, (lb_m/ft^2-hr)	*1.8E+6*
Cladding Surface Temperature, ^oF	*550*

3. Discussion of Results

Figure F-4.A-1 shows FALCON calculated coolant and cladding surface temperatures. Water at a pressure of 1000 psi entered the P-7 loop with a temperature of about 237^{o}C and is calculated to exit the channel with about ~10^{o}C higher temperature. A similar temperature rise in the coolant channel was also observed in the experiment.

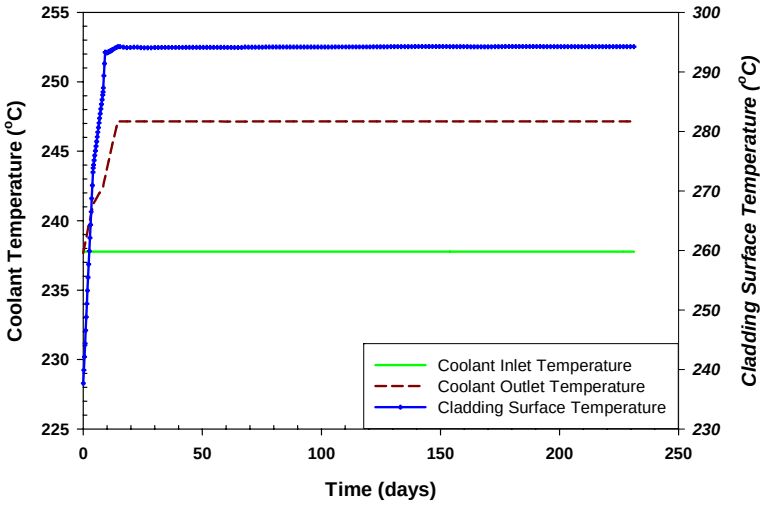

Figure F-4.A-1. FALCON calculation of coolant and cladding surface temperatures

FALCON includes the MATPRO cladding oxidation model, CORROS, [F-4.A-2] for BWR applications and this model was used to calculate the cladding oxidation during the irradiation. The oxide thickness calculated by FALCON using CORROS is shown in Figure F-4.A-2 for several different sets of initial conditions or model parameters. The default MATPRO oxide model calculates only about 4 microns of oxide at the end of the irradiation. Similar cladding oxidation was also obtained for the defined cladding surface temperature approach. However, the post-test hot cell measurements found the diameter increase of the rod to be about 127 microns due to the oxidation and cladding deformation [F-4.A-3]. FALCON calculates about 16 microns diametral deformation in the cladding, which strongly indicates that the oxide layer was the major contributor to the rod diameter increase. Experiments performed with BWR fuel rod cladding fabricated before 1980 reported a wide variation of cladding corrosion behavior for different surface treatments and surface conditions [F-4.A-4 and F-4.A-5]. As a result, several

different sensitivity calculations were performed to evaluate the impact of different initial conditions and model parameters on the end of life corrosion layer thickness.

In order to observe the impact of a pre-existing oxide layer on the in-reactor corrosion rate, the calculation was repeated assuming a 2 microns initial oxide thickness. In this case, FALCON calculates about 6 microns of oxide would form at the end of the base irradiation.

The under prediction by the default MATPRO oxidation model strongly indicates that the model is not calibrated for the high linear power operation over a relatively shorter period of time, which are the conditions of this irradiation. The oxidation enhancement factor used in the MATPRO low temperature oxidation model was derived from only a limited set of data and assigned to an average value of 9 for a BWR. Figure F-4.A-3 shows the data used to derive the enhancement factor for the MATPRO CORROS model. The original enhancement factor was developed using a lower bound value from the BWR data shown in F-4.A-3. A new hypothetical upper bound line has been drawn in Figure F-4.A-3, which indicates that this enchantment factor can be increased up to ~25 considering an upper bound fit to the data. Two sets of new FALCON calculations with and without a 2 micron pre-existing oxide layer were performed with an enhancement factor of 22 based on the new curve shown inF-4.A-3. The use of enhancement factors greater than 22 caused numerical problems in FALCON because of the asymptotic behavior of the corrosion rate. FALCON calculates about 17 microns of oxide for the fresh cladding model, whereas, for the 2 micron pre-existing oxide layer case the calculated maximum corrosion layer reached about 63 microns in the rod mid section. These results highlight the sensitivity of the corrosion layer build-up to the initial surface and metallurgical conditions.

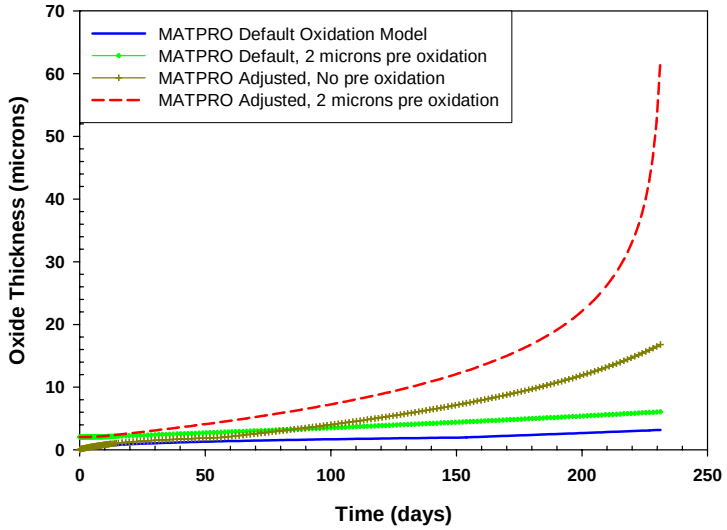

Figure F-4.A-2. FALCON calculation of cladding outer surface oxidation for rod SE-33 during the ETR base irradiation. Several variations of the MATPRO corrosion model for BWR conditions are shown for comparison.

The results contained in F-4.A-2 indicate that the high cladding heat flux combined with a corrosion layer of ~20 microns would have produced a condition of accelerated corrosion rate due to the feedback of the thermal resistance of the corrosion layer on the metal-oxide interface temperature. Since it was noted in visual examinations that rod SE-33 had a significant outer

surface corrosion layer (~65 microns), it would be expected that the higher burnup GEX rods irradiated in the ETR would have experience this accelerated corrosion rate. As shown in Figure F-4.2.A-2, the accelerated corrosion would have occurred sometime after 150 days of irradiation. The corrosion would easily have exceeded 50 microns at the end of life and most likely exceeded 100 microns, depending on the metallurgical and surface conditions of the cladding. As a consequence of this effect, high levels of corrosion would be expected only for the rods SE-33 (Test Rod 859) and SE-30 (Test Rod 756) because of their longer resistance time in the ETR (~182 EFPDs). Visual examinations of the lower burnup rods 684 and 685 (~13 GWd/tU) found no outer surface diameter changes from the base irradiation nor any notable outer corrosion features after 98 days of operation [F-4.1.A-1]. These visual examination results are consistent with the FALCON calculations with the modified CORROS model shown in Figure F-4.A-2, and based on the FALCON results, test rods 685 and 684 would have had less than 10 microns of outer surface corrosion.

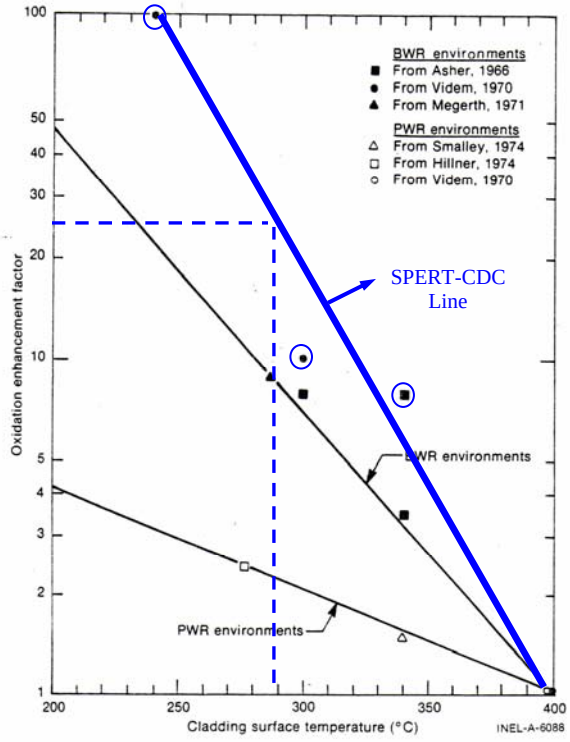

Figure F-4.A-3. MATPRO oxidation enhancement factor estimation for typical BWR and PWR environments

References:

F-4.A-1 R.W. Miller, 'The Effect of Burnup on Fuel Failure, Volume I: Power Burst Tests on Low Burnup UO_2 Fuel Rods', U. S. atomic energy commission scientific report, IN-ITR-113, July 1970.

F-4.A-2 "MATPRO - version 11: A handbook of materials properties for use in the analysis of light water reactor fuel rod behavior," NUREG/CR-0497 TREE-1280, February 1979.

F-4.A-3 R. W. Miller, 'The Effect of Burnup on Fuel Failure, Volume II: Power Burst Tests on Fuel Rods with 13,000 and 32,000 MWd/MTU Burnup', U. S. atomic energy commission scientific report, IN-ITR-118, April 1971.

F-4.A-4 F. Garzarolli, H. Stehle, E. Steinberg, and H. Weidinger, " Progress in the Knowledge of Nodular Corrosion," 7th International Symposium on Zirconium in the Nuclear Industry, June 24-27, 1985, Strasbourg, France, ASTM STP 939, pp. 417-430.

F-4.A-5 P. Rudling, and A. J. Machiels, " Corrosion Performance Ranking of Zircaloy-2 for BWR applications," 8th International Symposium on Zirconium in the Nuclear Industry, June 19-23, 1988, San Diego, California, ASTM STP 1023, pp. 315-333.

Response to Requests for Additional Information (RAI's)
NRR Safety Evaluation Report – Project No. 689

F-5. It is known that stress state has a significant impact on strain-to-failure and will also impact CSED. The mechanical test data presented are based on three stress states: hoop tensile (uniaxial ring tests), axial tensile and biaxial (burst tests). The EPRI CSED model development includes the ring (tensile) strain-to-failure data and appears to fit this data better than the burst or axial tension data. Based on round robin tests performed by Argonne National Laboratory, Commissariat a l'Energie Atomique, and the Russians it is known that the ring tensile tests are not a measure of material property in terms of strain-to-failure but instead ring test failure strains are a function of specimen size and test apparatus. The burst which are the most relevant to RIA and the axial tensile data appear to have lower strain energy densities (SEDs) at failure on average than the ring test data. This suggests that the proposed CSED correlation may seriously under predict the probability of failure leading to a non-conservative correlation.

Response to RAI F-5:

The database of mechanical property tests on irradiated cladding at high burnup is limited to only four experimental programs. Further, less than 120 mechanical property tests have been conducted with high fluence and high hydrogen content cladding material, including twenty-one (21) tests conducted at temperatures below 150°C and forty (40) ring tensile tests. These circumstances make it difficult to eliminate data that may contain some inaccuracies due to unique test specimen geometry or loading conditions.

The database of mechanical property tests includes ring tensile tests, axial tensile tests and biaxial burst tests. No individual dataset spans the range of temperature, hydrogen content, and oxide thickness necessary to appropriately describe the failure characteristics of irradiated Zircaloy cladding for application to RIA events. Because only a limited number of tests were available in any single test dataset, the entire database was combined together and used to develop a CSED model applicable to PCMI under RIA conditions. In combining the data together, two key factors must be considered: (1) the anisotropic mechanical behavior of Zircaloy cladding material and (2) differences in the stress state between the tests. For anisotropic mechanical behavior, it has been shown that the effects of irradiation eliminate or minimize the anisotropy in the mechanical response of Zircaloy cladding [F-5.1]. Therefore, combining mechanical property obtained from tests in the tangential and longitudinal directions is appropriate from a texture perspective. The ring tensile and axial tensile tests represent a uniaxial stress state in the tangential and longitudinal directions, respectively. The closed-end burst tests, on the other hand, represent a biaxial stress state with a longitudinal to tangential stress ratio of ~0.5 for these tests. In order to combine the results from the uniaxial ring and axial tensile tests with the biaxial burst tests results, a biaxiality correction factor was developed from experimental data on unirradiated, pre-hydrided Zircaloy material. The biaxiality correction factor was applied to the measured total elongation for both the uniaxial ring and axial tensile tests. The biaxiality correction factor ranges from 0.3 for low hydrogen samples to 0.15 for high hydrogen samples. By reducing the measured total elongation for the uniaxial tensile

tests, it becomes possible to combine the results from the uniaxial tensile tests and the biaxial burst tests into a single compatible dataset for model development.

A best-fit curve using an exponential form of the empirical equation was obtained from the combined database of CSED values calculated from the measured stress and strain parameters for each of the ring tensile tests, axial tensile tests and burst tests. Because the CSED model was obtained by a best-fit of the combined database, the model does not represent a best-fit curve to anyone of the individual datasets. To determine how the individual datasets influence the overall CSED best-fit model, the CSED model is compared to the best-fit curve developed for the non-spalled ring tensile tests and burst tests separately, in Figure F-5.1. At low oxide-to-cladding thickness ratios ($R_{ox} < 0.1$) , the ring tensile data influences the CSED model. At these ratios, the cladding material has a large amount of ductility ($\varepsilon_t > 3$ or 4 %). For higher R_{ox} values (> 0.1), the CSED model more closely follows the best-fit curve from the burst test CSED data.

The ring tensile test data used in the CSED model development are the only uniaxial mechanical property measurements in the tangential (hoop) direction. Since the primary loading under RIA conditions is in the hoop direction, these data were included as a means to obtain failure data applicable to deformations in the hoop direction. It is now recognized that artifacts of the sample geometry and loading mandrels influence the total elongation obtained from ring tensile tests. The impact of test artifacts on the total elongation has been primary observed on tests performed using unirradiated material that contain a large amount of ductility ($\varepsilon_t > 20\%$).

At the time of the original CSED model development, the influence of test artifacts on the ring tensile tests were not well known and the data were considered reliable. As mentioned above, a numerical best-fit to the CSED data from non-spalled burst tests was developed to evaluate the influence of including the ring data in the best-fit CSED model for non-spalled cladding. The results of this evaluation are summarized in Section 2.3.2.4 and 2.4.3 of the topical report. Figure F-5.2 shows a comparison of the curve from a best-fit to the burst CSED data and the curve from a best-fit to the entire CSED database, along with the CSED data obtained from the burst tests. As discussed above, the major difference between the two models is at low oxide thickness to cladding thickness ratios were the cladding ductility is the largest. Beyond an oxide to cladding thickness ration of 0.1, the two curves are very similar.

The validation of the CSED cladding integrity model is based on the analysis of the CABRI REP Na UO_2 test rods using FALCON. For the non-spalled CSED model, this includes REP Na-2, REP Na-3, REP Na-4, and REP Na-5. The FALCON transient fuel behavior code was used to calculate the SED accumulation during the PCMI phase of the power pulse for these experiments. For tests that survived the RIA experiment without cladding failure, the calculated SED value should be below the CSED curve. The potential for cladding failure increases once the PCMI loading causes the SED to increase above the CSED curve.

Shown in Figure F-5.3 is a comparison of the FALCON calculated SED values for the CABRI REP Na tests and the two different non-spalled CSED models, the best-fit to all the data (solid line) and the best-fit to the burst data only (dashed line). The SED results from FALCON reside below the best-fit curve to all the non-spalled CSED data, confirming that none of the test rods experience cladding failure. For the best-fit to the non-spalled burst test CSED data, the test

REP Na-2 resides above the curve indicating a high potential for cladding failure for this test. Similarly, REP Na-3 results from FALACON are just below the curve also indicating an increased potential for cladding failure. Neither of these tests exhibited any indication of cladding failure such as part-wall cladding cracks or localized plastic deformations in post-test metallographic examinations. These results confirm that the cladding failure boundary for RIA experiments resides above the CSED curve based only on the non-spalled burst tests. In support of this point, the non-failed MOX tests REP Na-6 and REP Na-9 further validate the use of the best-fit curve to all the CSED data. In these two tests, the Zircaloy cladding experienced residual hoop strains about twice that for the UO_2 fuel rods REP Na-2 and REP Na-3 [F-5.2]. Using the post-test strain measurements, the maximum SED experienced by the cladding during the power pulse can be estimated for the REP Na-9 and REP Na-6 and is approximately 45 MJ/m^3 and 28 MJ/m^3, respectively. The cladding oxide thickness to wall thickness ratios for REP Na-9 and REP Na-6 are 0.02 and 0.07, respectively. The REP Na-9 and REP Na-6 SED results reside slightly above the best-fit curve based on all the CSED data. The MOX test results further highlight that the actual cladding failure boundary for RIA conditions is above the best-fit CSED model based on using all the mechanical property data, including the ring tension data.

The validation of the CSED model using the FALCON analysis of the CABRI REP Na experiments indicate that the cladding failure boundary during RIA experiments is most appropriately represented by the best-fit curve to all the non-spalled CSED data for cladding with large amounts of ductility ($R_{ox} < 0.1$). For non-spalled cladding with low amounts of ductility ($R_{ox} > 0.1$), either curve is applicable for RIA experiments.

References

F-5.1. Murty, K. L. and S. T. Mahmood, "Effects of Recrystallization and Neutron Irradiation on Creep Anisotropy of Zircaloy Cladding," Zirconium in the Nuclear Industry: Ninth International Symposium, ASTM STP 1132, American Society for Testing and Materials, Philadelphia, Pennsylvania, 1991, pp. 198-217.

F-5.2. Cazalis, B, Papin, J., and Lemoine, F., "The MOX Fuel Tests in the CABRI REP-Na Programme: Analysis and Main Outcomes," *Proceedings of the ANS International Topical Meeting on Light Water Reactor Fuel Performance*, Park City, Utah, April 10-13, 2000.

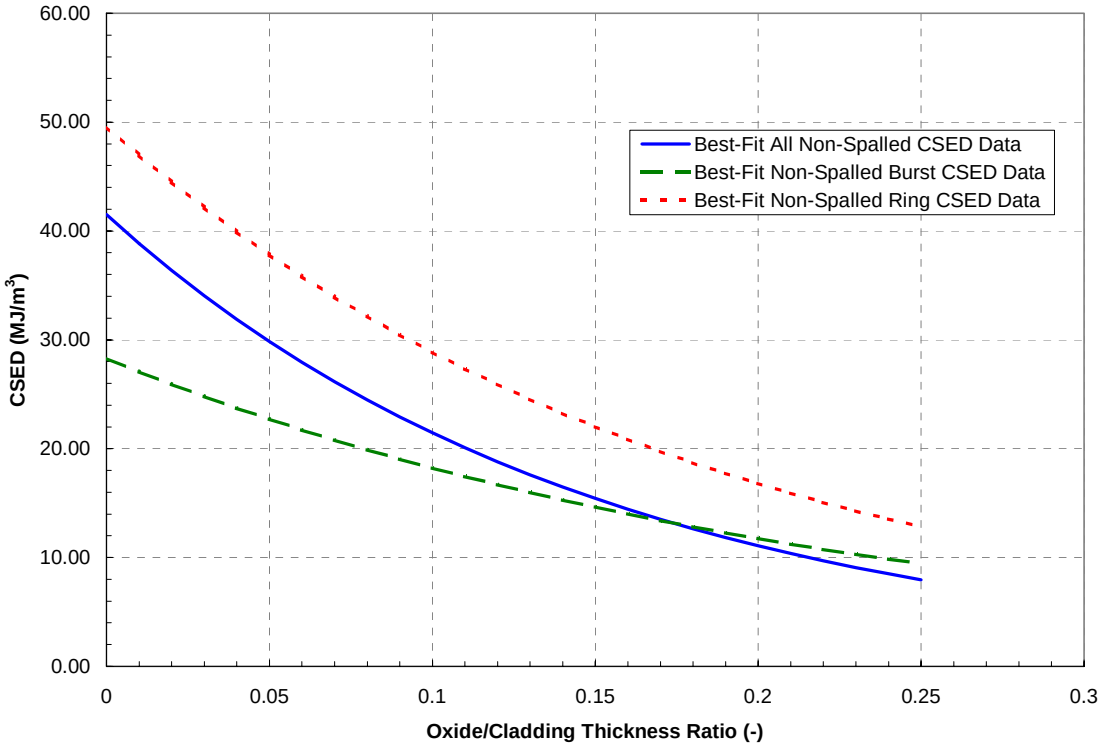

Figure F-5.1. Comparison of best-fit curves from numerical fits to the ring tensile tests, burst tests, and all the non-spalled mechanical property tests.

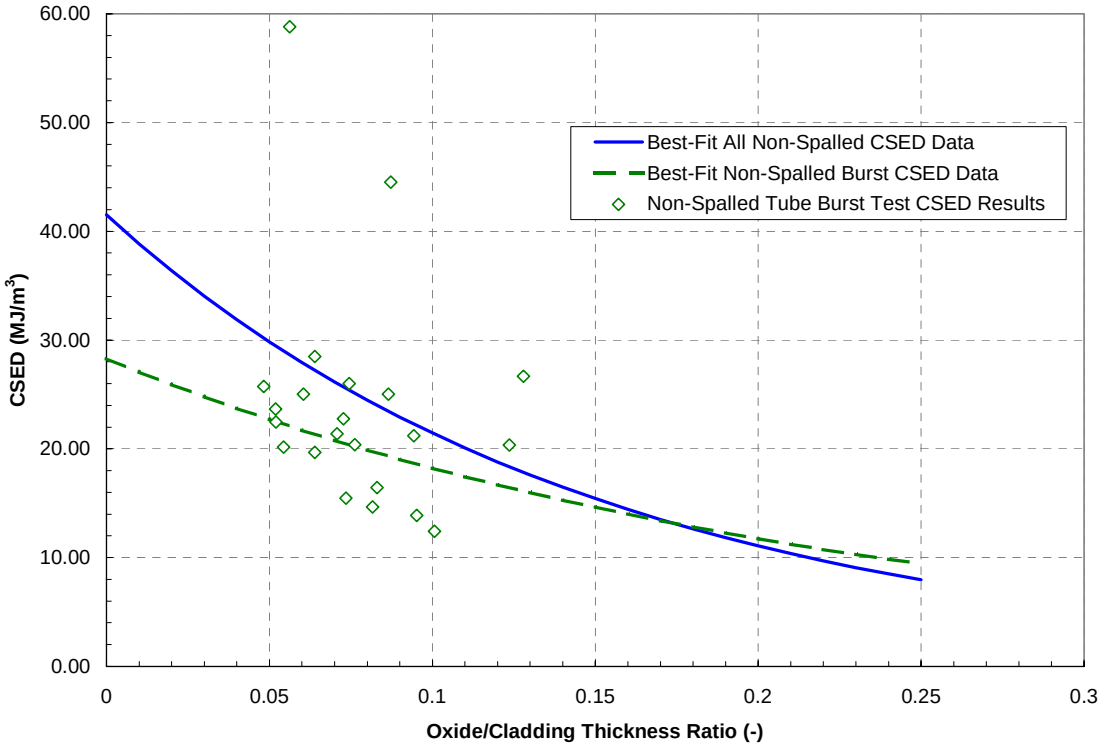

Figure F-5.2. Comparison of non-spalled tube burst test CSED data and best-fit curves

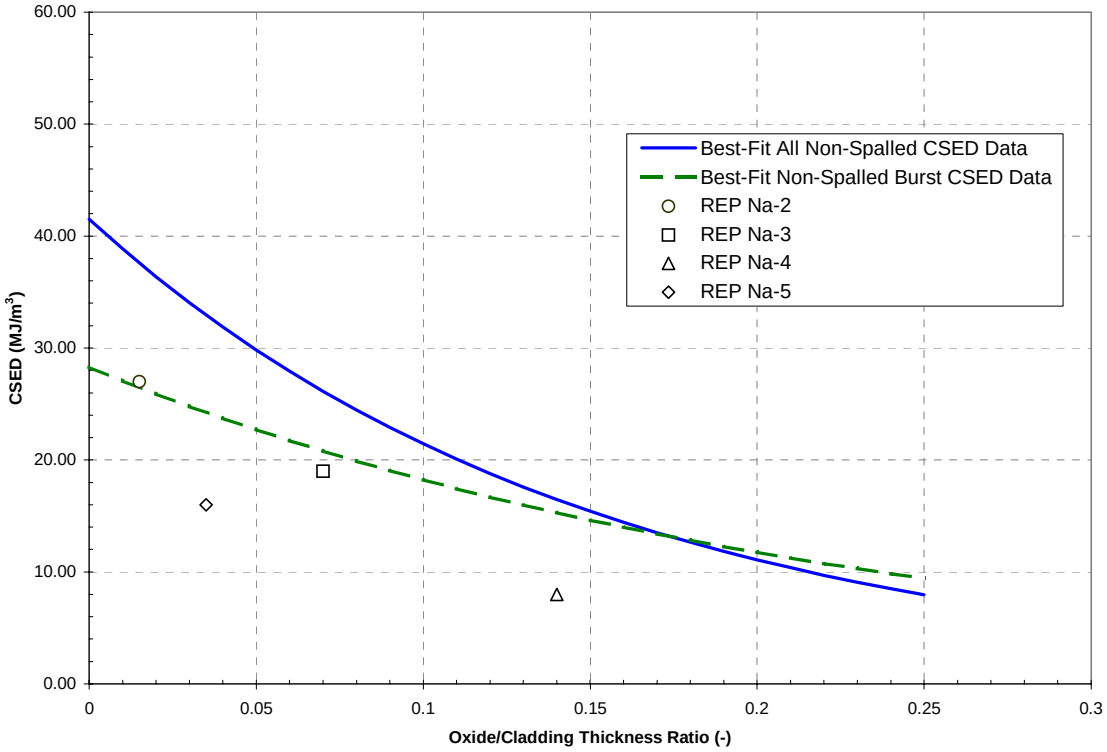

Figure F-5.3. Comparison of FALCON calculated SED with the CSED curve developed from a best-fit to the all the non-spalled CSED data and the CSED curve developed from a best-fit to only the non-spalled tube burst test data.

Response to Requests for Additional Information (RAI's)
NRR Safety Evaluation Report – Project No. 689

F-6. It appears that only PWR data are used to develop the CSED correlation as a function of oxide/cladding thickness ratio. However, the hydrogen pickup fraction is considerably higher for BWR cladding than for PWRs. Section 3.3.2 of the TR suggests that mechanical tests provided by Wisner and Adamson (1998) demonstrate that BWR Zircaloy-2 cladding will have equal or greater ductility than PWR Zircaloy-4 cladding. Examination of this reference appears to support this assertion up to a burnup of 45 GWD/MTU but does not support it above this burnup level. In addition, recent RIA tests performed on BWR rods in NSRR suggest that the BWR rod ductility drops significantly at burnups above 57 GWD/MTU and hydrogen levels above 150-200 parts-per-million. Therefore, the proposed limit provides non-conservative results.

Response to RAI F-6

Mechanical property tests on cladding from PWR fuel rods were used to develop the CSED correlation as a function of oxide-to-cladding thickness ratio because of the availability of the data and the emphasis on PWR rodlets in the CABRI and NSRR RIA-simulation tests. Two different CSED correlations were developed; one for temperatures above 280°C and one for temperatures below 150°C. The 280°C CSED correlation and the upper bound curve for the oxide thickness accumulation with burnup were used in the development of the proposed fuel rod failure threshold applicable to a lead rod average burnup of 75 GWd/MTU contained in the topical report.

While the hydrogen pickup fraction may be higher for BWR cladding as compared to PWR cladding, post-irradiation examinations find that the higher oxidation rate and the higher amount of oxide layer formation in PWR cladding produces considerably larger total hydrogen levels in PWR cladding. A comparison of hydrogen content measurements in irradiated PWR and BWR cladding is shown in Figure F-6.1 [F-6.1 and F-6.2]. It is clear from Figure F-6.1 that the combined oxidation rate and hydrogen pickup of PWR Zircaloy-4 cladding is an upper bound of BWR cladding throughout the entire burnup range.

The Wisner and Adamson [F-6.3] data referenced in Section 3.3.2 of the topical report were used to support the technical conclusion that the fuel rod failure threshold developed based on the 280°C CSED correlation and the bounding oxide thickness accumulation curve would be a lower bound for application to Hot-Zero Power (HZP) Control Rod Drop accidents (CRDA) in BWRs. This means that the PWR ductility data used to develop the CSED correlation is either representative of or a lower bound to BWR cladding. Since the publication of the topical report, additional data has become available through proprietary programs that continue to support the conclusions stated in the topical report [F-6.2, F-6.4]. A summary of the BWR cladding mechanical property data at temperatures above 250°C is shown as a function of hydrogen content in Figure F-6.2 and as a function of fast neutron fluence in Figure F-6.3. The BWR data includes material irradiated up to 65 GWd/MTU. Data from burst tests on irradiated PWR cladding without outer surface oxide spallation are shown for comparison. It can be seen that the total elongation from tube burst tests on PWR cladding is lower than the BWR data throughout

the entire fast fluence range up to 65 GWd/MTU. Based on this comparison, it can be concluded that Zircaloy-2 cladding material in BWR's has equal or higher ductility than Zircaloy-4 cladding material in PWR's at temperatures above 250°C and at equivalent burnup levels up to a lead rod average burnup level of 75 GWd/MTU.

The recent failures in the FK test series in NSRR were performed on test rods extracted from BWR fuel rods that were irradiated at powers less than 3 kW/ft during the last cycle of operation during which ~4 GWd/MTU was accumulated to reach 61 GWd/MTU [F-6.5 and F-6.6]. A schematic showing the fuel rod average power history and the assembly locations during the base irradiation is shown in Figure F-6.4 [F-6.2]. Such irradiation conditions can lead to deconditioning of the pellet-cladding gap, increasing the PCMI loads on the cladding during a subsequent power increase.

The coolant conditions for the FK tests were atmospheric pressure water at either a temperature of ~20°C or 80°C. The power pulses used in these tests had a full-width-half-maximum less than 6 milliseconds. Fuel rod analysis results find that only limited clad heating occurred at the time of cladding failure in these tests because of the rapid energy deposition. The cladding temperature at the time of cladding failure was below 50°C for the ambient temperature tests and less than 100°C for the heated coolant tests. These conditions combined with cladding hydrogen contents greater than 200 ppm and the presence of significant radial hydride fractions in the cladding outer region resulted in the cladding failure observed in the FK tests. Mechanical property tests have shown that the cladding ductility at low temperature levels may be lower than at elevated temperatures due to the impact of temperature on hydrogen solubility and material deformation mechanisms.

The effect of temperature on irradiated BWR cladding has recently been evaluated using Expansion Due to Contraction (EDC) tests performed by Studsvik [F-6.7]. A series of EDC tests were performed between 25°C and 300°C on intermediate (4-Cycle) and high (7-Cycle) burnup BWR cladding with hydrogen contents ranging between 60 ppm and 350 ppm. A summary of the EDC test results are shown in Figure F-6.5. These tests find that below a critical temperature, the cladding ductility is low due to the combined effects of irradiation and the presence of zirconium hydrides. Recovery of ductility occurs at temperatures above the critical temperature due to dissolution of zirconium hydrides and the increased ductility of both the Zircaloy-2 matrix material and the zirconium hydride platelets. The critical temperature ranged between 100°C and 200°C, depending on the fast neutron fluence and the hydrogen content. Similar results have been observed in the Wisner and Adamson data and the results reported in Reference F-6.4. A summary of total elongation as function of temperature from these tests can be found in Figure F-6.6

Because of the important role of temperature on the ductility of BWR cladding, the results of the FK tests in the NSRR reactor should not be used to evaluate the conservative aspects of the cladding failure threshold proposed in the topical report for BWR HZP CRDA conditions. The industry believes that the available mechanical property data supports our conclusion that the proposed failure threshold developed from PWR mechanical property data bounds the expected behavior of BWR fuel rods during a HZP CRDA up to a lead rod average burnup of 75 GWd/MTU.

References:

F-6.1 Mardon, J.P., Charquet, D., and Senevat, J., "Influence of Composition and Fabrication Process on Out-of-Pile and In-Pile Properties of M5 Alloy," Zirconium in the Nuclear Industry: Twelfth International Symposium, ASTM STP 1345, G. P. Sabol and G. D. Moan, Eds., American Society for Testing and Materials, West Conshohocken, PA, 2000, pp. 505-524.

F-6.2 Hayashi, H., et. Al., "Outside-in Failure of High Burnup BWR Segment Rods Caused by Power Ramps Tests," Proceedings of the ENS TOPFUEL 2003 Conference, March 2003.

F-6.3 Wisner S.B. and Adamson R.B., "Combined effects of radiation damage and hydrides on the ductility of Zircaloy-2," Nuclear Engineering and Design, 185, 1998, pp. 33-49.

F-6.4 Nakatsuka, M. and Ogata, K, "Cladding Transient Response: Rapid Burst Tests on Unirradiated and Irradiated Zircaloy Samples," EPRI, Palo Alto, CA: 2004, 1003045.

F-6.5 Nakamura, T., et. al., "High Burnup Fuel Behavior Under Simulated Reactivity Initiated Accident Conditions," Nuclear Technology, Vol. 138, June 2002.

F-6.6 Nakamura, T., et. al., "Failure Thresholds of High Burnup BWR Fuel Rods under RIA Conditions," Journal of Nuclear Science and Technology, Vol. 41, No. 1, p. 37–43, January 2004.

F-6.6 Grigoriev, et. al., "Temperature Effect on BWR Cladding Failure Under Mechanically Simulated RIA Conditions," Presented at the Fuel Safety Research Specialists Meeting, March 2004, Tokyo, Japan.

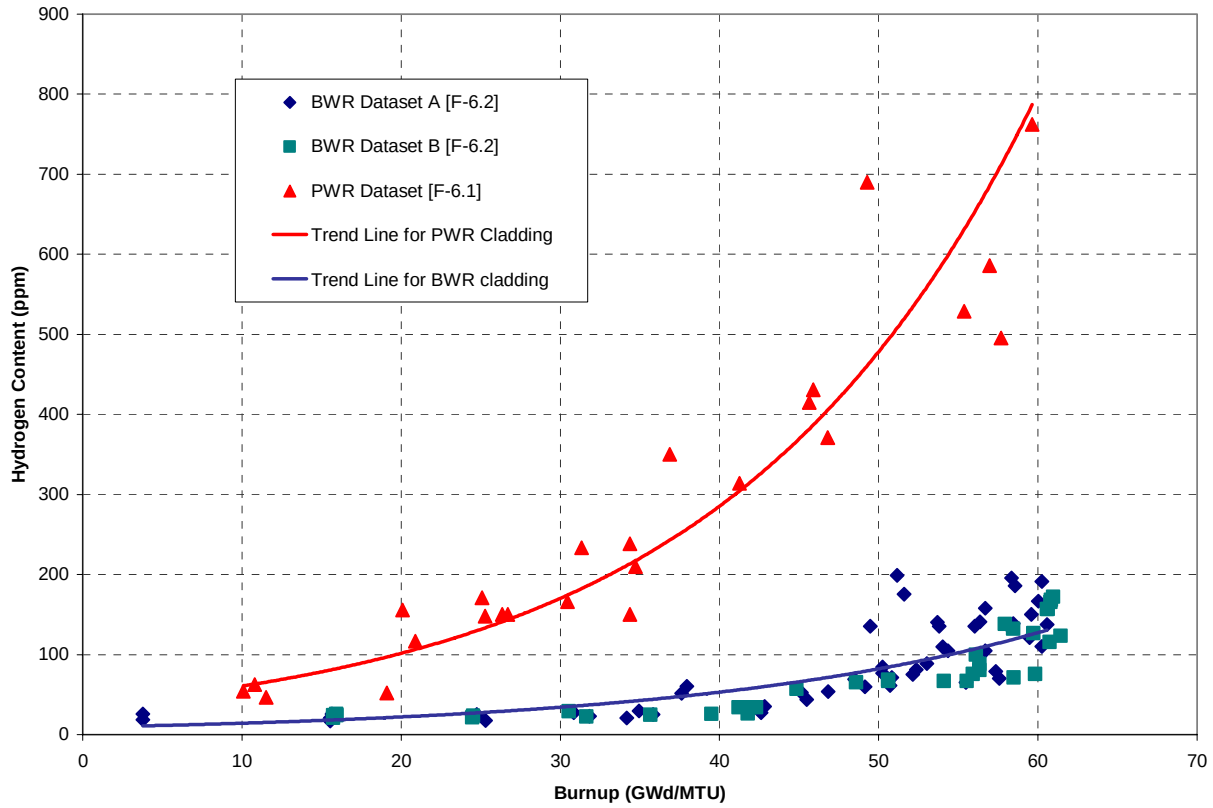

Figure 6-4.1 Hydrogen content as a function of fuel rod burnup for both PWR and BWR cladding material

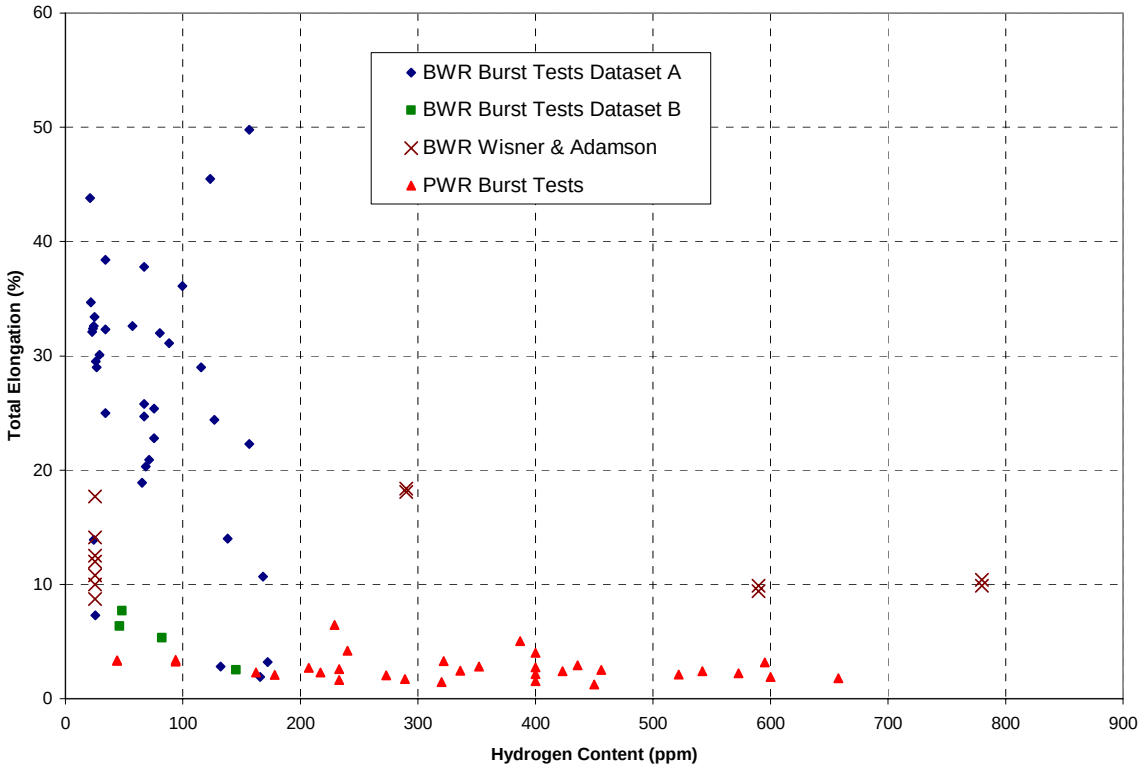

Figure 6-4.2 Total elongation as a function of hydrogen content for both BWR and PWR cladding from mechanical property tests at temperatures greater than 250°C

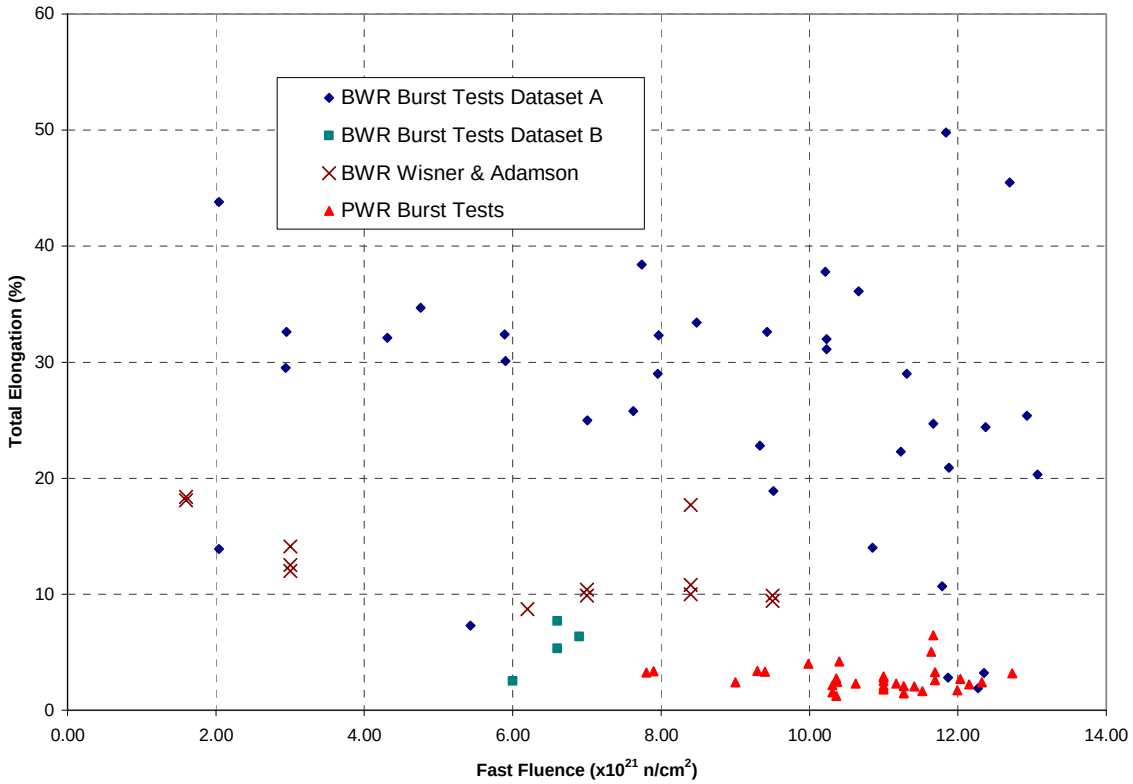

Figure F-6.3 Total Elongation as function of fast neutron fluence for both BWR and PWR cladding from mechanical property tests at temperatures greater than 250°C.

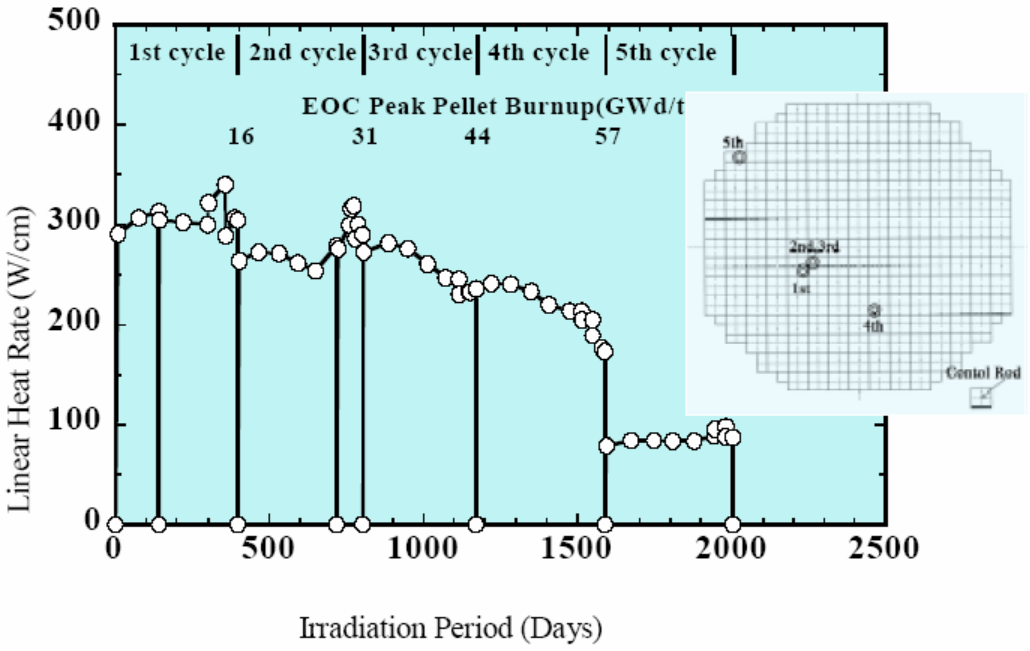

Figure F-6.4. Base irradiation power history for the fuel rods used in the NSRR FK tests

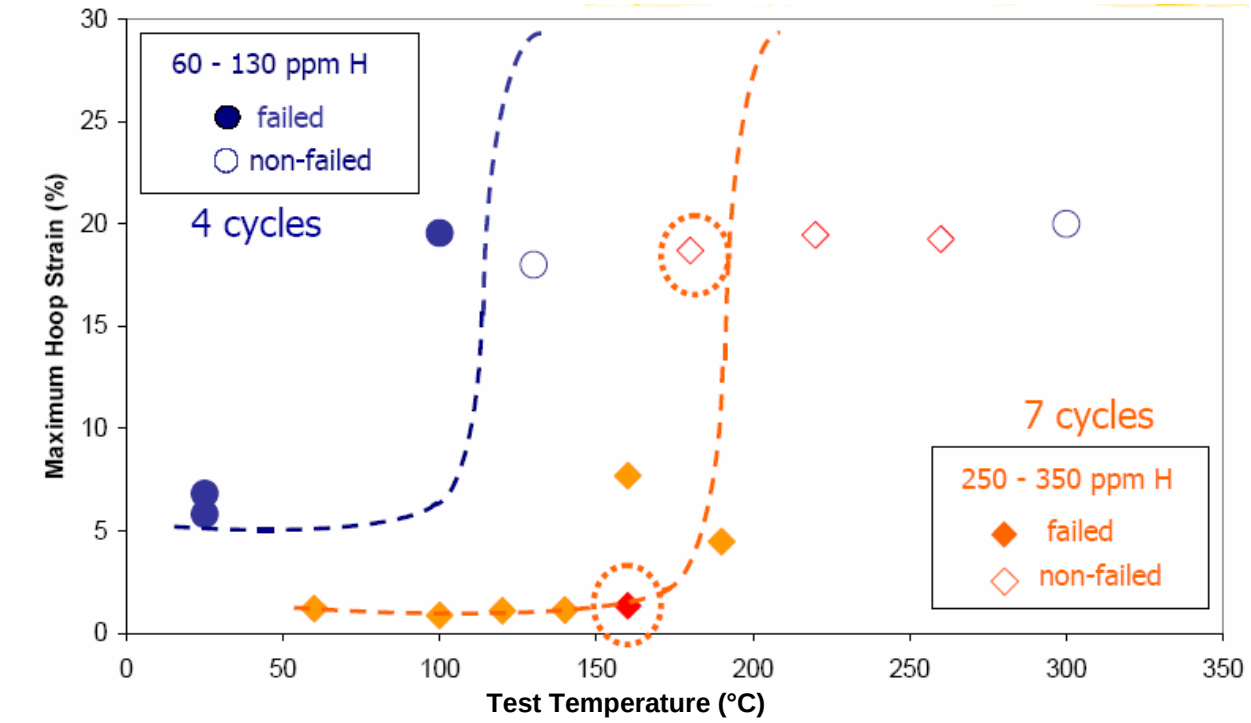

Figure F-6.5 Maximum hoop strain as a function of temperature from EDC tests performed on irradiated BWR cladding.

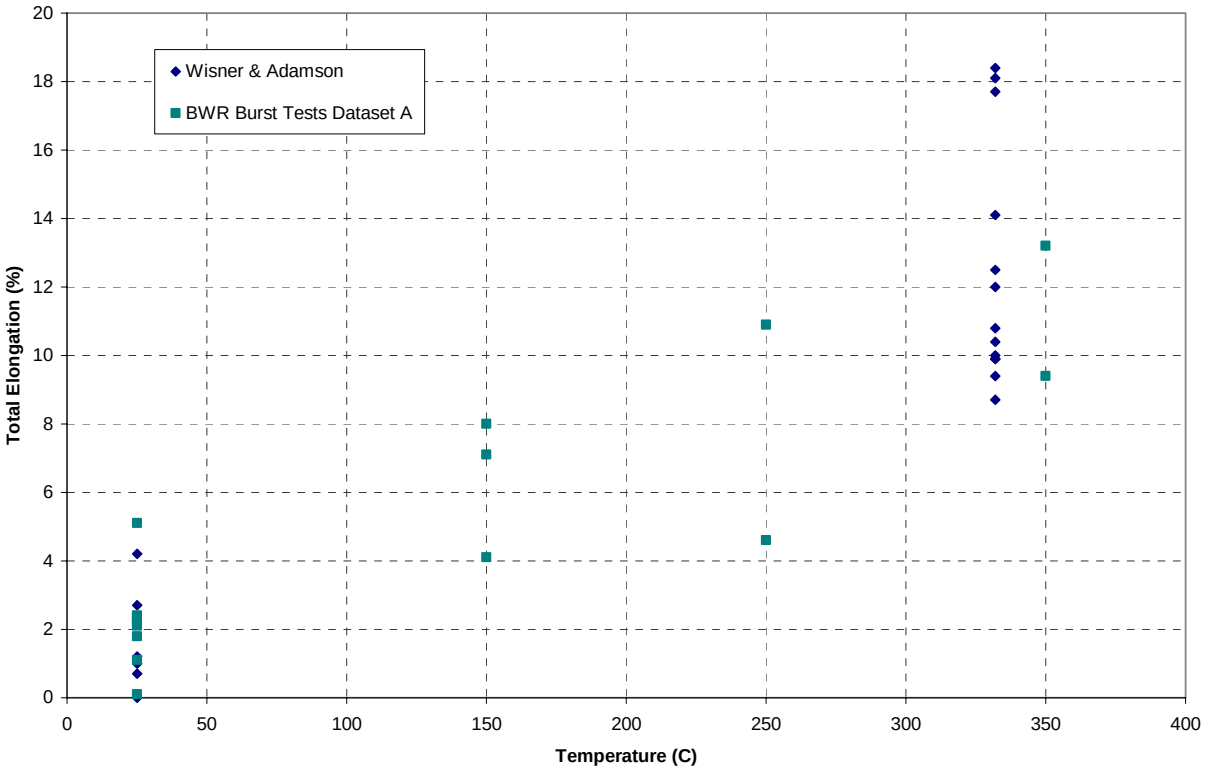

Figure F-6.6 Total elongation as a function of temperature for tests performed on irradiated BWR cladding.

F-7. The argument is made that the SED/CSED model is derived directly from the J-integral methodology used for fracture mechanics analysis. This argument may be challenged by many fracture mechanics experts; however, there is no argument with regard to the application of J-integral fracture toughness with respect to the American Society for Testing and Materials (ASTM standards for determining fracture toughness. A specific test method is specified for determining the J-integral values as stated in ASTM 813 and ASTM 1820 and this ASTM test method is not the same as the test measurement methods used to develop the SED/CSED methodology.

Furthermore, ASTM 1820 states that J-integral test should not be applied to brittle materials. Zircaloy uniform elongation strains of less than 1.0 to 1.5 percent strain (applicable to high burnup cladding) with a high hydrogen content appear to display significant brittle behavior. This suggests that the use of SED/CSED may not be applicable to high burnup cladding. This lack of applicability for the J-integral tests is further demonstrated by examining the available open literature J-integral data from irradiated Zircaloy with high hydrogen content. A plot of the J-integral data from Zircaloy versus hydrogen content does not show a discernable dependence, while a plot of the plane strain fracture toughness (K_{IC}) demonstrates a definitive dependence with a significant decrease in K_{IC} with increasing hydrogen content, which is expected due to hydrogen embrittlement. This suggest that the J-integral method may not be applicable in determining hydrogen embrittlement in high burnup Zircaloy.

There are three main points raised in the above review statement: (1) Comments on the RIA Report's section on the relationship between *SED* and the *J-Integral* for cladding tube under PCMI loading; (2) the application of the ASTM 1820 standard to high-burnup cladding; and (3) the comparison of *J-Integral* vs. hydrogen data with K_{IC} vs. hydrogen data and the conclusions drawn there from.

Point (1) requires detailed theoretical discussion, which is outside the scope of this response and will be addressed elsewhere in the appropriate forum[1]. However, Points (2) and (3), using fracture-testing arguments, seem to imply that high-burnup cladding may be too brittle to be judged by the SED/CSED methodology. Specific responses to these two points will be given here, but first we present a statement of general response.

GENERAL RESPONSE

Cladding material generally sustains some loss of ductility with burnup; however, we do not classify high-burnup cladding as a brittle material in a fracture mechanics sense, but the SED/CSED approach is valid regardless of whether the material is brittle or ductile. Equivalence between the SED/CSED approach and the *J-integral* is incidental and is not necessary to support our argument. It unfortunately has diverted the discussion away from the real issue, namely,

[1] A paper on this general topic is currently under preparation for publication.

how to develop an experimentally validated cladding failure criterion that is analytically compatible with the state of the art of fuel rod transient analysis.

The reviewer seems to view the SED/CSED RIA methodology from a fracture-toughness-testing perspective, whereas we view the problem from the broader perspective of the "mechanics of fracture" of fuel rod cladding subjected to the RIA phenomenon. The issue boils down to finding a resolution to the following question: Given the analytical and experimental state of the art, how can one predict the failure of high burnup cladding subjected to PCMI loading? The response to this question consists of the following three elements: (a) knowledge of the cladding initial physical condition from which failure could initiate, such as a defect, an incipient crack, an operationally induced flaw or a localized damage resulting from high burnup effects; (b) a fuel behavior computer code capable of detailed modeling of fuel rod behavior under the expected conditions; and (c) a failure criterion that expresses the failure measures in terms of response variables that can be computed in the fuel behavior code. These are discussed individually below.

With respect to the first element, the damage form is totally unknown and is beyond the analyst's grasp, but one can assume that after long service in the reactor environment some sort of surface damage, superimposed on hydride- and irradiation-induced distributed damage, would be present. The damage could be in the form of small flaws, oriented in the R-θ plane, caused by chemical or fission product attack at the pellet-cladding interface or a shallow crack in the hydride rim region at the OD. Whatever the geometry of this damage may be, it cannot be defined to permit a direct cause-and-effect analysis.

With regards to the analysis tool, the analytical state of the art consists of a full-2D finite-element based codes, such as FALCON, and axial-stacking-1D codes, such as FRAPTRAN and SCANAIR. These codes, each within its own capabilities, compute axi-symmetric stresses and strains in the R-Z plane, which do not vary azimuthally. This means that, even if one has full knowledge of the flaw geometry, flaws oriented in the R-θ plane cannot be modeled in an axi-symmetric R-Z analysis, and a direct numerical evaluation of their effect on cladding failure will remain elusive for these codes[2].

Because of the above-described analytical and practical constraints, failure criteria that specifically depend on the geometry of the flaw, e.g. fracture toughness, would not be useful. Note that fracture toughness is not an available option as a failure criterion for two reasons: firstly, inability to calculate stress intensity factor, as already mentioned, to be compared to a fracture toughness criterion; secondly, neither fracture toughness data, nor ASTM testing standards, exist for radial-axial fracture in thin tubes.

Clearly, then, if as a consequence of high-burnup operation localized damage in the form of shallow flaws exists, as most observers would agree that it does to a finite probability, failure prediction can be achieved only by the development of failure criteria and analysis methods that can recognize the presence of flaws but without specifically modeling the flaws. This, we have shown, has been achieved through the FALCON-SED/CSED methodology.

[2] An exception may be made for the FALCON code, which can specifically model a flaw in the r-θ plane. However, such modeling was not attempted for the reasons cited in this document.

The SED/CSED methodology combines axi-symmetric computations, which are far field with respect to radial-axial flaws in the R-θ plane, with material tests in various orientations, in a way that establishes a cause-and-effect linkage between the global and local conditions at failure. Detailed three-dimensional finite-element modeling would show that failures emanating from a small imperfection-type or hydride-related flaws involve local stress-strain fields that are three-dimensional, although the applied loading may be biaxial or even uni-axial. This condition applies in both systems, a fuel rod cladding subjected to a PCMI loading in an RIA transient, or a material property test in the laboratory. However, while the far-field stresses and strains are not compatible on a component-by-component basis between the two systems, the total energy is fully compatible, being the scalar sum of all components. Thus, by comparing scalar quantities, namely SED in the RIA transient and CSED from stress-strain tests, both representing similar material conditions, one in effect says that the mechanical energy required to initiate failure from a damage form is an invariant property of the material condition that gave rise to the damage form. This statement is valid for the SED/CSED methodology under radial loading regimes, which include PCMI in a fuel rod, pressurized tube tests, and mandrel-loaded or Poisson-loaded (insert-loaded) ring tension tests. Combining the strain energy contributions from radial-loading tests with non-radial loading tests, such as axial tension and standard ring tension tests, in the CSED database is justified on the basis that the best-estimate correlation of the sum of all the energies from the different tests is a more valid representation of the three-dimensional stress-strain field in the fuel rod than any single test. This has been validated by comparing the SED calculated at failure in RIA tests to the best-fit curve of the CSED database.

SPECIFIC RESPONSE

Application of the ASTM 1820 standard: The review comment, *"ASTM 1820 states that J-integral test should not be applied to brittle materials"*, appears to refer to paragraph 7.4 of the standard, which reads: *"However, there are some materials that are too brittle to be fatigue-cracked since they fracture as soon as the fatigue crack initiates; these are outside the scope of the present test method"*. Fuel rod cladding geometry, regardless of whether it is ductile or brittle, is outside the scope of the ASTM 1820 standard. Nevertheless, this ASTM-1820 analogy seems to place high burnup cladding in a behavior category that belongs to such brittle materials as glass and ceramics. We disagree with this analogy and the assessment of high-burnup cladding ductility. Such characterization of cladding ductility is totally at odds with the material-properties literature, which unambiguously shows that high-burnup cladding retains sufficient ductility at reactor operating conditions, including RIA transients. Furthermore, the literature shows *J-Integral* data for BWR cladding with hydrogen concentrations in the range of 700-900 ppm, which, while exhibiting "brittle fracture"[3] at room temperature, showed ductile behavior at 300°C, (see Grigoriev et. al., ASTM STP-1295, 1996, pp. 435-447)[4].

The SED/CSED methodology is valid regardless of whether the material is brittle or ductile. However, the reviewer has concluded, based on ASTM 1820 that the SED/CSED methodology

[3] The term "brittle fracture" is used here in a fracture-mechanics sense to mean elastic fracture, which is fracture under conditions of small-scale yielding, not to mean brittle material in the sense of glassy material behavior.
[4] Grigoriev's tests, which were for axially notched (not fatigue cracked) cladding tube specimens, did not conform to the 1820 standard.

would not be applicable to high-burnup cladding. This, however, seems to be a circular argument since, in asserting that by the ASTM 1820 *J-Integral* testing rules the SED/CSED methodology is inapplicable to high-burnup cladding, the reviewer is in effect relying on the equivalence between *J-Integral* and *SED/CSED*, which he had previously argued against. The reviewer further emphasizes his point by introducing some data trends relating *J-Integral* and K_{IC} values to hydrogen concentration, which is discussed in the next section.

***J-Integral*-Hydrogen data vs. K_{IC} -Hydrogen data:**

It was suggested in the review comment, based on the above ASTM 1820 analogy, that the SED/CSED methodology may not be applicable to high-burnup cladding. The comment goes on to say,

> *"This lack of applicability for the J-integral tests is further demonstrated by examining the available open literature J-integral data from irradiated Zircaloy with high hydrogen content. A plot of the J-integral data from Zircaloy versus hydrogen content does not show a discernable dependence, while a plot of the plane strain fracture toughness (K_{IC}) demonstrates a definitive dependence with a significant decrease in K_{IC} with increasing hydrogen content, which is expected due to hydrogen embrittlement"*.

The plots referred to in the review comment have not been provided by the reviewer to allow us to respond in a more informative way. However, relying on guesswork, we suspect that the reviewer is referring to two articles, a recent paper by *Bertolino et. al*. in the *Journal of Nuclear Materials 320, (2003) 272-279*, which contains the data for *J-Integral* vs. hydrogen content; and an earlier paper by *Kreyns et. al., ASTM STP 1295, 1996, pp. 758-782*, which contains the K_{IC}-hydrogen data.

Before commenting on Bertolino et. al. data, we refer the reviewer to two articles: Grigoriev et. al. (*ASTM STP 1295, 1996, pp.435-447*, Figure 8), and Edsinger et. al. (*ASTM STP 1354, 2000, pp. 316-339*, Figure 9), which show a clear trend of hydrogen dependency in their fracture initiation data. Both Grigoiev and Edsinger used BWR cladding specimens, while Bertolino used ASTM 1820 Zr-4 specimens. One should not ignore the Grigoriev and Edsinger results simply because they used non-ASTM specimens. One may argue that Grigoriev's and Edsinger's results may be influenced by the effect of Zr-2 texture on hydride morphology, but their results nevertheless belong to the present discussion.

As already noted, the Bertolino et. al. data is stable-crack-extension data generated in accordance with the ASTM 1820 Standard, and had the authors included in their paper crack initiation data explicitly, a discernable dependence on hydrogen would have been observed. In fact, upon closer examination of the Bertolino data, one can discern in Figure 7a, at $\Delta a \approx 0$, sensitivity to hydrogen. This figure is reproduced here for easy reference. The lack of sensitivity to hydrogen in the stable crack growth stage could be due to any number of reasons, not the least of which is the effect of hydride morphology, which may change during the test as the result of unloading and reloading procedure dictated by the testing method. In a sense, one might say that for this reason alone the test disqualifies itself for hydrided material. This is over and above the fact that Bertolino's "fracture toughness" values do not apply to cladding geometry or behavior under the conditions we are discussing.

The Kreyns et. al. paper presents no particular controversy that is relevant to the present discussion. However, one might point out that the data is for beta-quenched material, which could introduce a texture effect, both in the magnitude and the trend, which may require interpretation with respect to cold-worked stress-relieved Zr-4 cladding.

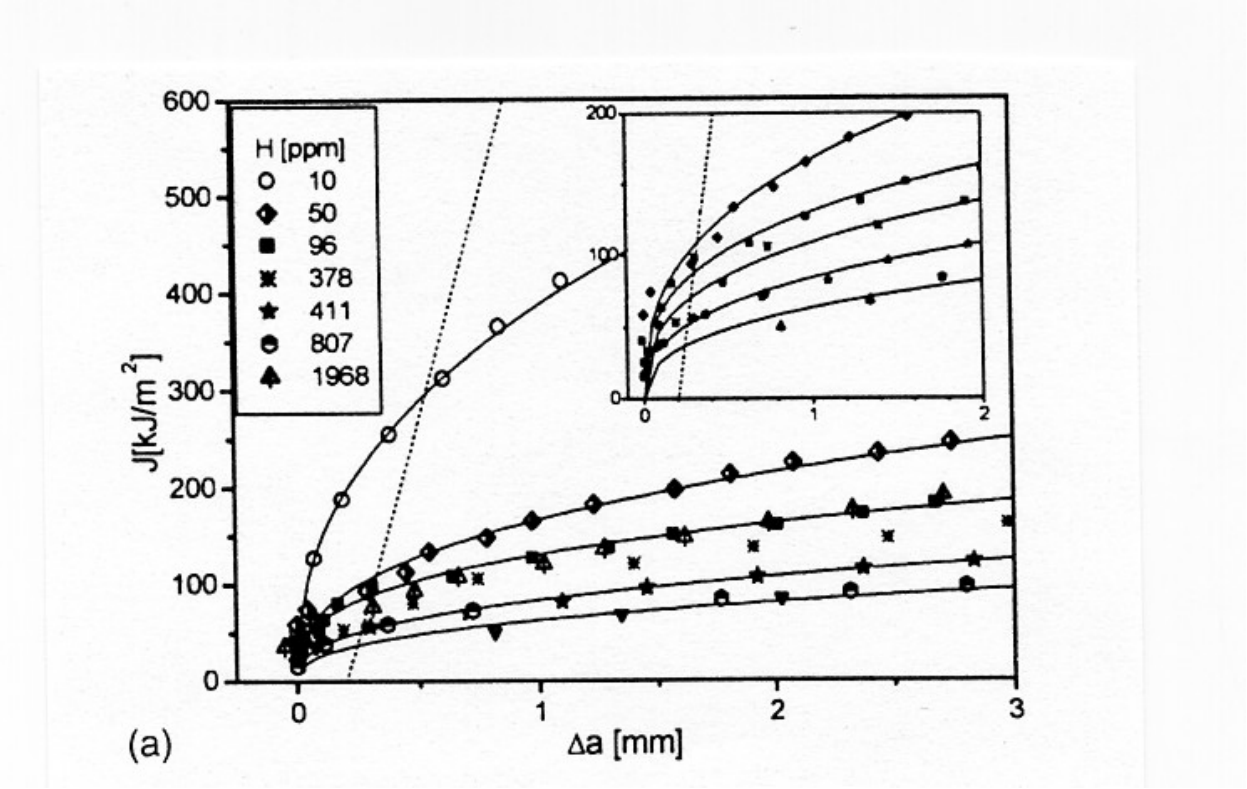

J-R Results at room Temperature for different H content. (Figure 7a from *Bertolino et. al*. in the *Journal of Nuclear Materials 320, (2003) 272-279*)

Response to Requests for Additional Information (RAI's)
NRR Safety Evaluation Report – Project No. 689

F-8. The staff attempted to duplicate the SEDs calculated with FALCON by programming Equation 2-14 into the FRAPTRAN code and applying the same methodology. The studies performed with FRAPTRAN were unable to duplicate the SED values for those CABRI and NSRR test rods with plastic strains at or above 1 percent. This indicates that the SED values may be code dependent.

Response to RAI F-8

The strain energy density formula given by Equation 2-14 in the Topical Report depends on the evolution of the cladding hoop and axial stress and strain calculated by the fuel performance code. Provided the cladding hoop and axial stress and strain calculated by different fuel performance codes are similar, the SED calculated using Equation 2-14 should also be similar between the different codes. As an example, a comparison of calculated cladding strain and SED results for the CABRI tests on UO_2 fuel has been developed for the SCANAIR and FALCON transient fuel performance codes. Electricitie de France (EdF) provided the SCANAIR results for this comparison. The predicted versus measured maximum residual cladding hoop strain is shown in Figure F-8.1 for both FALCON and SCANAIR. The results from the two codes are almost identical up to about 1.3% calculated residual hoop strain. Furthermore, the results agree well with the post-test measurements as evidenced by the fact the symbols are near the perfect agreement line in Figure F-8.1. For REP Na-2, some difference in residual cladding hoop strain calculated by FALCON and SCANAIR is noted because the SCANAIR gaseous swelling model produces much higher pellet expansion as compared to FALCON. The FALCON result for REP Na-2 is much closer the measured data as shown in Figure F-8.1.

A comparison of the calculated SED values from SCANAIR and FALCON is shown in Figure F-8.2. It should be noted that the failed UO_2 rods REP Na-8 and REP Na-10 have been added to the SED plot. The SED calculated by FALCON agrees very well with the SCANAIR results for all the CABRI experiments except for REP Na-2. For this case, the SED calculated by SCANAIR is ~2.3 times the value from FALCON. However, this is consistent with the large difference in the cladding hoop strain calculated by the two codes. SCANAIR calculated a residual cladding hoop strain that is ~2.8 times the value from FALCON. These results highlight the fact that the SED is code independent as long as the calculated conditions are similar between the two codes.

Only limited results for cladding residual hoop strain are available from FRAPTRAN to compare with the FALCON results [F-8.1]. No results for the FRAPTRAN calculated SED values were available. A comparison of the FRAPTRAN results with the FALCON and SCANAIR calculations is shown in Figure F-8.3 for the residual hoop strain. For residual cladding hoop strains up to 1%, good agreement is seen between all three codes. The FRAPTRAN results for REP Na-2 with a measured strain of ~3% is well below both the FALCON and SCANAIR values. The residual cladding hoop strain calculated by FALCON is the closest to the post-test measurements. It would be expected that the SED for the CABRI tests up to 1% strain would

agree well between FALCON and FRAPTRAN unless the Zircaloy-4 stress-strain constitutive models in the two codes are considerably different.

For the FALCON and SCANAIR codes that have been well validated against RIA experiments, good agreement is observed between both the residual cladding hoop strain and the SED values. The inability of FRAPTRAN to reproduce the SED's from FALCON may be related to the limited amount of validation for this code. Additional information from the FRAPTRAN results for the CABRI and NSRR experiments are required before this issue can be fully resolved.

References:

F-8.1 Geelhood, K,J., Beyer, C.E., and Cunningham, M.E., "Modifications to FRAPTRAN to Predict Fuel Rod Failures Due to PCMI during RIA-Type Accidents," Proceedings of the 2004 International Meeting on LWR Fuel Performance, Orlando, Florida, September 19-22, 2004.

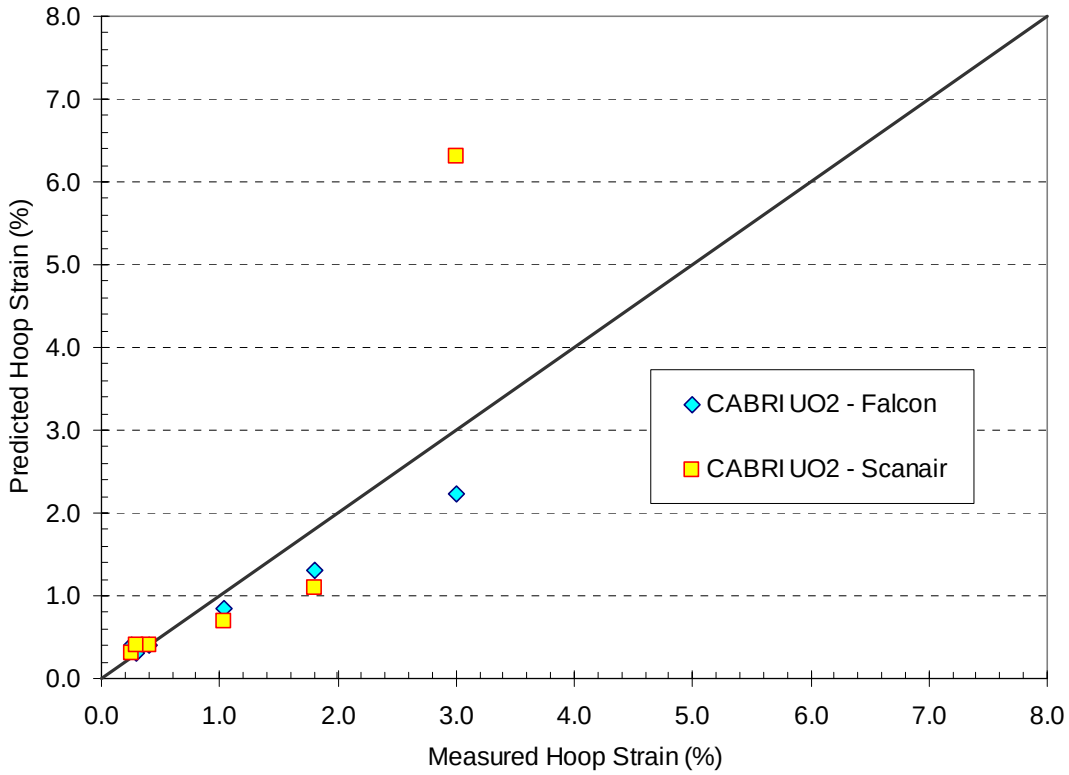

Figure F-8.1. Predicted versus Measured Cladding Residual Hoop Strain for FALCON and SCANAIR

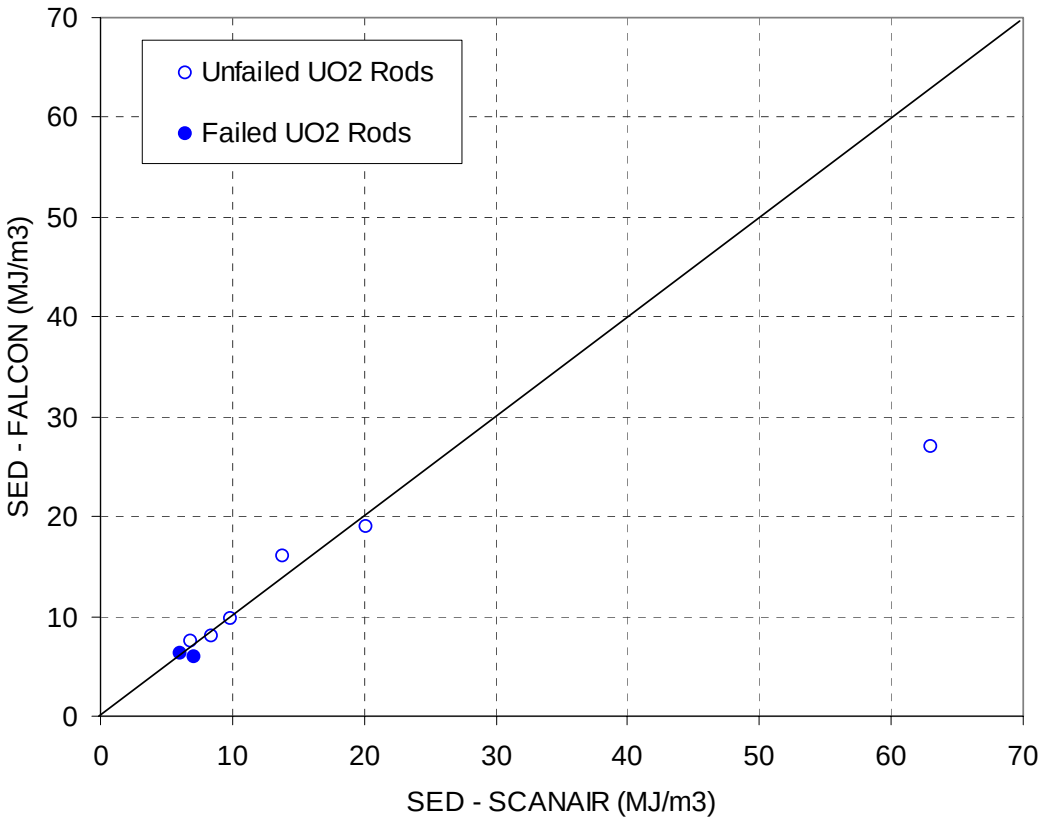

Figure F-8.2. Comparison of the Calculated SED values from FALCON and SCANAIR for the CABRI Tests

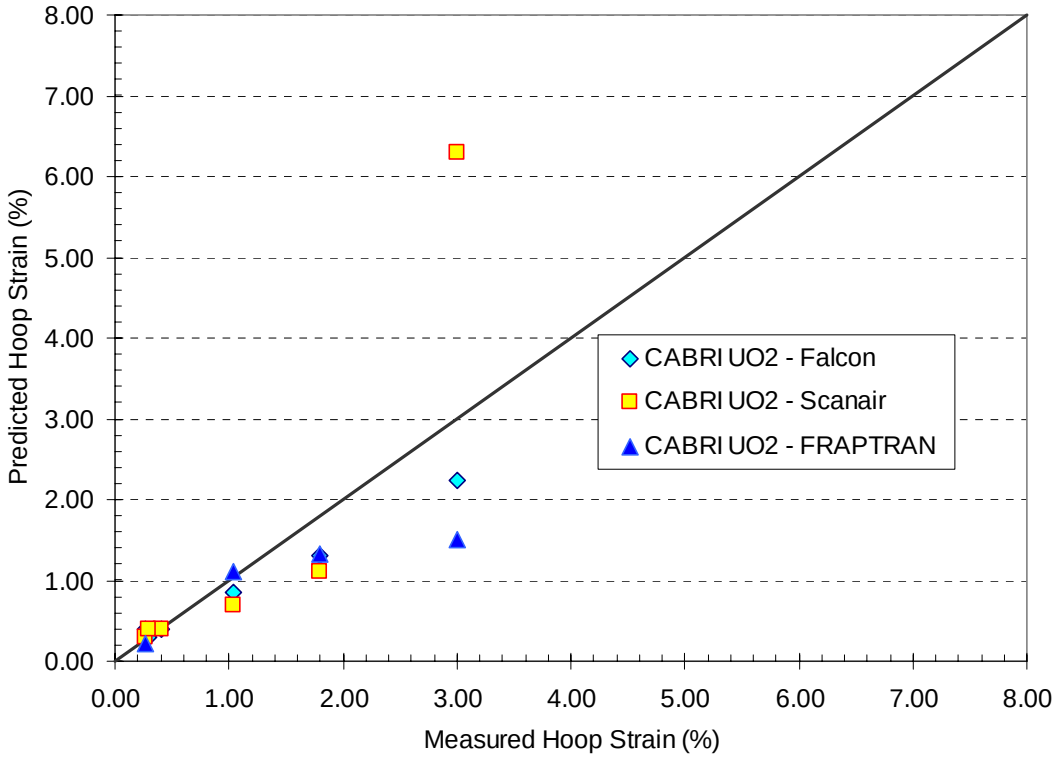

Figure F-8.3. Predicted versus Measured Cladding Residual Hoop Strain for FALCON, SCANAIR, and FRAPTRAN

Technical Concerns/Requests for Additional Information on the EPRI RIA Topical Report
Based on the NRR Safety Evaluation Report – March 2005

ID Number	Description of Technical Concern
	Coolability Limit
C-1	In addition, the FALCON code version used in the development of the coolability limit underestimates fuel temperatures at high burnups resulting in an overprediction of the energy needed to cause fuel melting when the fuel burnup is above 40 gigawatt days per metric ton uranium (GWD/MTU). This effect leads to a non-conservative melt enthalpy limit.
C-2	The Topical Report discusses the impact of gadolinia on the proposed fuel coolability limit but does not address the impact other poisons such as erbia.
C-3	Although we believe there may be a justifiable coolability limit at an enthalpy above the Research Information Letter (RIL)-0401 cladding failure threshold, we cannot accept the proposed limit because of the lack of experimental data. Assertions are made about limited amounts of fuel dispersal, small magnitude of pressure pulses, and inefficient energy conversion of non-molten particles. However, these assertions are based mostly on tests in the Nuclear Safety Research Reactor (NSRR) with medium-to-high-burnup specimens under conditions that are far from typical for a nuclear power plant. No analysis is presented that would allow one to interpret these data or to compare predicted light-water reactor pressure pulses with vessel limits. We do not believe it is adequate to assume that molten fuel is needed to produce an energetic fuel-coolant interaction and then use a burnup-dependent melt enthalpy as the limit.

ID Number	Description of Technical Concern
	Failure Threshold
F-1	A best estimate fit to the mechanical failure data is used to determine the critical strain energy density (CSED). This fit means that slightly less than 50 percent of the rods will fail just below the failure threshold when failure is not predicted. This is not consistent with NRC criteria that dose consequences for accidents not be underestimated. A lower bound fit of the failure data would be more appropriate to determine the RIA failure and subsequent radionuclide release and dose estimates.
F-2	Clad cracking in CABRI REP Na-8 and REP Na-10 was not associated with hydride blisters or spalled locations in these tests. We believe that spalling did not cause the early failure in these tests but failure was simply a consequence of heavy oxidation that produced hydrides which degraded ductility. Eliminating these two tests results in an artificially high CSED curve.
F-3	The single mixed-oxide (MOX) fuel failure in the French Test Reactor (CABRI) series was assumed to be different from the uranium dioxide (UO_2) failures because of inhomogeneities and a gas expansion model was invoked for only this test. We are not convinced that gas expansion can significantly enhance the cladding stress as postulated. Thermal expansion of MOX and UO_2 are almost identical, so the loading from expansion should not depend on homogeneity.
F-4	We agree that the method of determining oxidation of the two Special Power Excursion Reactor Test tests was not accurate. We do not agree that adjusting that result for densities (Pilling-Bedworth ratio) corrects the problem. Our previous analysis for the irradiation conditions of these specimens indicates that the oxide thickness should be less than 65 microns, rather than larger as was concluded in the report. Moving these points out to 130 microns produces a non-conservative acceptance limit.

ID Number	Description of Technical Concern
F-5	It is known that stress state has a significant impact on strain-to-failure and will also impact CSED. The mechanical test data presented are based on three stress states: hoop tensile (uniaxial ring tests), axial tensile and biaxial (burst tests). The EPRI CSED model development includes the ring (tensile) strain-to-failure data and appears to fit this data better than the burst or axial tension data. Based on round robin tests performed by Argonne National Laboratory, Commissariat a l'Energie Atomique, and the Russians it is known that the ring tensile tests are not a measure of material property in terms of strain-to-failure but instead ring test failure strains are a function of specimen size and test apparatus. The burst which are the most relevant to RIA and the axial tensile data appear to have lower strain energy densities (SEDs) at failure on average than the ring test data. This suggests that the proposed CSED correlation may seriously under predict the probability of failure leading to a non-conservative correlation.
F-6	It appears that only PWR data are used to develop the CSED correlation as a function of oxide/cladding thickness ratio. However, the hydrogen pickup fraction is considerably higher for BWR cladding than for PWRs. Section 3.3.2 of the TR suggests that mechanical tests provided by Wisner and Adamson (1998) demonstrate that BWR Zircaloy-2 cladding will have equal or greater ductility than PWR Zircaloy-4 cladding. Examination of this reference appears to support this assertion up to a burnup of 45 GWD/MTU but does not support it above this burnup level. In addition, recent RIA tests performed on BWR rods in NSRR suggest that the BWR rod ductility drops significantly at burnups above 57 GWD/MTU and hydrogen levels above 150-200 parts-per-million. Therefore, the proposed limit provides non-conservative results.

ID Number	Description of Technical Concern
F-7	The argument is made that the SED/CSED model is derived directly from the J-integral methodology used for fracture mechanics analysis. This argument may be challenged by many fracture mechanics experts; however, there is no argument with regard to the application of J-integral fracture toughness with respect to the American Society for Testing and Materials (ASTM standards for determining fracture toughness. A specific test method is specified for determining the J-integral values as stated in ASTM 813 and ASTM 1820 and this ASTM test method is not the same as the test measurement methods used to develop the SED/CSED methodology. Furthermore, ASTM 1820 states that J-integral test should not be applied to brittle materials. Zircaloy uniform elongation strains of less than 1.0 to 1.5 percent strain (applicable to high burnup cladding) with a high hydrogen content appear to display significant brittle behavior. This suggests that the use of SED/CSED may not be applicable to high burnup cladding. This lack of applicability for the J-integral tests is further demonstrated by examining the available open literature J-integral data from irradiated Zircaloy with high hydrogen content. A plot of the J-integral data from Zircaloy versus hydrogen content does not show a discernable dependence, while a plot of the plane strain fracture toughness (K_{IC}) demonstrates a definitive dependence with a significant decrease in K_{IC} with increasing hydrogen content, which is expected due to hydrogen embrittlement. This suggest that the J-integral method may not be applicable in determining hydrogen embrittlement in high burnup Zircaloy.
F-8	The staff attempted to duplicate the SEDs calculated with FALCON by programming Equation 2-14 into the FRAPTRAN code and applying the same methodology. The studies performed with FRAPTRAN were unable to duplicate the SED values for those CABRI and NSRR test rods with plastic strains at or above 1 percent. This indicates that the SED values may be code dependent.